AN ABSTRACT OF THE THESIS OF

Sung-Kwan Park for the degree of Doctor of Philosophy in Mechanical Engineering presented on March 12, 1993.

Title: Numerical Analysis of Liquid Cooling by Natural Convection for Heated Protrusions Simulating Vertical Plate-Mounted Electronic Components Facing an Opposing Plate

Redacted for Privacy

Abstract approved: Dwight J. Bushnell

Natural convection liquid cooling from three uniformly heated protruding elements, simulating evenly spaced, vertical, plate-mounted electronic components facing an opposing unheated plate within an enclosure maintained at constant temperature, was numerically investigated. Two-dimensional coupled conduction and natural convection governing equations were solved, based upon finite control volumes for a wide range of Rayleigh numbers. Dielectric liquids, including distilled water, FC-75, and ethylene glycol, were employed as coolants for a Prandtl number range from 5.9 to 103. Modified channel Rayleigh numbers and channel Rayleigh numbers from 10^4 to 10^{10}, based on five channel spacing to vertical plate height ratios (b/h), respectively, 0.2, 0.267, 0.333, 0.4, and 0.5, were analyzed.

Protruding surface temperatures of the uniformly heated elements were lowest for water, followed by ethylene glycol, and were highest for FC-75. Three distinct flow patterns were observed for the protruding heated channels: reversed flows due to the effect of circulation at the top portion of the enclosure, relatively high velocity flows at the front of the heated elements, and relatively weak flows adjacent to the unheated shrouding plate.

Optimum channel spacing to height ratios were analyzed to determine effective temperature reductions for the protruding heated surfaces. For water, FC-75, and ethylene glycol, subject to varied heat input levels, optimal ratios were, respectively, 0.333, 0.4, and greater than 0.4. The most favorable correlations of protruding vertical channels for all cooling liquids combined were

$$\mathrm{Nu}_b = 1.6539 \left[\left(\frac{b}{h} \right) \mathrm{Ra}_b^* \right]^{0.1371}$$

and

$$\mathrm{Nu}_b = 1.4902 \left[\left(\frac{b}{h} \right) \mathrm{Ra}_b \right]^{0.1400}$$

with standard deviations of 9.75% and 9.76%, respectively, for $5.9 \leq \mathrm{Pr} \leq 103$, $0.2 \leq b/h \leq 0.5$, and $1.03 \leq R_1 \leq 9.8$, where R_1 is the solid heating element to liquid thermal conductivity ratio.

Numerical Analysis of Liquid Cooling by Natural Convection for Heated Protrusions Simulating Vertical Plate-Mounted Electronic Components Facing an Opposing Plate

by

Sung-Kwan Park

A THESIS

submitted to

Oregon State University

in partial fulfillment of
the requirements for the
degree of

Doctor of Philosophy

Completed March 12, 1993

Commencement June 1993

APPROVED:

Redacted for Privacy

Associate Professor of Mechanical Engineering in charge of major

Redacted for Privacy

Head of Department of Mechanical Engineering

Redacted for Privacy

Dean of Graduate School

Date thesis is presented March 12, 1993

Typed by B. McMechan for Sung-Kwan Park

ACKNOWLEDGEMENTS

I would like to express my sincere appreciation to my major advisor, Dr. Dwight J. Bushness, for his consistent support and guidance during my period of enrollment at Oregon State University. Without his interest and suggestions, this research could not have been completed.

I would also like to thank each of the members of my committee, including Professors Lorin R. Davis, Milton B. Larson, Joel Davis, and Sheikh Burhanuddin, for their kind advice and encouragement. The valuable help given by Drs. Junku Yuh and Heidi Pattee was greatly appreciated for reason of the time they gave to me.

I would also like to extend my appreciation to the Department of Mechanical Engineering for providing me with a teaching assistantship during my graduate program. Thanks are also due to Bill McMechan for his help with the thesis format.

This thesis is dedicated to my parents with deep gratitude for their endless love and encouragement. Without their prayers and devotion, I could not have completed my program. Finally, I would like to express my appreciation to my wife, Shin-Ahe, and my three sons, Joshua, Paul, and Isaiah, for their patience and love. They have been and they will be my entire life.

TABLE OF CONTENTS

TABLE OF CONTENTS (continued)

LIST OF FIGURES

LIST OF FIGURES (continued)

LIST OF FIGURES (continued)

LIST OF FIGURES (continued)

LIST OF FIGURES (continued)

LIST OF APPENDIX FIGURES

LIST OF TABLES

NOMENCLATURE

Symbol	Description
A	Each discrete heating area, $l_c B$, m^2
B	Protruding discrete heating element height, cm
b	Channel spacing, cm
$\left(\frac{b}{h}\right)Gr_b$	Channel Grashoff number [11], $(b/h)(g\beta\Delta T b^3/(\nu^2_f))$
$\left(\frac{b}{h}\right)Ra_b$	Channel Rayleigh number, $(b/h)(g\beta Q b^3/(k_f \alpha_f \nu_f))$
$\left(\frac{b}{h}\right)Ra^*_b$	Modified channel Rayleigh number, $(b/h)(g\beta q'' b^4/(k_f \alpha_f \nu_f))$
Cp	Specific heat at constant pressure, J/(kg°K)
d	Horizontal distance from protruding surface to unheated plate, cm
Gr_b	Grashoff number, $g\beta\Delta T b^3/(\nu^2_f)$
g	Gravitational acceleration, m/sec^2
H	Height of enclosure, cm
h	Channel height, cm
h_a	Vertical distance between plate and enclosure, cm
h_b	Vertical distance from heating element to plate edge, cm
h_c	Vertical distance between protruding heated elements, cm
k_f	Thermal conductivity for coolants, W/m°K
k_{s1}	Thermal conductivity for protruding solid heated element, W/m°K
k_{s2}	Thermal conductivity for solid unheated plates, W/m°K

NOMENCLATURE (continued)

Symbol	Description
L	Horizontal length of enclosure, cm
l_a	Horizontal distance between enclosure and plate, cm
l_b	Thickness of plate, cm
l_c	Protrusion length, cm
$Nu_{b,each}$	Average Nusselt number of each protruding surface
Nu_b	Average Nusselt number of all three protruding surfaces
P^*	Pressure, N/m^2
P	Dimensionless pressure, $P^*/\rho_f U_o^2$
Pr	Prandtl number, υ_f/α_f
Q	Heat input per unit axial length of computational heated element, W/m
q''	Heat flux, W/m^2
$\overline{q}''$	Average heat flux of protruding heated surface, W/m^2
R_1	Protrusion to liquid thermal conductivity ratio, k_{s1}/k_f
R_2	Unheated plate to liquid thermal conductivity ratio, k_{s2}/k_f
R^*_1	Material property ratio, $(\rho_f Cp_f)/(\rho_{s1} Cp_{s1})$
R^*_2	Material property ratio, $(\rho_f Cp_f)/(\rho_{s2} Cp_{s2})$
Ra_b	Rayleigh number, $g\beta Qb^3/k_f\alpha_f\nu_f$
Ra^*_b	Modified Rayleigh number, $g\beta\overline{q}''b^4/k_f\alpha_f\nu_f$
Ra_t	Rayleigh number for isothermally heated case, $g\beta\Delta Tb^3/(\alpha_f\nu_f)$

NOMENCLATURE (continued)

Symbol	Description
s	Vertical distance from first protruding element to third protroding element, cm
T^*	Temperature, °K
T_c	Cooling enclosure wall temperature, °K
T	Dimensionless temperature, $(T^* - T_c)/(Q/k_f)$
t	Time, sec
U	Dimensionaless horizontal velocity, u/U_o
U_0	Reference velocity, $(\alpha_f/b)(Ra_bPr)^{1/2}$ $(=(g\beta Qb/k_f)^{1/2})$, m/sec
u	Horizontal velocity component, m/sec
V	Dimensionless vertical velocity component, v/U_o
v	Vertical velocity component, m/sec
X	Dimensionless horizontal coordinate, x/b
x	Horizontal coordinate, cm
x'	Horizontal coordinate at edge of first protruding element surface, cm
Y	Dimensionless vertical coordinate, y/b
y	Vertical coordinate, cm
y'	Vertical coordinate at edge of first protruding element surface, cm

NOMENCLATURE (continued)

Greek Symbols	Description
α	Thermal diffusivity, $k/\rho C_p$, m^2/sec
β	Thermal expansion coefficient, $1/°K$
μ	Dynamic viscosity, Kg/m-sec
ν	Kinematic viscosity, m^2/sec
ρ	Density, Kg/m^3
τ	Dimensionless time, $(U_0/b)t$
Θ	Ratio of temperature difference, $\Delta T_i/\Delta T_{min}$
Ψ	Dimensionless streamfunction, (Eqn. 4-52)

Subscripts

f	Fluid
s1	Solid 1 (electronic package)
s2	Solid 2 (printed circuit board)

Numerical Analysis of Liquid Cooling by Natural Convection for Heated Protrusions Simulating Vertical Plate-Mounted Electronic Components Facing an Opposing Plate

CHAPTER 1

INTRODUCTION

Throughout its existence, the electronics industry has strived to improve the reliability of electronics systems by the reduction of system operating temperatures and the junction temperature among system components. Recently, electronics systems have been rapidly shrinking in size, while at the same time the complexity and the capability of these systems continues to grow. Thus, system volumes have decreased as system power has increased, resulting in dramatic increases in system heat density.

It was recently determined that the peak heat fluxes in a newly manufactured computer circuit were several times greater than for a comparable circuit in an older computer [1,2]. For the 25-year period indicated in Figure 1.1, the rates of increase for module level heat fluxes were the most dramatic in the final five years of the period in question. At the same time, allowable operating temperatures have been maintained at relatively constant levels, a

factor which makes the cooling problem an even greater challenge within the electronics industry.

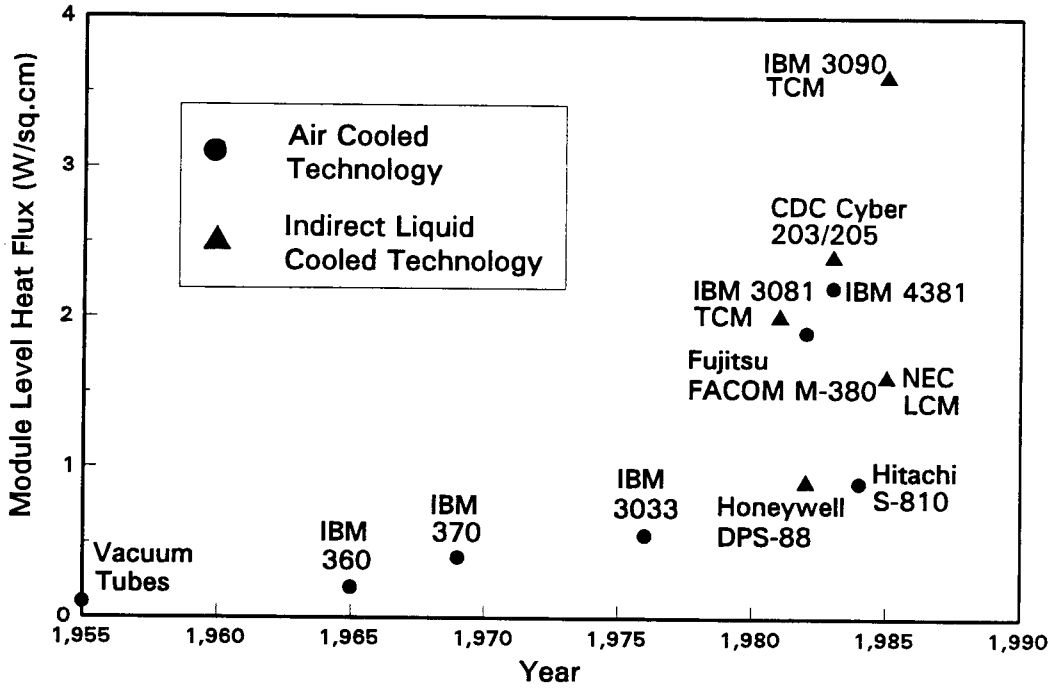

Fig. 1.1 Trend in heat fluxes at the module level [1,2].

Unless they are matched by improvements in cooling capacity, the power densities that exist within modern large-scale computers could result in operating temperatures that will be sufficiently high to degrade electrical performance and system reliability. In some cases, severe physical damage to the powered components may result. The issue resides within the need to control temperatures for each system component to ensure the manufacture of reliable electronic systems. Therefore, the basic heat transfer problem evidenced in electronic systems is the removal of internally generated heat by the provision of adequate heat

flow paths from the sources of heat to an ultimate sink, which is often the surrounding fluid.

Due to the extent and variety of industrial applications which may be affected, numerical heat transfer in vertical channels with discrete protruding heat sources, simulating electronic integrated circuit (IC) elements surface-mounted on parallel vertical printed circuit boards (PCB), has received an increasing amount of attention. Electronics industry engineers have sought means to add to the cooling capacity of electronic packages. However, efficient cooling cannot be achieved in the absence of the ability to understand the heat transfer processes, including the flow and thermal fields applicable to each specific model of manufacture.

Figure 1.2 illustrates an array of heated blocks attached to an unheated vertical plate with an opposed, unheated shrouding plate, used for the investigation of natural convection in a vertical channel. In the illustration, the uniform heat sources of the protruding arrays are all equal and the arrays, viewed as rectangular cross section areas, are evenly spaced and mounted horizontally on the vertical plate. Dielectic fluids at different Prandtl numbers are employed as the working fluids. This computational model is of practical importance insofar as it simulates the case of heated ICs or electronic modules mounted on PCBs. The opposing unheated shrouding plates shown in Figure 1.2 may be considered as an unheated PCB on which a

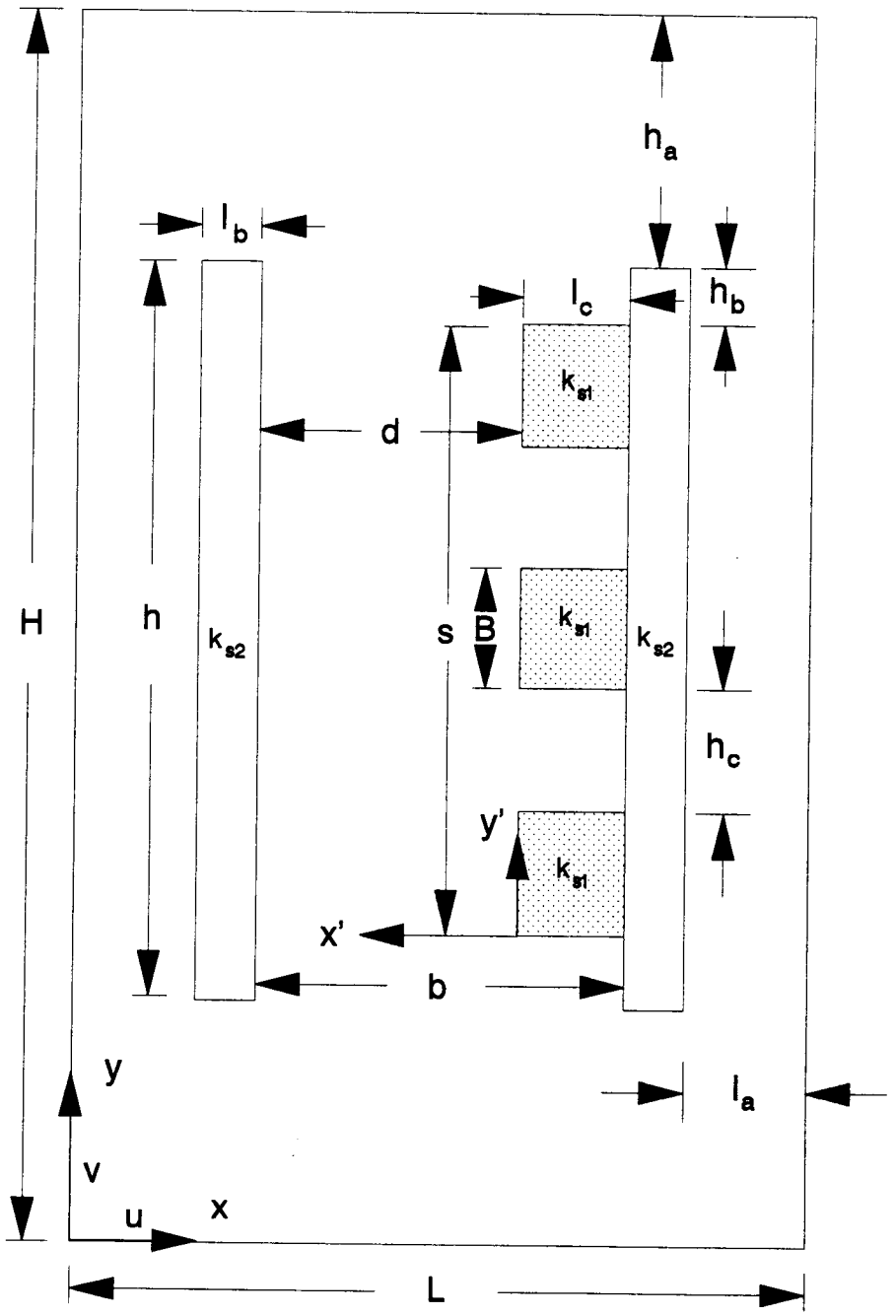

Fig. 1.2 Schematic diagram of fluid-cooled protruding heating channel.

number of small elements, insignificant as heat generators, have been placed.

When the blocks are heated, a buoyancy-driven flow occurs as each heated block induces an upward buoyancy boundary layer flow. In turn, each protruding block is characterized by a rising flow, which then may have an effect upon neighboring rising flows at points downstream. The overall rising flow accelerates as it proceeds downstream. Thus, the overall boundary layer builds up and thickens near the upper blocks. This type of buoyancy flow may be changed by unheated shrouding plates placed in relation to protruding heated plates at certain channel spacings. However, the interaction of thermal energy spread and momentum diffusion within the vertical channels makes it difficult to provide accurate analyses of the prediction of the natural convection processes. From numerical computations, it may be possible to determine whether the described interactions enhance or reduce natural convection heat transfer rates.

The problem under consideration in Figure 1.2 has been examined numerically, based upon the finite control volume methods described by Patankar [3], a procedure which in turn is based upon the application of the SMAC algorithm [4]. This investigation is based upon the recognized principle that buoyancy flows may be modified when an unheated wall is placed parallel to and opposite to a protruding element plate distinguished by selected finite spacing

between the plates. With reference to the problem considered in Figure 1.2, the objectives of the present numerical analyses of heat transfer were as follows:

1) Determine the natural convection heat transfer characteristics of a vertical channel with protruding discrete heat sources;
2) Identify the heat transfer effects of unheated walls;
3) Describe the geometric parameter effects of the heat transfer process;
4) Obtain steady-state streamline flow patterns and thermal distributions in isothermal lines;
5) Propose the most favorable numerical correlation in the form

$$Nu_b = f\left(\frac{b}{h} Ra_b^*\right) \text{ and } Nu_b = f\left(\frac{b}{h} Ra_b\right);$$

6) Compare the numerical output with experimental results obtained from consideration of a similar model; and
7) Determine the outline of the optimal geometric parameters for strong heat transfer effects in cooling the heated modules with various fluids.

The natural convection flow and heat transfer rate may be altered, dependent upon the specific boundary conditions, the geometric configuration, and cooling properties. The advantage of natural convection cooling is that no fans or blowers are required to move fluids. Rather, fluid

movements are induced by the density differences which result from the heat generated by electronic components. A number of dielectric coolants have been considered as candidates for working fluids for present generations of natural convection models. These candidates include air, distilled water, fluorochemicals (FC-75, FC-77, or FC-78), and ethylene glycol. However, since it is the usual fluid source for forced convection, air cooling by natural convection has proved to be inadequate. Air cooled by natural convection remained too hot even when relatively small heat inputs were supplied. This indicated that air cooling by natural convection would be unable to support the packaging densities and heat flux levels required in recent generations of mechanical systems (Fig. 1.1). Therefore, for the present study of heat transfer capabilities and the temperature limits of operations, distilled water, FC-75, and ethylene glycol were the dielectric cooling liquids considered.

Numerical computations were performed for a range of governing parameters frequently encountered in actual applications. The input levels were as given in Table 1.1. Based upon channel spacings, the Rayleigh number ranged from 2×10^5 to 2×10^{10}. Prandtl numbers were varied from 5.9 to 103. The ratios of channel spacing to PCB height ratios (b/h) considered were 0.2, 0.267, 0.333, 0.4, and 0.5, whereas the heated element width to channel spacing ratios (l_c/b) were 0.267, 0.333, 0.4, 0.5, and 0.667

and the heated element height to channel spacing ratios (B/b) were 0.333, 0.417, 0.5, 0.625, and 0.833.

Table 1.1 Parameter values used for numerical computations

Dimensionless parameters	Minimum	Maximum
Unfixed		
Pr	5.9	103.0
Ra_b	2.0 E+5	2.0 E+10
k_{s1}/k_f (= R_1)	1.03	9.8
k_{s2}/k_f (= R_2)	0.43	4.05
b/h	0.2	0.5
l_c/b	0.267	0.667
B/l_a	1.0	0.526
B/b	0.333	0.833
Fixed		
H/B	10	
L/B	6	
h_a/B	2	
h_b/B	0.5	
h_c/B	1	
h/B	6	
l_b/B	0.5	
l_c/B	0.8	

CHAPTER 2

LITERATURE REVIEW

2.1 Scope

Renewed interest in laminar free convection in vertical channels stems from the increasing number of applications which require a cooling process for electronic circuit boards. The microminiaturization of electronic devices has achieved considerable progress with the remarkable pace of development in electronics engineering. Typically, vertical printed circuit boards containing any number of electronic devices are aligned to form vertical channels. Each circuit generates heat and is thus sensitive to temperature. In modern electronics, the heat is generated from high power dissipating components such as transistors and resistors mounted on PCBs, rather than from the entire PCB itself. Consequently, additional information on the heat transfer process for heated vertical parallel plates has become increasingly desirable.

When two parallel plates are placed face-to-face in vertical positions within a fluid, and where at least one of the plates is heated, a flow is induced between the plates due to buoyancy effects. Based upon this principle, current research directions for natural convection of

vertically heated surfaces have been changing from interest in simple flush-heated vertical channels to more practical considerations: (1) The effects of localized discrete heat sources along the vertical surface (a case which ignores the thickness of the chips or modules); and (2) the effects of a discrete and protruding heated block (a case which considers the thickness of a block array simulating electronic components).

As a result, to the extent that previously completed research is related to the area of interest of the present investigation, this chapter reviews only a selection of relevant and important methods and findings. Research material on heat transfer for electronic and microelectronic equipment reviewed for vertical plates and vertical channels is categorized in three sections: natural convection from flush-mounted heat sources; natural convection from localized discrete heat sources; and natural convection from protruding discrete heat sources.

2.2 Natural Convection From Flush Heat for Vertical Plates and Vertical Channels

Problems of heat transfer by means of natural convection along vertical plates or in vertical channels have been the subject of investigation for a number of years. Sparrow and Gregg [5] obtained an exact solution for the laminar boundary layer equations for the similarity vari-

able from a vertical plate with uniform heat flux. Heat transfer parameters were calculated for Prandtl numbers in the range 0.1 to 100. It was demonstrated that when average Nusselt numbers were calculated for a plate with uniform surface heat flux, based upon temperature differences at one-half the height, the results were very close to those for a uniform temperature plate.

Fujii and Fujii [6] proposed a simple and accurate correlation for the prediction of local Nusselt-Prandtl relationships for a vertical plate with uniform heat flux. These relationships were defined as

$$Nu_x = C^*(Ra_x^*)^{1/5} \tag{2-1}$$

and

$$C^* = \left(\frac{Pr}{4 + 9Pr^{1/2} + 10Pr}\right)^{1/5}, \tag{2-2}$$

where C^* covered any range of Prandtl number. This correlation was directed explicitly for Nusselt numbers as a simple function of Prandtl numbers. Roy [7], who solved the free convection boundary layer equations for large Prandtl number fluids, recommended another relationship for C^*, as given in equation (2-1), and then compared his results with those obtained by Fujii and Fujii [6] as follows:

$$C^* = \frac{1}{1.5823 + 0.3129Pr^{-1/2} - 0.0419Pr^{-1}} \cdot \qquad (2\text{-}3)$$

Churchill and Chu [8] developed correlation equations for laminar and turbulent free convection for an isothermal vertical plate. The correlation for the laminar regime was

$$Nu = 0.68 + \frac{0.670Ra_t^{1/4}}{\left[1 + \left(\frac{0.492}{Pr}\right)^{9/16}\right]^{4/9}} \cdot \qquad (2\text{-}4)$$

Equation (2-4) provided a good representation for all $Ra_t < 10^9$. The correlation for the laminar plus turbulent regime was

$$Nu^{1/2} = 0.825 + \frac{0.387Ra_t^{1/6}}{\left[1 + \left(\frac{0.492}{Pr}\right)^{9/16}\right]^{8/27}} \cdot \qquad (2\text{-}5)$$

Laminar free convection in heated vertical channels has been of considerable interest for electronic cooling applications and, therefore, has been subject to extensive investigation in the field of heat transfer. Elenbaas [9], who pioneered studies concerned with the effects of natural convection between vertical channels, considered the phenomenon of heat dissipation from parallel vertical plates in air environments and discussed the effects of heat transfer with respect to the ratio of plate height to channel spacing. It was demonstrated that heat dissipation increased significantly as the channel spacing was decreased, attributed to the increase of flow velocity in proportion to the decrease in channel spacing. The correlation for

symmetrically uniform surface temperature boundary conditions was

$$Nu_b = \frac{1}{24}\left(\frac{b}{h}\right)Ra_t\left[1 - \exp\left(-\frac{35}{Ra_t}\frac{b}{h}\right)\right]^{3/4}, \qquad (2\text{-}6)$$

where b is channel spacing and h is the plate height.

Tao [10] examined heat transfer problems for a fully developed laminar flow of combined free and forced convection in a vertical channel with constant axial wall temperature gradient, both with and without heat generation, introducing a complex function which was directly related to the velocity and temperature fields. Bodoia and Osterle [11] developed a numerical solution for free convection between symmetrically heated vertical plates, using the finite difference method from the basic governing equations for continuity, momentum, and energy. Based upon the assumption that the fluid entered the channel at an ambient temperature and a flat velocity profile, variations in velocity, temperature, and pressure were obtained throughout the flow field. The flow and heat transfer characteristics of the channel were determined and height, defined as the distance from the channel entrance to that position along the channel where the flow approaches its fully developed values, was estabished. With the exception of low values of channel Gr, the numerical results obtained from their study appeared to be in good agreement with the experimental work of Elenbaas [9].

Aung [12] presented fully developed flow solutions for laminar free convecton for a vertical, parallel-plate channel with asymmetric heating. The channel walls were maintained either at uniform fluxes of heat or at uniform wall temperatures. To account for the asymmetric heating of the walls, variances from 0 to 1 in wall heat flux ratios, or in wall temperature ratios, were tested.

Miyatake et al. [13] and Miyatake and Fujii [14] sought numerical solutions for heat transfer by natural convection between two vertical parallel plates submerged in an infinite fluid, where one of plates was uniformly heated and the other was thermally insulated. It was assumed that the channel inlet and outlet pressures were equal to the static pressure of the ambient fluid, and that the fluid entered the channel with a uniform velocity profile. Numerical results were obtained for local Nusselt values for fluids with Prandtl numbers 0.7 and 10. The heat transfer correlations for the isothermally heated case were

$$Nu_b = 0.613\left(\frac{b}{h}Ra_t\right)^{0.25}, \qquad \text{for } Pr = 0.7 \qquad (2\text{-}7)$$

and

$$Nu_b = 0.68\left(\frac{b}{h}Ra_t\right)^{0.25}, \qquad \text{for } Pr = 10\ . \qquad (2\text{-}8)$$

Miyatake and Fujii [15,16] subsequently performed a numerical analysis to determine flow development and heat transfer characteristics for laminar natural convection between

two parallel plates with asymmetric uniform wall temperatures and with asymmetric uniform heat fluxes.

Siegel and Norris [17] experimentally tested free convection between uniformly heated parallel vertical plates which were partially enclosed. In these experiments, the top of the rectangular space between the plates was left open, whereas the bottom and the sides were closed. Results indicated that the heat input per unit area was substantially uniform, but that the rise in surface temperature increased and the local Nussult number decreased as either of the cross-sectional dimensions of the free convection space was reduced.

Sparrow et al. [18] provided both experimental results and numerical solutions for natural convection in an open-ended vertical channel where one channel wall was maintained at a uniform temperature, while the second principal wall was unheated. The experiments were conducted with water in the channel. The numerical results covered a Prandtl number range from 0.7 to 10. The heat transfer correlations for the interwall area were

$$\mathrm{Nu}_b = 0.688\left[\left(\frac{b}{h}\right)\mathrm{Ra}_t\right]^{0.249}, \qquad \text{for } 0.7 < \mathrm{Pr} < 10, \quad (2\text{-}9)$$

where $2 \times 10^2 < (b/h)\,\mathrm{Ra}_t < 10^5$.

Levy [19] discussed the problem of determining optimum spacing between parallel vertical isothermal flat plates for natural convection heat transfer to the environment. Results were compared with the optimum spacing for an air

environment, first suggested in the experimental data derived by Elenbaas [9] and subsequently derived numerically by Bodoia and Osterle [11]. Levy [19] obtained a criterion which could be used to determine the minimum vertical isothermal channel spacing required to minimize differences in temperature between the plates and the fluid.

Burch et al. [20] investigated numerical solutions for laminar natural convection between finitely conducting vertical plates. Analysis of the physical situation of the solution involved consideration of both the energy conservation equation for solid walls and the equations of mass, momentum, and energy conservation for the fluid. Results were obtained for Grashof numbers 10, 10^3 and 10^6, wall-to-fluid conductivity ratios of 1 and 10, and wall thickness-to-width ratios of 0.1 and 0.5. It was indicated that conduction exercised a significant influence upon natural convection heat transfer, particularly at low ratios of conductivity and high ratios of wall thickness to channel width.

Kim et al. [21] sought numerical solutions for laminar free convective heat transfer in channels formed between a series of vertical, parallel plates with an embedded line heat source of uniform temperature. The numerical model derived resembled those for cooling passages in electronic equipment. The investigation was based upon the assumption that the nature of the circuit board arrangement was such that heat dissipation from this type of heat source would

be partially due to fluid convection and partially due to conduction to the substrate. In addition, this study employed a repeated boundary condition based upon the concept that the temperature and heat flux at any point on the vertical surface would be identical to those at any corresponding point on the vertical surface in the adjacent channel.

Hanzawa et al. [22] experimentally investigated natural convective heat transfer between vertical parallel plates with symmetric and asymmetric heating at high Gr numbers ranging from 10^5 to 10^8. Since most of the previous experimental and numerical approaches had been restricted to small temperature differences between heated plates and the fluids for the case of low buoyancy forces, the object of this investigation was to obtain information on heat transfers within electronic devices .

Chang and Lin [23] subjected transient natural convection due to step changes in plate temperatures within symmetrically heated vertical plate channels of finite height to numerical solution. Results were obtained for air where Ra_t was varied from 10^3 to 10^6 and the aspect ratio (b/h) varied from 5 to 10. The correlation equation for the average Nusselt number was proposed as:

$$Nu_b = 14.1 - 9.42 \log\left[\left(\frac{b}{h}\right)Ra_t\right] + 2.13\left[\log\left[\left(\frac{b}{h}\right)Ra_t\right]\right]^2, \qquad (2\text{-}10)$$

Wirtz and Stutzman [24] reported on experimental heat transfer measurements for two-dimentional natural convection between vertical plates subjected to uniform and symmetric heat fluxes. Data were collected over a range of heat fluxes and geometric parameters where the flow was in the developing temperature field regime. Correlations were based upon the calculation of maximum plate temperature variations for given heat flux and plate geometry inputs.

Ramanathan and Kumar [25] presented numerical results for natural convection flows between two vertical, parallel and uniform heat flux plates within a large enclosure. The numerical data developed were compared with the experimental data derived by Wirtz and Stutzman [24]. Asymptotic correlations were presented for $1 \leq h/b \leq 15$ and $10 \leq Ra^* \leq 3 \times 10^5$ as follows:

$$Nu_b = \left[185\left(\frac{b}{h}\right)^5 + \left[23\left(\frac{b}{h}Ra^*\right)^{-1.3} + 0.5\left(\frac{b}{h}Ra^*\right)^{-0.6}\right]^{-1.25}\right]^{0.2} . \qquad (2\text{-}11)$$

2.3 Natural Convection Heat Transfer From Localized Discrete Heat for Vertical Plates and Vertical Channels

Despite the fact that the natural convection induced by discrete heating has an obviously practical value for electronic equipment cooling applications, this phenomena has received little attention to date. In this section,

consideration is given to the natural convection heat transfer characteristics resulting from a discrete heating source as compared to those resulting from a uniform heating source.

Jaluria [26] conducted a numerical study of the interacting natural convection flows generated by isolated thermal energy sources, such as those for electronic components, located on vertical adiabatic surfaces. Of particular interest was the nature of the flow at low Grashof values (i.e., from 10 to 10^5) based upon the height of the heated element and the surface heat flux. In turn, Chu et al. [27] examined the numerical effects of localized heating in rectangular channels, based upon an unsteady state formulation and an alternating direction-implicit method. The heating element was a lengthy isothermal strip located in an otherwise insulated vertical wall. Computations were conducted for $Pr = 0.7$, $0 < Ra_t < 10^5$, and aspect ratios from 0.4 to 5. The size and locations of the heater strip were also varied. The accuracy of solutions was qualitatively evaluated by experimental examination of smoke flow patterns within a 2.54 cm by 2.54 cm enclosure. However, the range of Rayleigh numbers was not sufficient to allow the solution of the large Rayleigh numbers required for many practical applications.

Turner and Flack [28] experimentally measured heat transfer rates for laminar convection air flows in rectangular enclosures with a single isothermally heated vertical

wall, a concentrated cooling strip placed on the opposing wall, and adiabatic top and bottom plates. The geometry for these experiments was the inverse of the geometry examined by Chu et al. [27]. The aspect ratio of the enclosure and the size and location of the cooling strips were parametrically varied for Grashof numbers from 5×10^6 to 9×10^6.

Yan and Lin [29] sought numerical solutions for the effects of discrete heating on vertical, parallel channel flows driven by the buoyancy force of thermal diffusion. Results were obtained for Pr = 0.7, and Rayleigh numbers to 10^3. Attention was focused upon comparisons of the effects of discrete heating boundary conditions and uniform heating boundary conditions.

Keyhani et al. [30] conducted both experimental and numerical investigations of free convection in a vertical cavity (for aspect ratios of (h/b) = 4.5) for a single isothermal vertical cold wall and, alternatively, three adiabiatic and flush-heated sections of equal height on an opposite vertical wall. Experiments were conducted with ethylene glycol for nominal power inputs to 1.03 W/cm^2. Streamlines and isothermal patterns from the numerical results were demonstrated for Pr = 25 and Pr = 166.

2.4 Natural Convection from Protruding Discrete Heat Sources for Vertical Plates and Vertical Channels

Microelectronic chips normally protrude from the PCB substrate. To improve conformance to this real situation, a number of analytical and experimental investigations have been conducted to determine the effects of single, protruding simulated chips, or arrays of protruding chips, mounted on a PCB.

Hwang [31] presented an analytical and experimental study of heat transfer from mixed free and forced convection for a vertical flat plate with square protuberances, based upon the simulation of the heat dissipating electronic components. This study was based upon the assumption that the free and forced flow directions were either identical for the upward flows or exact opposites for the downward flows. The experiments indicated that the free convection increased heat transfer for the upward flows, while the downwards flow for a laminar mixed-flow regime were decreased.

Braaten and Patankar [32] considered the effects of buoyancy on fully developed flows and heat transfer for shrouded arrays of rectangular blocks modifying components mounted on closely spaced circuit boards. An analysis was conducted for laminar flows, assuming both fully developed hydrodynamic and thermal conditions. Solutions were ob-

tained for a range of Rayleigh numbers from 0 to 10^6 for five different physical situations.

Ortega and Moffat [33] presented the results of an extensive experimental investigation of the natural convective heat transfer rates and thermal characteristics of a regular array of protruding, cubical roughness elements mounted on an insulated plane wall opposed by a smooth insulated plate. Shrouded array heat transfer results were compared to those obtained with the Sparrow and Gregg correlations [5]. When a shrouding plate was placed in front of the array, heat transfer behavior was changed significantly if the aspect ratio (h/b) was less than 4. Use of a shrouded, protruding array resulted in plate-average heat transfer coefficients which were from 40—50 percent higher than those obtained for equivalent smooth and parallel channels.

Park and Berglers [34] conducted an experimental study of the natural convection heat transfer characteristics of simulated microelectronic circuits with thin foil heaters arranged in two configurations: flush-mounted on a circuit board substrate or at 1 mm protrusions from the substrate. Heat transfer coefficients were obtained for two heater heights (5 mm and 10 mm) and for varied widths, using both distilled water and R-113 (Freon-TF). The data obtained were compared to those derived from the Fujii and Fujii [6] correlation for laminar boundary layer solutions for a vertical surface with uniform heat flux.

Shakerin et al. [35] conducted both numerical and experimental analyses of laminar natural convection flows adjacent to heated walls with both single and repeated two-dimensional, rectangular roughness element protrusions. While the research focus was directed at the flow and heat transfer process for Pr = 0.7 and Pr = 7, heat transfer effects were determined for varied geometries of protruding roughness elements.

Afrid and Zebib [36] conducted a numerical investigation of the case of conjugate (conduction-convection) natural convection cooling for single, discrete protruding devices compared to three protruding devices mounted on a vertical insulated wall. The effects of changes in selected dimensions and power densities for different devices, subject to constant values for both solid and fluid physical properties, were investigated with respect to the thermal design of printed board assemblies.

Hung and Shiau [37] performed a series of systematic experiments for the measurement of transient natural convective heat fluxes in vertical, parallel plates with rectangular protruding ribs. Based upon their transient heat distribution measurement model, a dimensionless transient convective heat flux was defined. In addition, two generalized correlations for transient convective heat flux were proposed for both the power-on and power-off transient periods. The transient average Nusselt numbers, which were considered to be the key parameter for determining transi-

ent convective heat dissipation in the test channel, were successfully estimated.

Keyhani et al. [38] conducted an experimental investigation of aspect ratio effects upon natural convection heat transfer for rectangular enclosures with five discrete protruding heat sources. The heaters were mounted at uniform vertical spacing on a single vertical wall. An adjustable vertical wall opposite to the wall with the heated sections was placed so that enclosure widths could be varied to desired values. The top surface of the test enclosure was an isothermal heat sink and ethylene glycol was used as the working fluid. Data were collected at steady state for a local modified Rayleigh number (Ra^*) range from 2.4×10^6 to 4.5×10^{10} and local Prandtl numbers varied from 110 to 70.

Lin [39] experimented with natural convection from six rectangular, protruding heated arrays on a vertical channel within an enclosure. Protruding arrays composed of square cross sectional areas were evenly spaced and mounted on the vertical plate. Air, distilled water, and Chevron multimachine oil 68 were employed as working fluids for varied Prandtl numbers. Based upon the array heights, modified Rayleigh numbers were from 1.6×10^5 to 3.8×10^8, whereas the channel space-to-height ratios, b/h, were from 0.104 to 0.567 and without a shrouding wall. Experimental results indicated that heat transfers for large channel spacings (i.e., b/h = 0.567) were not affected by the presence of an

unheated, shrouded wall. Protruding block surface temperatures were lowest for the distilled water medium and highest for the air medium for given identical heat inputs at steady state. Moreover, though only small heat inputs were supplied, the heated block surface temperatures for the air medium by natural convection were higher than expected. These experiments demonstrated that air cooling by means of natural convection would not support the packaging densities and heat flux levels required for a number of modern applications. The most favorable empirical correlation for vertical channels with protruding arrays was

$$Nu_b = 1.3181\left(\frac{b}{h}Ra_b^*\right)^{0.149}, \qquad \text{for } 0.72 < Pr < 1009 . \tag{2-12}$$

Finally, Sathe and Joshi [40] sought a numerical solution for coupled conduction and natural convection transport from a substrate-mounted heat generating protrusion in a liquid-filled square enclosure. The unique feature of these computations was that conduction heat transfer within the protrusion and substrate, as well as coupled natural convection, was considered. Computations for flow and heat transfer were conducted for specified rates of volumetric energy generation within the protrusion. A commercially available dielectric liquid, FC-75, was selected for the working fluid.

CHAPTER 3

THEORETICAL ANALYSIS

Three uniform, plate-mounted (PCB) heat generation protrusions (i.e., chips), and an opposing wall within a fluid-filled cavity, are considered. A schematic sketch of this configuration has been provided in Figure 1.2. The protrusion plates and the fluid have constant transport properties (ν, k, α) and coefficients of thermal expansion (β). The governing equations for the natural convection of the fluid and the coupled conduction processes for specified rates of volumetric energy generation within the protrusions are described in the following sections.

3.1 Principal Assumptions and Governing Equations

Based upon the assumption of a two-dimensional, incompressible, time-dependent laminar flow with negligible viscous dissipation, and invoking the Boussinesq approximations, the governing equations can be defined as follows. For low speed flows that involve small density variations, the well-known Boussinesq approximation is valid. The obvious reason for the use of the Boussinesq approximation is that some simplification of the governing equations is enabled by treating density as a constant for all terms,

with the exception of the body force terms for the momentum equations [41,42]. The governing equations are thus as follows.

1) Working Fluid Region:

Continuity:

$$\frac{\partial u}{\partial x} + \frac{\partial v}{\partial y} = 0 \ . \qquad (3\text{-}1)$$

Momentum:

$$\frac{\partial(\rho_f u)}{\partial t} + \frac{\partial(\rho_f uu)}{\partial x} + \frac{\partial(\rho_f uv)}{\partial y} = -\frac{\partial P^*}{\partial x} + \mu_f\left(\frac{\partial^2 u}{\partial x^2} + \frac{\partial^2 u}{\partial y^2}\right), \qquad (3\text{-}2)$$

$$\frac{\partial(\rho_f v)}{\partial t} + \frac{\partial(\rho_f uv)}{\partial x} + \frac{\partial(\rho_f vv)}{\partial y} = -\frac{\partial P^*}{\partial y} + \mu_f\left(\frac{\partial^2 v}{\partial x^2} + \frac{\partial^2 v}{\partial y^2}\right) + \rho_f g \beta_f (T^* - T_c) \ . \qquad (3\text{-}3)$$

Energy:

$$\frac{\partial(\rho_f T^*)}{\partial t} + \frac{\partial(\rho_f uT^*)}{\partial x} + \frac{\partial(\rho_f vT^*)}{\partial y} = \frac{k_f}{Cp_f}\left(\frac{\partial^2 T^*}{\partial x^2} + \frac{\partial^2 T^*}{\partial y^2}\right) . \qquad (3\text{-}4)$$

2) Protruding Discrete Heating Elements (e.g., chips):

Energy:

$$\rho_{s1} Cp_{s1} \frac{\partial T^*}{\partial t} = k_{s1}\left(\frac{\partial^2 T^*}{\partial x^2} + \frac{\partial^2 T^*}{\partial y^2}\right) + \frac{Q}{Bl_c} \ . \qquad (3\text{-}5)$$

3) Vertical Plates (PCB):

Energy:

$$\rho_{s2} Cp_{s2} \frac{\partial T^*}{\partial t} = k_{s2} \left(\frac{\partial^2 T^*}{\partial x^2} + \frac{\partial^2 T^*}{\partial y^2} \right) . \qquad (3\text{-}6)$$

These equations can be nondimensionalized by the use of channel spacing b as the length scale and

$$(X, Y) = \frac{(x, y)}{b} , \qquad (3\text{-}7)$$

$$(U, V) = \frac{(u, v)}{U_0} , \qquad (3\text{-}8)$$

$$P = \frac{P^*}{\rho_f U_0^2} , \qquad (3\text{-}9)$$

$$T = \frac{T^* - T_c}{(Q/k_f)} , \qquad (3\text{-}10)$$

$$\tau = (U_0/b)\, t , \qquad (3\text{-}11)$$

where x, y, u, v, t, T^*, P, and $U_0 \left(= \left\{ \frac{g\beta Qb}{k_f} \right\}^{\frac{1}{2}} \text{[m/sec]} \right)$ are the physical variables given in Fig. 1.2 and the nomenclature.

The Rayleigh and Prandtl numbers are defined in the usual way:

$$\text{Ra} = \frac{g \beta_f Q b^3}{\alpha_f k_f \nu_f} \qquad (3\text{-}12)$$

and

$$Pr = \frac{\nu}{\alpha} = \frac{\mu_f Cp_f}{k_f} \quad . \tag{3-13}$$

3.2 Dimensionless Governing Equations

The following dimensionless governing equations are from the nondimensional variables given in section 3.1.

1) Working Fluid Region:

Continuity:

$$\frac{\partial U}{\partial X} + \frac{\partial V}{\partial Y} = 0 \quad . \tag{3-14}$$

Momentum:

$$\frac{\partial U}{\partial \tau} + \frac{\partial (UU)}{\partial X} + \frac{\partial (UV)}{\partial Y} = - \frac{\partial P}{\partial X} + \left\{\frac{Pr}{Ra}\right\}^{\frac{1}{2}} \left\{\frac{\partial^2 U}{\partial X^2} + \frac{\partial^2 U}{\partial Y^2}\right\} \quad , \tag{3-15}$$

$$\frac{\partial V}{\partial \tau} + \frac{\partial (UV)}{\partial X} + \frac{\partial (VV)}{\partial Y} = - \frac{\partial P}{\partial Y} + \left\{\frac{Pr}{Ra}\right\}^{\frac{1}{2}} \left\{\frac{\partial^2 V}{\partial X^2} + \frac{\partial^2 V}{\partial Y^2}\right\} + T \quad . \tag{3-16}$$

Energy:

$$\frac{\partial T}{\partial \tau} + \frac{\partial (UT)}{\partial X} + \frac{\partial (VT)}{\partial Y} = \left\{\frac{1}{Ra\, Pr}\right\}^{\frac{1}{2}} \left\{\frac{\partial^2 T}{\partial X^2} + \frac{\partial^2 T}{\partial Y^2}\right\} \quad . \tag{3-17}$$

2) Protruding Discrete Heating Elements (e.g., chips):

Energy:

$$\frac{\partial T}{\partial \tau} = R_1^* \left[R_1 \left\{ \frac{1}{\mathrm{Pr\,Ra}} \right\}^{\frac{1}{2}} \left\{ \frac{\partial^2 T}{\partial X^2} + \frac{\partial^2 T}{\partial Y^2} \right\} + \left\{ \frac{1}{\mathrm{Pr\,Ra}} \right\}^{\frac{1}{2}} \left\{ \frac{1}{G_B F_c} \right\} \right] . \tag{3-18}$$

3) Vertical Plates (PCB):

Energy:

$$\frac{\partial T}{\partial \tau} = R_2^* \left[R_2 \left\{ \frac{1}{\mathrm{Pr\,Ra}} \right\}^{\frac{1}{2}} \left\{ \frac{\partial^2 T}{\partial X^2} + \frac{\partial^2 T}{\partial Y^2} \right\} \right] . \tag{3-19}$$

For purposes of analysis, the following nondimensional variables are introduced:

$$(R_1, R_2) = \frac{(k_{s1}, k_{s2})}{k_f} , \tag{3-20}$$

$$(R_1^*, R_2^*) = \frac{\rho_f Cp_f}{(\rho_{s1} Cp_{s1}, \rho_{s2} Cp_{s2})} , \tag{3-21}$$

$$(G_B, F_c) = \frac{(B, l_c)}{b} . \tag{3-22}$$

Total field governing equations, which are for the combined fluid and solid regions, are as follows. Note that the conservation differential equations are valid throughout the entire computational domain, and that in the solid regions, velocities are maintained equal to zero, thus reducing the energy equation to pure conduction.

1) Total Governing Equations for the Computational Domain:

Continuity:

$$\frac{\partial U}{\partial X} + \frac{\partial V}{\partial Y} = 0 \ . \qquad (3\text{-}14)$$

X-Momentum:

$$\frac{\partial U}{\partial \tau} + \frac{\partial (UU)}{\partial X} + \frac{\partial (UV)}{\partial Y} = -\frac{\partial P}{\partial X} + \left\{\frac{\mathrm{Pr}}{\mathrm{Ra}}\right\}^{\frac{1}{2}} \left\{\frac{\partial^2 U}{\partial X^2} + \frac{\partial^2 U}{\partial Y^2}\right\} . \qquad (3\text{-}15)$$

Y-Momentum:

$$\frac{\partial V}{\partial \tau} + \frac{\partial (UV)}{\partial X} + \frac{\partial (VV)}{\partial Y} = -\frac{\partial P}{\partial Y} + \left\{\frac{\mathrm{Pr}}{\mathrm{Ra}}\right\}^{\frac{1}{2}} \left\{\frac{\partial^2 V}{\partial X^2} + \frac{\partial^2 V}{\partial Y^2}\right\} + T . \qquad (3\text{-}16)$$

Energy:

$$\frac{\partial T}{\partial \tau} + \frac{\partial (UT)}{\partial X} + \frac{\partial (VT)}{\partial Y} = R^* \left[R \left\{\frac{1}{\mathrm{Ra\,Pr}}\right\}^{\frac{1}{2}} \left\{\frac{\partial^2 T}{\partial X^2} + \frac{\partial^2 T}{\partial Y^2}\right\} + S^* \left\{\frac{1}{\mathrm{Pr\,Ra}}\right\}^{\frac{1}{2}} \left\{\frac{1}{G_B F_c}\right\} \right] . \qquad (3\text{-}23)$$

2) The energy source term is:

$S^* = 0$, for the fluid and vertical plates (i.e., where no heat is generated; and

$S^* = 1$, for the heated elements.

3) The ratio of thermal conductivity is:

$R = 1$, in the fluid;

$R = R_1$, in the heated blocks; and

$R = R_2$, in the vertical plates.

4) The ratio of properties, R^*, is:

$R^* = 1$, in the fluid;

$R^* = R^*_1$, in the heated elements; and

$R^* = R^*_2$, in the vertical plates.

Equations (3-14)—(3-16) and (3-23) are subject to the following initial and boundary conditions:

For $\tau = 0$: $T = 0$, $U = V = 0$, for all domains;

For $\tau > 0$: $U = V = 0$, for the heated elements, vertical plates, and all cavity walls; and

$T = 0$, for all cavity walls.

CHAPTER 4

NUMERICAL PROCEDURES

Numerical solutions for the dimensionless governing equations were obtained using the control volume formulation described by Patankar [3] and the simplified marker-and-cell (SMAC) algorithm [4] proposed for the numerical solution of time-dependent, viscous flow problems for incompressible fluids. The SMAC algorithm is significantly easier to use and has been applied to investigations of the dynamics of given flow problems for several space dimensions. When comparison data have been available, results obtained from the use of this method have generally been in good agreement with experimental results. The current study was based upon concepts first presented in consideration of the SMAC. For each time step, momentum equations are solved explicitly, whereas pressure equations are solved implicitly and the energy equation is solved semi-implicitly. The basis of computation is to separate each calculation cycle into three phases [43].

The calculation cycle procedure is outlined as follows:

- Phase I, the Tilde Phase: Two momentum equations are advanced in dimensionless time ($\tau + \Delta\tau$) to

obtain approximate (tilde) velocities $(\tilde{U}, \tilde{V})$, based on the previous-time values of dimensionless pressure P and temperature T. Although these values of the velocity components satisfy the momentum equations, based upon the current values of P and T, continuity is usually not satisfied.

- Phase II, the Implicit Phase: The dimensionless velocity components and the dimensionless pressure corrections (U', V', P') are obtained from the elliptic equation, which satisfies the continuity equation $(\nabla \cdot \vec{U} = 0)$. For this phase, a potential function is employed, determined by the requirement that it is capable of converting the velocity field to a form which everywhere satisfies the incompressibility condition, or

$$U(\tau + \Delta\tau) = \tilde{U}(\tau) + U' , \tag{4-1}$$

$$V(\tau + \Delta\tau) = \tilde{V}(\tau) + V' \tag{4-2}$$

and

$$P(\tau + \Delta\tau) = P(\tau) + P' . \tag{4-3}$$

- Phase III, the Scalar Phase: Using the previously computed values of $U(\tau + \Delta\tau)$ and $V(\tau + \Delta\tau)$, the advanced time $(\tau + \Delta\tau)$ for dimensionless temperature, $T(\tau + \Delta\tau)$ and other scalar quantities are computed.

The solution is advanced step-by-step in time by continued application of the three solution phases.

4.1 Tilde Phase

4.1.1 Tilde Velocities

Using summation conventions, the rearrangement of the dimensionless governing equations is as follows:

1) Continuity:

$$\frac{\partial U_i}{\partial X_i} = 0 \ , \tag{4-4}$$

2) Momentum:

$$\frac{\partial U_i}{\partial \tau} + \frac{\partial (U_i U_j)}{\partial X_j} = -\frac{\partial P}{\partial X_i} + M \frac{\partial}{\partial X_j} \left\{ \frac{\partial U_i}{\partial X_j} \right\} + \delta_{2i} T \ , \tag{4-5}$$

and

3) Energy:

$$\frac{\partial T}{\partial \tau} + \frac{\partial (U_j T)}{\partial X_j} = R^* \cdot N \frac{\partial}{\partial X_j} \left(\frac{\partial T}{\partial X_j} \right) + S_0 \ , \qquad (i, j = 1, 2) \tag{4-6}$$

where

$$M = \left\{ \frac{\mathrm{Pr}}{\mathrm{Ra}} \right\}^{\frac{1}{2}} \ , \tag{4-7}$$

$$N = R \left\{ \frac{1}{\mathrm{Pr} \cdot \mathrm{Ra}} \right\}^{\frac{1}{2}} \ , \tag{4-8}$$

and

$$S_0 = R^* \left\{ \frac{1}{\mathrm{Pr\,Ra}} \right\}^{\frac{1}{2}} \left\{ \frac{1}{G_B \cdot F_c} \right\} S^* \ . \qquad (4\text{-}9)$$

For the prototype differential, the form of the momentum equation is

$$\frac{\partial U_i}{\partial \tau} + \frac{\partial}{\partial X_j} \left\{ U_i U_j - M \frac{\partial U_i}{\partial X_j} \right\} = - \frac{\partial P}{\partial X_i} + \delta_{2i} T \ . \qquad (4\text{-}10)$$

For the prototype finite volume, the form is

$$V_0 \frac{\partial U_i}{\partial \tau} + \sum_j A_j \left\{ U_j U_i - M \frac{\partial U_i}{\partial X_j} \right\} = S_{U_i} \ , \qquad (4\text{-}11)$$

where

$$S_{U_i} = V_0 \left\{ - \frac{\partial P}{\partial X_i} + \delta_{2i} T \right\}$$

and V_0 is the cell volume. The time advancement form of the above equation may be written as a forward difference yielding,

$$\frac{V_0}{\Delta \tau} \left(U_i^{n+1} - U_i^n \right) + \sum_j A_j \left\{ U_j U_i - M \frac{\partial U_i}{\partial X_j} \right\} = S_{U_i} \ . \qquad (4\text{-}12)$$

where $i, j = 1, 2$.

4.1.2 Pressure-Velocity Method

The pressure-velocity approach is most commonly used for low speed flows, but it is appropriate for all flow speeds. Three partial differential equations are needed for the solution of the pressure field, P, and the two velocity components, U_1 and U_2 (or U, V). The Navier-

Stokes equations provide two equations, but with the unknowns P, U and V. The two momentum equations (i.e., parabolic PDEs) are used to solve the velocity components and the continuity equation is used to solve for pressure (i.e., an elliptic PDE).

Using a means to time-advance the pressure field in conjunction with the velocity field so that pressure is included implicitly in equation (4-12), the velocity U_i^{n+1} is

$$U_i^{n+1} = U_i^n + \frac{\Delta\tau}{V_0}\left\{-A_i(\Delta_{\boldsymbol{i}} P^{n+1}) + \dot{S}_{U_i}^n\right\} , \qquad (4\text{-}13)$$

where the fourth term in this case is

$$\dot{S}_{U_i}^n = -\sum_j A_j \left\{U_j U_i - M\frac{\partial U_i}{\partial X_j}\right\} + V_0\,\delta_{2i}\,T . \qquad (4\text{-}14)$$

At this point, start by separating the velocity vector into the rotational part $(\tilde{U}_m)$ and the irrotational part (U_m') ,

$$U_m^{n+1} = \tilde{U}_m + U_m' ,$$

where $m = 1,2$ and $P^{n+1} = P^n + P'$, and then

$$\begin{aligned} U_m^{n+1} = \tilde{U}_m + U_m' &= U_m^n + \frac{\Delta\tau}{V_0}\left\{-A_m\Delta_{\boldsymbol{m}}(P^n + P') + \dot{S}_{U_m}^n\right\} \\ &= U_m^n + \frac{\Delta\tau}{V_0}\left\{-A_m\Delta_{\boldsymbol{m}} P^n + \dot{S}_{U_m}^n\right\} - \frac{\Delta\tau}{V} A_m\Delta_{\boldsymbol{m}} P' , \end{aligned} \qquad (4\text{-}15)$$

where the bold $\boldsymbol{m}$ indicates that the summation rule is suspended. The symbol, $\tilde{U}$, indicates a provisional dimensionless velocity, based upon the latest value computed for the pressure field.

For the provisional time-advanced dimensionless velocity field,

$$\tilde{U}_m = U_m^n + \frac{\Delta\tau}{V_0}\left[-A_m(\Delta_m P^n) + \dot{S}_{U_m}^n\right] \qquad (4\text{-}16)$$

and the dimensionless velocity correction is

$$U_m' = -\frac{\Delta\tau}{V_0} A_m(\Delta_m P') \ , \qquad (4\text{-}17)$$

where

$$\dot{S}_{U_m}^n = -\sum_j A_j\left\{U_j U_m - M\frac{\partial U_m}{\partial X_j}\right\} + V_0\,\delta_{2m}T \ . \qquad (m, j = 1,2)$$

4.1.3 Finite Volume Form of the Continuity Equation

The finite volume continuity form is expressed as

$$\sum_I A_I U_I = 0 \ . \qquad (I = 1,2) \qquad (4\text{-}18)$$

Assuming that the numerical procedure converges at the advanced time step $n + 1$, then the continuity for the time step is satisfied as

$$\sum_I A_I U_I^{n+1} \cong 0 \ . \qquad (4\text{-}19)$$

Thus,

$$\sum_I A_I(\tilde{U}_I + U_I') = 0 \qquad (4\text{-}20)$$

and

$$\sum_I A_I U_I' = -\sum_I A_I \tilde{U}_I = -\tilde{D} \ , \qquad (4\text{-}21)$$

where $\tilde{D}$ is a known value based upon the provisional velocity fields $(\tilde{U})$ and $(\tilde{V})$.

4.2 Implicit Phase

4.2.1 Divergence

The divergence tilde, $\tilde{D}$, is computed, using the tilde velocities,

$$\sum_I A_I \tilde{U}_I = \tilde{D} \ . \tag{4-22}$$

The velocity correction, U_I' , which is the irrotational part for the next time step from equation (4-17), is dependent upon pressure change. Thus, it may be known that the dimensionless velocity corrections are simply the gradients of the scalar potential

$$U_I' = -\frac{\partial \Phi}{\partial X_I} \ . \tag{4-23}$$

Equations (4-23) and (4-17) define the relationship between pressure change and velocity change. The differential form of equation (4-17) is

$$\begin{aligned} U_I' &= -\Delta\tau \frac{\partial}{\partial X_I}(P') = -\frac{\partial \Phi}{\partial X_I} \\ &= -\frac{\partial}{\partial X_I}(\Delta\tau P') \ . \qquad (I = 1, 2) \end{aligned} \tag{4-24}$$

Thus

$$\Phi = \Delta\tau P' \qquad \text{or} \qquad P' = \frac{\Phi}{\Delta\tau} \ , \tag{4-25}$$

and from equations (4-21) and (4-23),

$$\sum_I A_I U_I' = \sum_I A_I \left(-\frac{\partial \Phi}{\partial X_I} \right) = -\tilde{D} .$$

Therefore,

$$\sum_I A_I \left(\frac{\partial \Phi}{\partial X_I} \right) = \tilde{D} . \qquad (4\text{-}26)$$

Equation (4-21) with equation (4-23)can be expressed in the differential form

$$\frac{\partial}{\partial X_I} \left(\frac{\partial \Phi}{\partial X_I} \right) = \nabla^2 \Phi = \frac{\partial \tilde{U}}{\partial X} + \frac{\partial \tilde{V}}{\partial Y} = \tilde{D} . \qquad (4\text{-}27)$$

To find Φ to satisfy the above elliptic equation by the iteration method, start $\Phi^{m+1} = \Phi^m + \Phi'$, where

$$\begin{aligned} \nabla^2 \Phi^{m+1} &= \nabla^2 (\Phi^m + \Phi') = \tilde{D} , \\ \nabla^2 \Phi' &= \tilde{D} - \nabla^2 \Phi^m = E^m , \end{aligned} \qquad (4\text{-}28)$$

and where E^m is the error of the mth iteration.

As soon as Φ' is updated, then Φ can be updated, until the point that the small error criterion is satisfied. Following the mth iteration, Φ' , which satisfies the error criterion, can be found when $\Sigma \mid E_m \mid < \xi$, where ξ is the convergence criterion.

4.2.2 Update U^{n+1}, V^{n+1} and P^{n+1}

The implicit changes U', V', and P' are calculated with the values of $\Phi_{i,j}$,

$$U_I' = -\frac{\partial \Phi}{\partial X_I} , \qquad P' = \frac{\Phi}{\Delta \tau} , \qquad I=1,2 , \qquad (4\text{-}29)$$

The advanced values of the velocity U_I^{n+1} and the pressure P^{n+1} are then updated,

$$U_I^{n+1} = \tilde{U}_I + U_I' = \tilde{U}_I - \frac{\partial \Phi}{\partial X_I} \qquad (4\text{-}30)$$

and

$$P^{n+1} = P^n + P' = P^n + \frac{\Phi}{\Delta \tau} . \qquad (4\text{-}31)$$

4.3 Scalar Phase (update dimensionless temperature, T^{n+1})

From equation (4-6), the prototype differential equation for the energy equation,

$$\frac{\partial T}{\partial \tau} + \frac{\partial}{\partial X_j}\left\{U_j T - R^* \cdot N \frac{\partial T}{\partial X_j}\right\} = S_0 , \qquad (j = 1,2) \qquad (4\text{-}32)$$

for the prototype finite volume form is

$$V_0 \frac{\partial T}{\partial \tau} + \sum_I A_I \left\{U_I T - R^* \cdot N \frac{\partial T}{\partial X_I}\right\} = V_0 S_0 . \qquad (I=1,2)$$

(4-33)

The time advancement form of the above equation may be written as a forward difference, yielding

$$\frac{V_0}{\Delta \tau}\left(T^{n+1} - T^n\right) = -\sum_I A_I \left\{U_I^{n+1} T^n - R^* \cdot N \frac{\partial T^n}{\partial X_I}\right\} + V_0 S_0^n .$$

(4-34)

The update temperature is

$$T^{n+1} = T^n + \frac{\Delta\tau}{V_0}\left\{-\sum_I A_I\left(U_I^{n+1}T^n - R^*\cdot N\frac{\partial T^n}{\partial X_I}\right) + V_0 S_0^n\right\}, \tag{4-35}$$

for $I = 1,2$ where

$$N = R\left\{\frac{1}{\mathrm{Pr\,Ra}}\right\}^{\frac{1}{2}}, \quad \text{and}$$
$$S_0 = R^*\left\{\frac{1}{\mathrm{Pr\,Ra}}\right\}^{\frac{1}{2}}\left\{\frac{1}{G_B F_c}\right\}\cdot S^* .$$

4.4 Coordinate and Grid System

Two-dimensional rectangular coordinates were chosen for this study. For this system, the common subscripts i and j indicate positions in, respectively, the x- and y-directions. To distinguish between the scalar and vector quantities, a staggered grid system was chosen [3].

In staggered grids, velocity components are calculated at the faces of the control volumes. Thus, from Figure 4.1, the x-direction velocity U is calculated at the faces that are normal to the x-direction. The lines indicate the control volume surfaces. All of the scalar variables, that is, temperature, pressure, and streamfunction, are located at the cell center, while the vector variables, the velocities, are located at the cell faces. It is necessary to define U and V momentum cells to obtain velocities from the discretization of the momentum equation since the veloci-

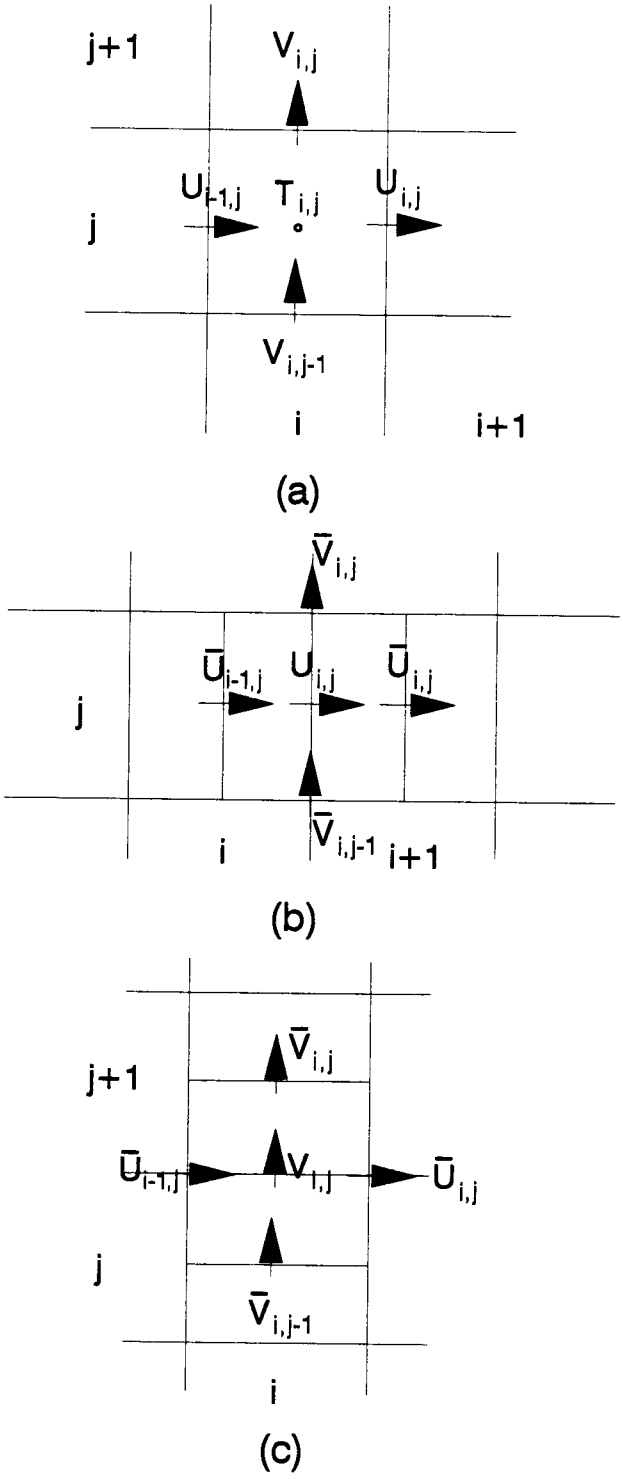

Fig. 4.1 Staggered grid variables: (a) continuity cell; (b) *U*-momentum cell; and (c) *V*-momentum cell.

ties are located at the cell faces of the continuity cell. For a typical control volume, it may easily be seen that the discretized continuity equation contains the differences between adjacent velocity components.

4.5 Discretization of the Governing Equation

4.5.1 Discretization of Momentum Equations

From equations (4-13) and (4-14), the momentum equations can be divided into four terms (i.e., the inertial, viscous, pressure, and gravity terms). Each term is discretized for the purpose of determining the tilde velocities ($\tilde{U}$ and $\tilde{V}$) .

a) Inertial term:

The inertial term of the momentum equation is discretized by application of the upwind method. For example, in Figure 4.2 this includes the unequally-spaced U-momentum cell surface velocities ($\overline{U}$ and $\overline{V}$) . The discrete form of the inertial term for the U-momentum cell is

$$\begin{aligned}\sum_l A_l U_l U = \frac{\Delta y_{i,j}}{2} \{ &(|\overline{U}_{i,j}| + \overline{U}_{i,j}) U_{i,j} - (|\overline{U}_{i,j}| - \overline{U}_{i,j}) U_{i+1,j} \\ &- (|\overline{U}_{i-1,j}| + \overline{U}_{i-1,j}) U_{i-1,j} + (|\overline{U}_{i-1,j}| - \overline{U}_{i-1,j}) U_{i,j} \} \\ &+ \left\{ \frac{\Delta x_{i,j} + \Delta x_{i+1,j}}{4} \right\} \{ (|\overline{V}_{i,j}| + \overline{V}_{i,j}) U_{i,j} \\ &- (|\overline{V}_{i,j}| - \overline{V}_{i,j}) U_{i,j+1} - (|\overline{V}_{i,j-1}| + \overline{V}_{i,j-1}) U_{i,j-1} \\ &+ (|\overline{V}_{i,j-1}| - \overline{V}_{i,j-1}) U_{i,j} \}\end{aligned}$$

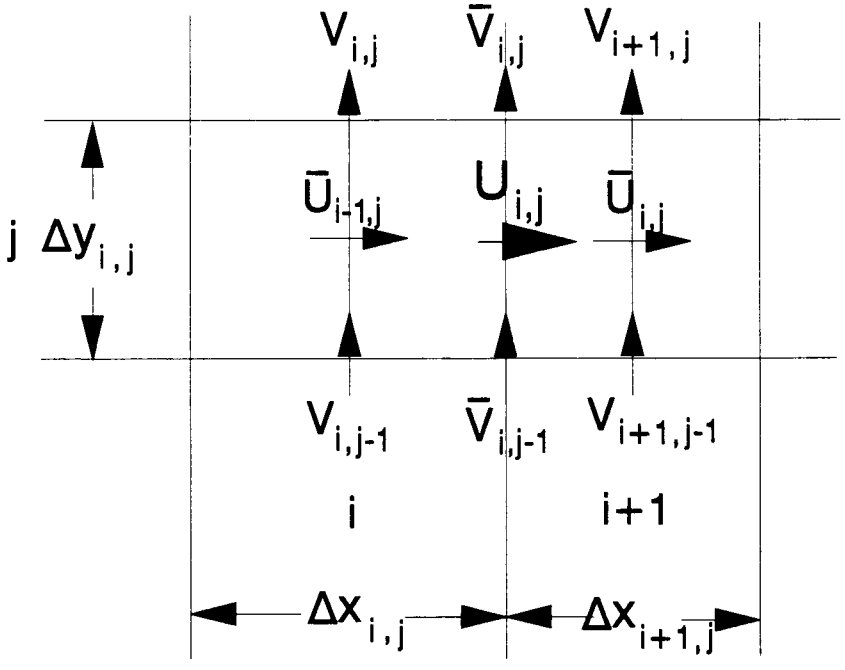

Fig. 4.2 Unequally spaced U-momentum cell with velocities ($\overline{U}$ and $\overline{V}$) .

where $A_1 = \Delta y(i,j)$ and $A_2 = \frac{\Delta x_{i,j} + \Delta x_{i+1,j}}{2}$. In an unequally-spaced grid system, the U-momentum cell surface velocities ($\overline{U}$ and $\overline{V}$) can be shown according to the following interpolations:

$$\overline{U}_{i,j} = \frac{U_{i,j} + U_{i+1,j}}{2} ,$$

$$\overline{U}_{i-1,j} = \frac{U_{i-1,j} + U_{i,j}}{2} ,$$

$$\overline{V}_{i,j} = V_{i,j} + \left(\frac{\Delta x_{i,j}}{\Delta x_{i,j} + \Delta x_{i+1,j}} \right) (V_{i+1,j} - V_{i,j}) ,$$

$$\overline{V}_{i,j-1} = V_{i,j-1} + \left(\frac{\Delta x_{i,j}}{\Delta x_{i,j} + \Delta x_{i+1,j}} \right) (V_{i+1,j-1} - V_{i,j-1}) .$$

b) Viscous term:

The viscous term from equation (4-11) is discretized for the unequally-spaced U-momentum cell. From Figure 4.3, the viscous term of the finite control volume form for the U-momentum cell can be expressed as follows, where $J1$ and $J2$ are the momentum fluxes at the designated cell face for the U-momentum cell,

$$\sum_I A_I \left\{ M \frac{\partial U}{\partial x_I} \right\} = A_1 \{ J1_{i,j} - J1_{i-1,j} \} + A_2 \{ J2_{i,j} - J2_{i,j-1} \}$$

$$= A_{1_{i+1,j}} \frac{M_{i+1,j}}{\Delta x_{i-1,j}} (U_{i+1,j} - U_{i,j}) + A_{1_{i,j}} \frac{M_{i,j}}{\Delta x_{i,j}} (U_{i,j} - U_{i-1,j})$$

$$+ \left\{ \frac{\Delta x_{i,j} + \Delta x_{i+1,j}}{2} \right\} \left\{ CM2_{i,j} + \left(\frac{\Delta x_{i,j}}{\Delta x_{i,j} + \Delta x_{i+1,j}} \right) \times (CM2_{i+1,j} - CM2_{i,j}) \right\} (U_{i,j+1} - U_{i,j})$$

$$+ \left\{ \frac{\Delta x_{i,j-1} + \Delta x_{i+1,j-1}}{2} \right\} \left\{ CM2_{i,j-1} + \left(\frac{\Delta x_{i,j-1}}{\Delta x_{i,j-1} + \Delta x_{i+1,j-1}} \right) \times (CM2_{i+1,j-1} - CM2_{i,j-1}) \right\} (U_{i,j} - U_{i,j-1}) ,$$

for I = 1,2 and where $CM2$, the finite volume connector, is related to the corresponding gradient of U-momentum for each cell in the computational grid system as

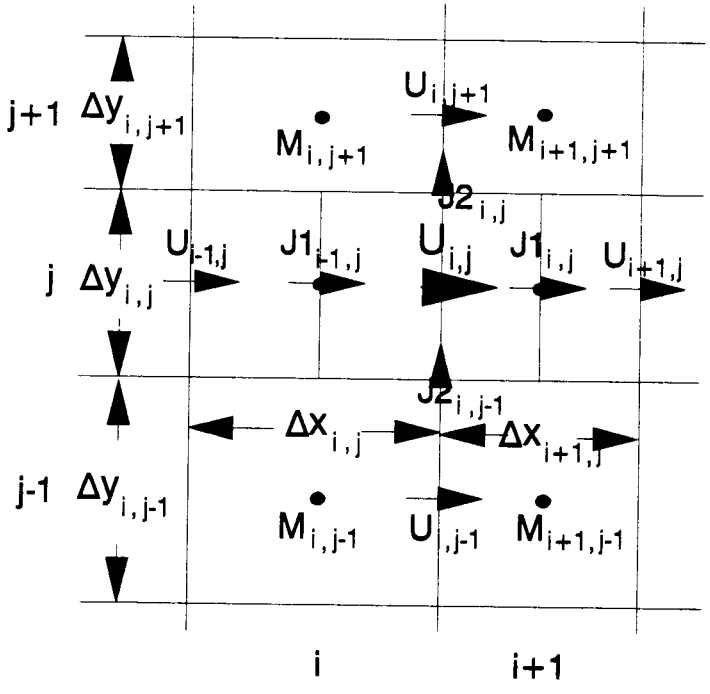

Figure 4.3 Unequally spaced *U*-momentum cell and momentum flux *J*1 and *J*2 at the *U*-momentum cell surface.

$$CM2_{i,j} = \frac{2}{\frac{\Delta y_{i,j}}{M_{i,j}} + \frac{\Delta y_{i,j+1}}{M_{i,j+1}}} \quad .$$

c) Pressure term:

From equation (4-13), the pressure term for the control volume form in the x-direction can be discretized as

$$A_{1_{i,j}} \Delta_x P = \Delta y_{i,j} \left(P_{i+1,j} - P_{i,j} \right) \ ,$$

where $A_{1_{i,j}} = \Delta y_{i,j}$.

d) Gravity term:

From the governing equation, there is no external force in the x-direction. From equation (4-14), the V-momentum equation has only a gravity term. The unequally-spaced V-momentum cell for the gravity term is shown in Figure 4.4. The discrete form of the gravity term of the control volume $(V_0 T)$ is

$$V_0 T = V_{0_{i,j}} \left\{ T_{i,j} + \left(\frac{\Delta y_{i,j}}{\Delta y_{i,j} + \Delta y_{i,j+1}} \right) (T_{i,j+1} - T_{i,j}) \right\} .$$

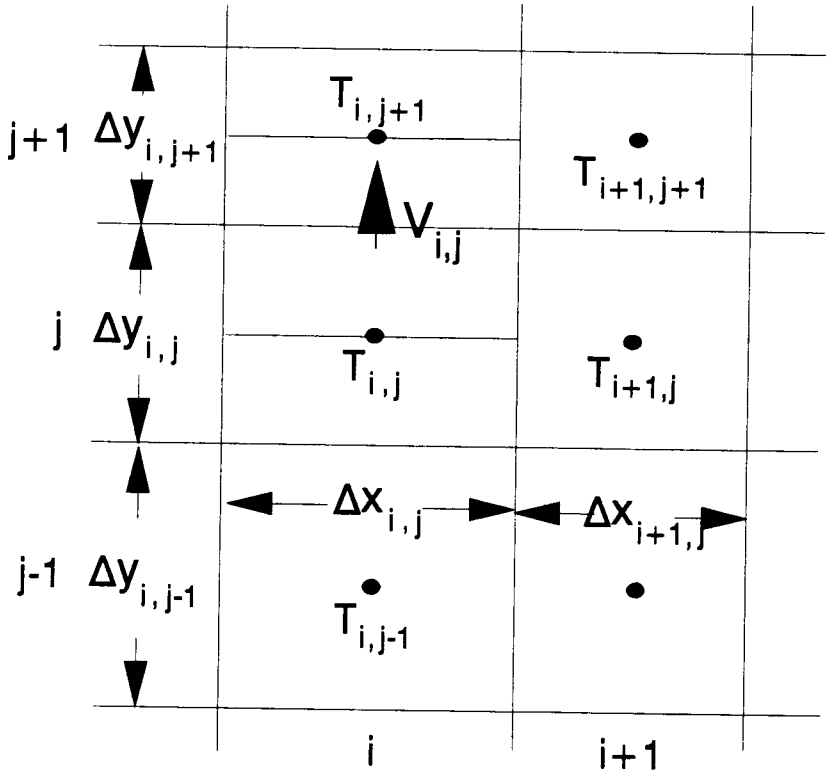

Fig. 4.4 Unequally-spaced V-momentum cell for gravity term.

4.5.2 Discretization of Continuity Equation

To satisfy the continuity equation, the dimensionless velocity U_m^{n+1} is expressed in the following forms:

1) As an integral, $\int_{c.s.} (\vec{V}\cdot\vec{n})\, dA = 0$; and

2) As a finite volume, $\sum_I A_I U_I^{n+1} = 0$.

A potential function is employed to determine the velocity corrections (U', V') . The continuity cells which satisfy the continuity equation, with the potential variable $\Phi_{i,j}$, are shown in Figure 4.5.

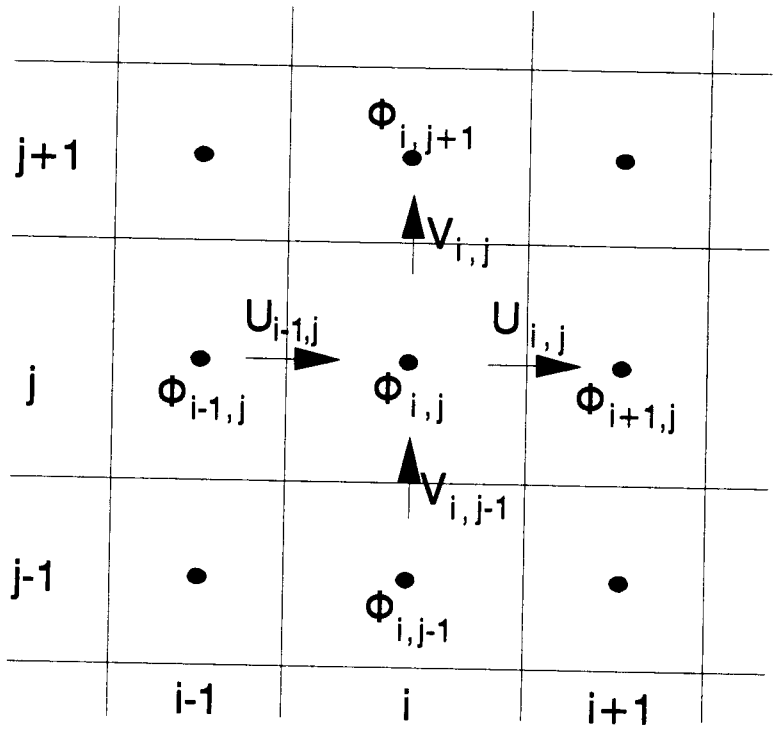

Fig. 4.5 Continuity cell with potential variable Φ .

From equations (4-19) and (4-21),

$$A_{1_{i,j}} U_{i,j}^{n+1} - A_{1_{i+1,j}} U_{i-1,j}^{n+1} + A_{2_{i,j}} V_{i,j}^{n+1} - A_{2_{i,j-1}} V_{i,j-1}^{n+1} = 0$$

and

$$A_{1_{i,j}} (U'_{i,j} - U'_{i-1,j}) + A_{2_{i,j}} (V'_{i,j} - V'_{i,j-1})$$
$$= -A_{1_{i,j}} (\tilde{U}_{i,j} - \tilde{U}_{i-1,j}) - A_{2_{i,j}} (\tilde{V}_{i,j} - \tilde{V}_{i,j-1}) = -\tilde{D} ,$$

where $\tilde{D}$ is the divergence from the previous time-step values.

By the discretization of equation (4-21), for the definition $U'_l = -\frac{\partial \Phi}{\partial x_l}$,

$$C1_{i,j} \Phi_{i+1,j} + C1_{i-1,j} \Phi_{i-1,j} + C2_{i,j} \Phi_{i,j+1} + C2_{i,j-1} \Phi_{i,j-1}$$
$$- \{C1_{i,j} + C1_{i-1,j} + C2_{i,j} + C2_{i,j-1}\} \Phi_{i,j} = \tilde{D}_{i,j} ,$$

where

$$C1_{i,j} = \frac{A_{1_{i,j}}}{\frac{\Delta x_{i,j}}{\eta_{i,j}} + \frac{\Delta x_{i+1,j}}{\eta_{i+1,j}}} \quad \text{and} \quad C2_{i,j} = \frac{A_{2_{i,j}}}{\frac{\Delta y_{i,j}}{\eta_{i,j}} + \frac{\Delta y_{i,j+1}}{\eta_{i,j+1}}} ,$$

and where $\eta_{i,j}$ is always 1.0 for the fluid region at the computational domain, but for a solid cell should be a small value (e.g., $10^{-50} \approx$ zero) to satisfy the boundary condition.

4.5.3 Discretization of the Energy Equation

From equation (4-33), the energy equation can be divided into three terms (i.e., convection, conduction, and heat source terms). Each term is discretized for the purpose of determining the dimensionless temperature.

a) Convection term:

Figure 4.6 illustrates discretization of the convection term for the temperature cell using the upwind method. From equation (4-35), the convection term for the energy equation is

$$\sum_l A_l U_l^{n+1} T^n = \frac{A_{1_{i,j}}}{2}\{(|U_{i,j}| + U_{i,j})\, T_{i,j} - (|U_{i,j}| - U_{i,j})\, T_{i+1,j} - (|U_{i-1,j}| + U_{i-1,j})\, T_{i-1,j} + (|U_{i-1,j}| - U_{i-1,j})\, T_{i,j}\} + \frac{A_{2_{i,j}}}{2}\{(|V_{i,j}| + V_{i,j})\, T_{i,j} - (|V_{i,j-1}| - V_{i,j})\, T_{i,j+1} - (|V_{i,j-1}| + V_{i,j-1})\, T_{i,j-1} + (|V_{i,j-1}| - V_{i,j-1})\, T_{i,j}\}.$$

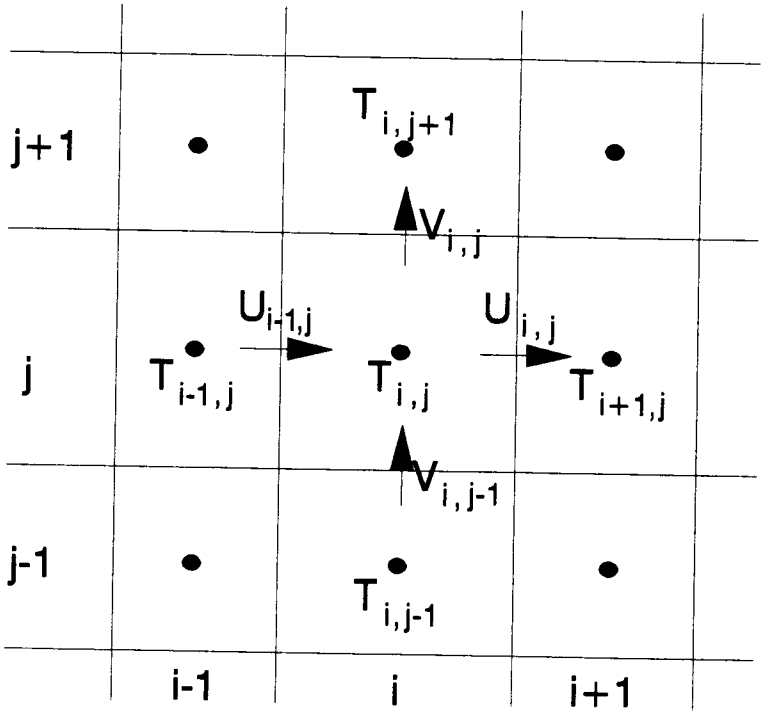

Fig. 4.6 Temperature cell for discretization of the convection term using the upwind method.

b) Conductive term:

Figure 4.7 shows the temperature cell for discretization of the conduction term. For the energy equation, the conduction term with heat fluxes ($J1^*$ and $J2^*$) is:

$$\sum_I A_I\left(N\frac{\partial T^n}{\partial x_I}\right) = A_1\left\{J1^*_{i,j} - J1^*_{i-1,j}\right\} + A_2\left\{J2^*_{i,j} - J2^*_{i,j-1}\right\}$$

$$= A_{1_{i,j}}\left\{\frac{2}{\frac{\Delta x_{i,j}}{N_{i,j}} + \frac{\Delta x_{i+1,j}}{N_{i+1,j}}}\left(T_{i+1,j} - T_{i,j}\right)\right.$$

$$\left. - \frac{2}{\frac{\Delta x_{i-1,j}}{N_{i-1,j}} + \frac{\Delta x_{i,j}}{N_{i,j}}}\left(T_{i,j} - T_{i-1,j}\right)\right\}$$

$$+ A_{2_{i,j}}\left\{\frac{2}{\frac{\Delta y_{i,j}}{N_{i,j}} + \frac{\Delta y_{i,j+1}}{N_{i,j+1}}}\left(T_{i,j+1} - T_{i,j}\right)\right.$$

$$\left. - \frac{2}{\frac{\Delta y_{i,j-1}}{N_{i,j-1}} + \frac{\Delta y_{i,j}}{N_{i,j}}}\left(T_{i,j} - T_{i,j-1}\right)\right\},$$

for $I = 1,2$ where

$$N_{i,j} = R_{i,j}\left\{\frac{1}{\mathrm{Pr\,Ra}}\right\}^{\frac{1}{2}} .$$

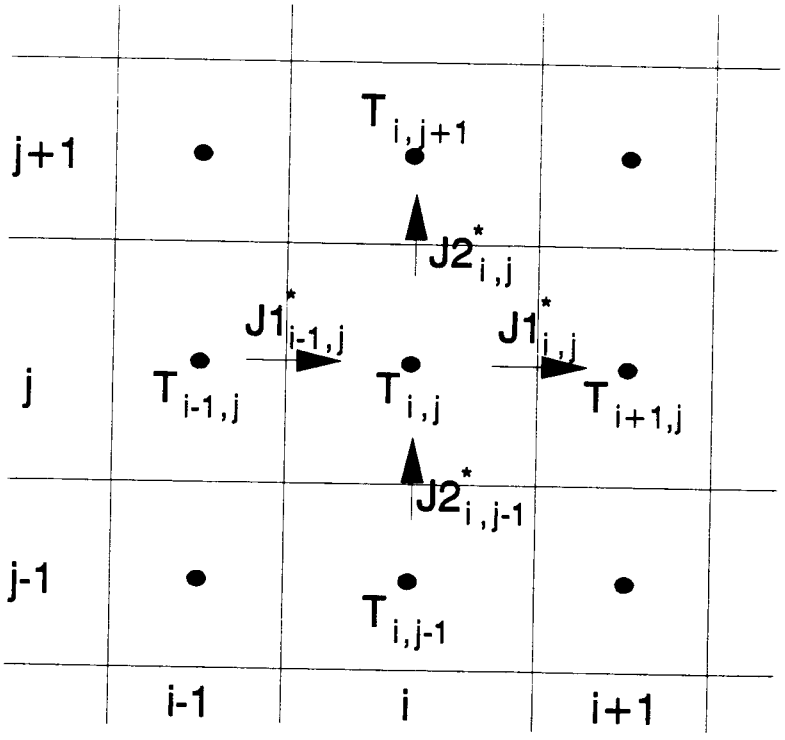

Figure 4.7 Temperature cell for discretization of the conduction term with heat flux ($J1^*$ and $J2^*$) .

c) Heat source term:

When the cell has a heat source, the heat source term for the energy equation must be calculated as

$$V_0 S_0^n = \Delta x_{i,j} \cdot \Delta y_{i,j} S_0^n ,$$

where

$$S_0 = R^*_{i,j} \left\{ \frac{1}{\mathrm{Pr}\ Ra} \right\}^{\frac{1}{2}} \left\{ \frac{1}{G_B F_c} \right\} S^*_{i,j} .$$

4.6 Connector Logic for the Boundaries

The connectors developed for the finite-volume equations provide a convenient, flexible and powerful mechanism for cell development in the computational grid system, enabling boundary conditions to be set at any type. The explanation for this mechanism resides in the variety of parameters provided within the construction of the connector coefficients, $CX_{i,j}$, and a heat source which can be manipulated to achieve the desired effect.

For example, consider a two-dimensional, steady-state heat conduction problem for a solid material, as shown in Figure 4.8. The finite volume connector, $CX_{i,j}$, is related to the corresponding gradient of $T^*_{i,j}$ for each cell through the cell boundary. That is, the connectors relate the heat fluxes $(J1_{i,j}, J2_{i,j})$ between adjacent computation cells for the diffusion processes [43].

By using the steady-state conservation law, applied to finite-volume cells with the heat source, $S_{i,j}$, the energy equation can be expressed as:

$$(J1_{i,j} - J1_{i-1,j}) + (J2_{i,j} - J2_{i,j-1}) = -V_{0_{i,j}} S_{i,j} , \qquad (4\text{-}36)$$

where $J1$ and $J2$ are heat fluxes through the surfaces of cell i, $V_{0_{i,j}}$ is the volume of cell i,j, and $S_{i,j}$ is the heat source at cell i,j. Using Fourier's law, which expresses the heat fluxes $(J1, J2)$,

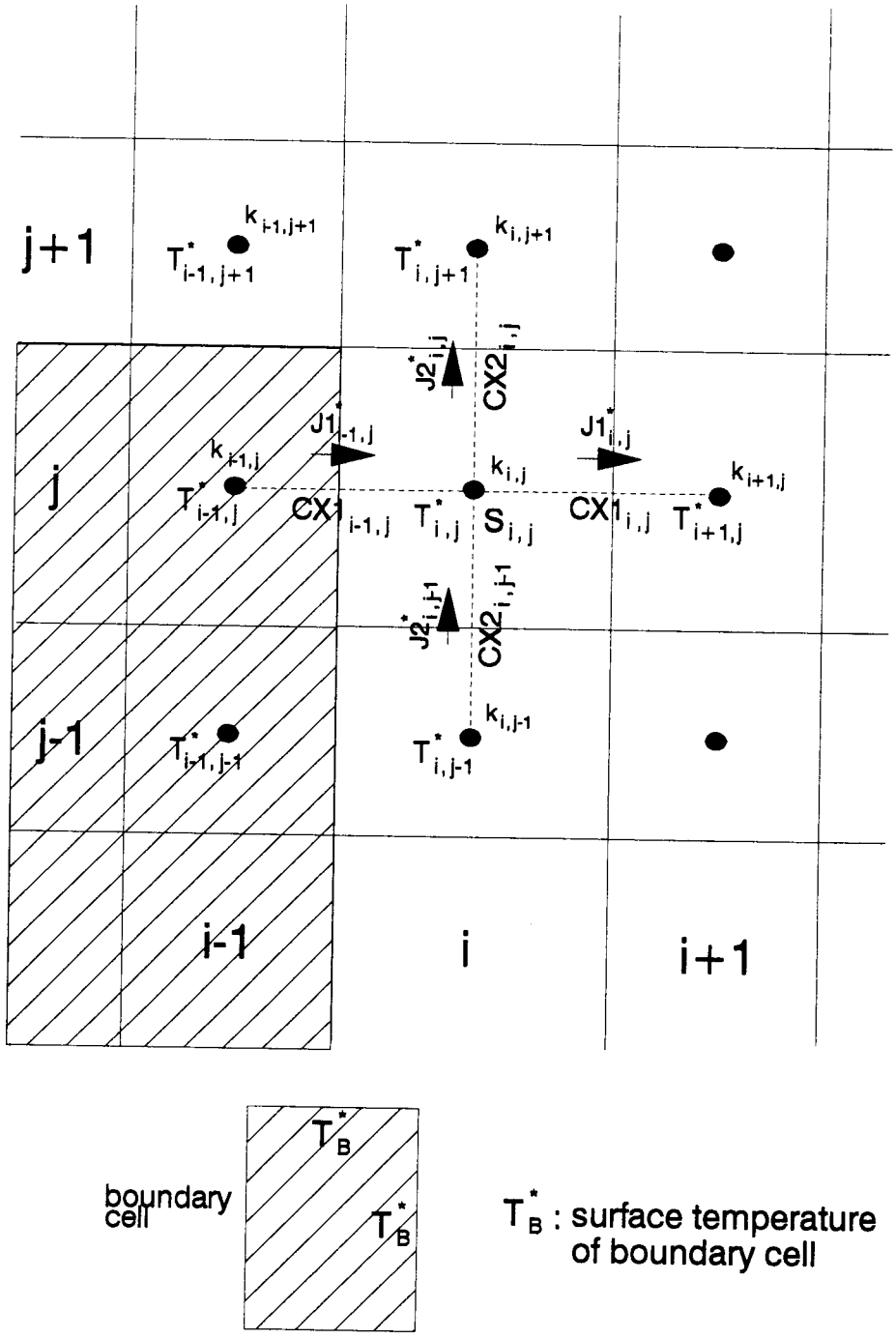

Figure 4.8 Connector example at five points for diffusion process with boundary cells.

$$\left\{\frac{\Delta y_{i,j}\,(T^*_{i+1,j} - T^*_{i,j})}{\frac{\Delta x_{i,j}}{2k_{i,j}} + \frac{\Delta x_{i+1,j}}{2k_{i+1,j}}} - \frac{\Delta y_{i-1,j}\,(T^*_{i,j} - T^*_{i-1,j})}{\frac{\Delta x_{i-1,j}}{2k_{i-1,j}} + \frac{\Delta x_{i,j}}{2k_{i,j}}}\right\}$$

$$+ \left\{\frac{\Delta x_{i,j}\,(T^*_{i,j+1} - T^*_{i,j})}{\frac{\Delta y_{i,j}}{2k_{i,j}} + \frac{\Delta y_{i,j+1}}{2k_{i,j+1}}} - \frac{\Delta x_{i,j-1}\,(T^*_{i,j} - T^*_{i,j-1})}{\frac{\Delta y_{i,j-1}}{2k_{i,j-1}} + \frac{\Delta y_{i,j}}{2k_{i,j}}}\right\}$$

$$= -V_{0_{i,j}} S_{i,j} \,. \tag{4-37}$$

By setting the connectors $CX1_{i,j}$ and $CX2_{i,j}$,

$$CX1_{i,j} = \frac{2\Delta y_{i,j}}{\frac{\Delta x_{i,j}}{k_{i,j}} + \frac{\Delta x_{i+1,j}}{k_{i+1,j}}}\,, \tag{4-38}$$

$$CX2_{i,j} = \frac{2\Delta x_{i,j}}{\frac{\Delta y_{i,j}}{k_{i,j}} + \frac{\Delta y_{i,j+1}}{k_{i,j+1}}}\,, \tag{4-39}$$

the diffusion equation can then be expressed as

$$CX1_{i,j}\,(T^*_{i+1,j} - T^*_{i,j}) - CX1_{i-1,j}\,(T^*_{i,j} - T^*_{i+1,j}) + CX2_{i,j}\,(T^*_{i,j+1} - T^*_{i,j}) - CX2_{i,j-1}\,(T^*_{i,j} - T^*_{i,j-1}) = -V_{0_{i,j}} S_{i,j} \,. \tag{4-40}$$

Rearranging equation (4-40),

$$CX1_{i,j}\,T^*_{i+1,j} + CX1_{i-1,j}\,T^*_{i-1,j} + CX2_{i,j}\,T^*_{i,j+1} + CX2_{i,j-1}\,T^*_{i,j-1} - (CX1_{i,j} + CX1_{i-1,j} + CX2_{i,j} + CX2_{i,j-1})\,T^*_{i,j} = -V_{0_{i,j}} S_{i,j} \,. \tag{4-41}$$

This equation represents the finite volume discretization of the diffusion equation, often referred to as the finite volume form of the elliptic equation.

Two types of boundary conditions are generally used. The first case is a fixed value for the transport variable at the boundary, the so-called Dirichlet boundary condition. The second case is the fixed value for the gradient of transport variable at the boundary, the so-called Neumann boundary condition. For example, from Fig. 4.8, if the boundary cell surface temperature is known and is constant, $T^*_{i-1,j}$, it should be equal to T^*_B , which is $T^*_{constant}$. Thus,

$$T^*_{i-1,j} = T^*_B = T^*_{constant} \quad . \tag{4-42}$$

To satisfy equation (4-42), it is obvious that the connector $CX1_{i-1,j}$ from equation (4-37) should be changed as follows:

$$CX1_{i-1,j} = \frac{2\Delta y_{i-1,j}}{\frac{\Delta x_{i,j}}{k_{i,j}}} \quad . \tag{4-43}$$

By setting $k_{i-1,j}$ at such a "large number" (10^{30}), it is easy to change equation (4-38) to satisfy the boundary condition.

Consider an insulated boundary condition at the boundary surface ($J1_B = 0$) . From Fig. 4.8, the heat flux $J1_{i-1,j}$ is equal to zero at the boundary surface. There are two methods of satisfying the boundary condition. From Fig. 4.8, an obvious method is to set $T^*_{i-1,j} = T^*_{i,j}$, which works well in one-dimensional space. However, in the two-dimensional situation given in Fig. 4.8, $T^*_{i-1,j}$ and

$T_{i-1,j+1}$ will generally have different values. Thus, $T^*_{i-1,j}$ cannot equal $T^*_{i,j}$ and $T^*_{i-1,j+1}$ at the same time to achieve the boundary condition. Therefore, a conditional check must be performed to determine the value of $T^*_{i-1,j}$ through computation. Since the conditional statements inhibit compiler optimization and generally consume excess computer time, this is an inefficient method of setting boundary conditions. The other method, which maximizes computer efficiency, is to set the connector at the boundary cell to zero to ensure that the flux is zero. Flux $J1_{i-1,j}$ will be zero if the connector $CX1_{i-1,j}$ is zero. This connector variable can be set at zero by the logical definition of the material conductivity $k_{i-1,j}$ at a small number (e.g., 10^{-30}) to satisfy the boundary condition.

4.7 Stability Condition

To obtain the dimensionless values $\tilde{U}$, $\tilde{V}$, and T from the momentum and energy equations, explicit methods are used. Treatment of the two-dimensional heat transfer problem considered in the current investigation requires a stability condition, or one which makes the explicit method stable:

$$\Delta\tau \le \mathrm{Min}\left\{\frac{1}{\frac{|U_{i,j}|}{\Delta X_{i,j}} + \frac{|V_{i,j}|}{\Delta Y_{i,j}} + 2\cdot CMAX\left(\frac{1}{\Delta X^2_{i,j}} + \frac{1}{\Delta Y^2_{i,j}}\right)}\right\}$$

$$CMAX = \mathrm{MAX}\left(\left\{\frac{\mathrm{Pr}}{\mathrm{Ra}}\right\}^{\frac{1}{2}},\ R^*_{i,j}\cdot R_{i,j}\left\{\frac{1}{\mathrm{Pr}\cdot\mathrm{Ra}}\right\}^{\frac{1}{2}}\right). \qquad (4\text{-}44)$$

The time-step $\Delta\tau$ must satisfy equation (4-44) to assure the stability of the explicit computations. Therefore, the conservative factor 0.95 is multiplied by $\Delta\tau$ to assure stability.

4.8 Nusselt Number, Rayleigh Number and Stream Function

To compute a Nusselt number at the heated protruding surface, reference length and temperature are selected. Since concern is directed at the effect of the channel aspect ratio, the channel spacing, b, was selected as the reference length for the present study. The ambient fixed temperature, T_c, which was the surface temperature of the enclosure, was selected as the reference temperature. Thus, the local Nusselt number at the heated surface was nondimensionalized for the heat flux q'' :

$$Nu_{local} = \frac{q'' b}{(T^*|_{surface} - T_c) k_f} . \qquad (4\text{-}45)$$

The heat flux q'' for the heated block surface in the channel direction, based upon the Fourier law, can be calculated as:

$$q'' = -k \frac{\partial T^*}{\partial x}\bigg|_{surface} .$$

Based upon this derivation, q'' is computed in consideration of the following staggered grid system:

where

$$q'' = \frac{T^*_{sl} - T^*_f}{\frac{(\Delta x_{sl})}{2} + \frac{(\Delta x_f)}{2}} \quad , \qquad (4\text{-}46)$$

T^*_{sl} = dimensional temperature of the heated device surface,

T^*_f = dimensional temperature of the fluid cell nearest to the heated device surface,

Δx_{sl} = dimensional cell space for T^*_{sl} in the x-direction, and

Δx_f = dimensional cell space for T^*_f .

However, the local Nusselt number can also be computed for dimensionless values, obtained from the dimensionless governing equations as

$$Nu_{local} = \frac{\left\{ \frac{T_{sl} - T_f}{\left(\frac{1}{R_1}\right)\frac{\Delta X_{sl}}{2} + \frac{\Delta X_f}{2}} \right\}}{\left\{ T_{sl} - (T_{sl} - T_f)\left(\frac{\Delta X_{sl}}{\Delta X_{sl} + R_1 \Delta X_f}\right) \right\}} \quad , \qquad (4\text{-}47)$$

where

$$T_{sl} = \frac{T^*_{sl} - T_c}{(Q/k_f)} \quad ,$$

$$R_1 = \frac{k_{sl}}{k_f} \quad ,$$

$$\Delta X_{sl} = \frac{\Delta x_{sl}}{b} \quad ,$$

and

$$\Delta X_f = \frac{\Delta x_f}{b} .$$

The instanteous height-average Nusselt number for each protruding heated device surface in the streamwise direction is then defined as

$$Nu_{b,each} = \frac{1}{B} \int_0^B Nu_{local}\, dy . \qquad (4\text{-}48)$$

Similarly, the channel Rayleigh numbers are defined by two differing concepts, Q and q'' , respectively, based upon the heat input or source in the heated device and the heat flux from the heated block surface, where q'' is used to define the modified Rayleigh number:

1) Rayleigh number:

$$Ra_b = \frac{g\beta Q b^3}{\alpha_f \nu_f k_f} . \qquad (4\text{-}49)$$

2) Modified Rayleigh number:

$$Ra_b^* = \frac{g\beta \overline{q}'' b^4}{\alpha_f \nu_f k_f} . \qquad (4\text{-}50)$$

One problem in obtaining the modified Rayleigh number is the difficulty of calculating average heat flux at the heated surface in the streamwise direction $\overline{q}''$. For reason of the conduction effects in the heated device, heat flux at the heated device surface in the streamwise direction cannot be strictly uniform, and will rather reflect variation in accordance with the block surface. Thus, the average heat flux at the heated block is calculated as

$$\overline{q}'' = \frac{2}{B}\sum_{j}\left(\frac{T^{*}_{sl,j} - T^{*}_{f,j}}{\frac{\Delta x_{sl,j}}{k_{sl}} + \frac{\Delta x_{f,j}}{k_{f}}}\right)\Delta y_{j} \ . \qquad (4\text{-}51)$$

The dimensionless streamfunction $\Psi(X,Y)$ is defined by

$$\frac{\partial \Psi}{\partial Y} = U \ , \qquad (4\text{-}52)$$

$$\frac{\partial \Psi}{\partial X} = -V \ . \qquad (4\text{-}53)$$

Either equation (4-52) or (4-53) can be used to determine $\Psi(X,Y)$. Expressing the dimensionless velocity U in the finite difference form, and referring to the grid, the first relation is

$$U_{i,j} = \frac{\Psi_{i,j+1} - \Psi_{i,j}}{\Delta Y_{i,j}} \ ,$$

and thus,

$$\Psi_{i,j+1} = \Psi_{i,j} + U_{i,j}\Delta Y_{i,j} \ . \qquad (4\text{-}54)$$

4.9 Determination of a Steady-State Solution

If an electronic system is switched on and left running for lengthy periods of time, subject to constant power requirements, then the temperature of the electronic components and their mounting structures, including the PCBs, will stabilize. Sampling temperature and velocity values for selected grid locations demonstrates how this steady-state may be attained. Figures 4.9 and 4.10, respectively,

demonstrate variations for dimensionaless temperature, T, and the dimensionless velocities, U and V, at selected locations over dimensional time. To demonstrate progression to steady-state temperature, three different locations were selected (Fig. 4.9), for which the observed velocity variations were considered (Fig. 4.10). From the information presented, it is apparent that a steady-state was attained in approximately 1,000 sec. The confirmed steady-state results provided in the current investigation are based upon this common approach, and the observations as presented in Figures 4.9 and 4.10.

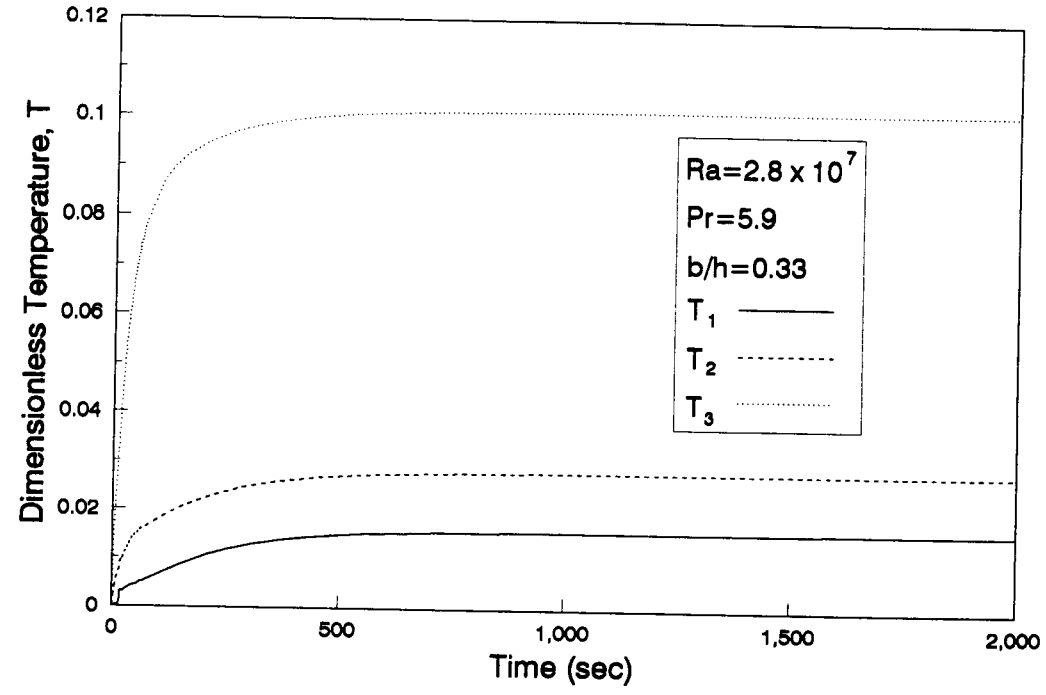

Figure 4.9 Dimensionless temperature evolution at selected locations to determine steady-state.

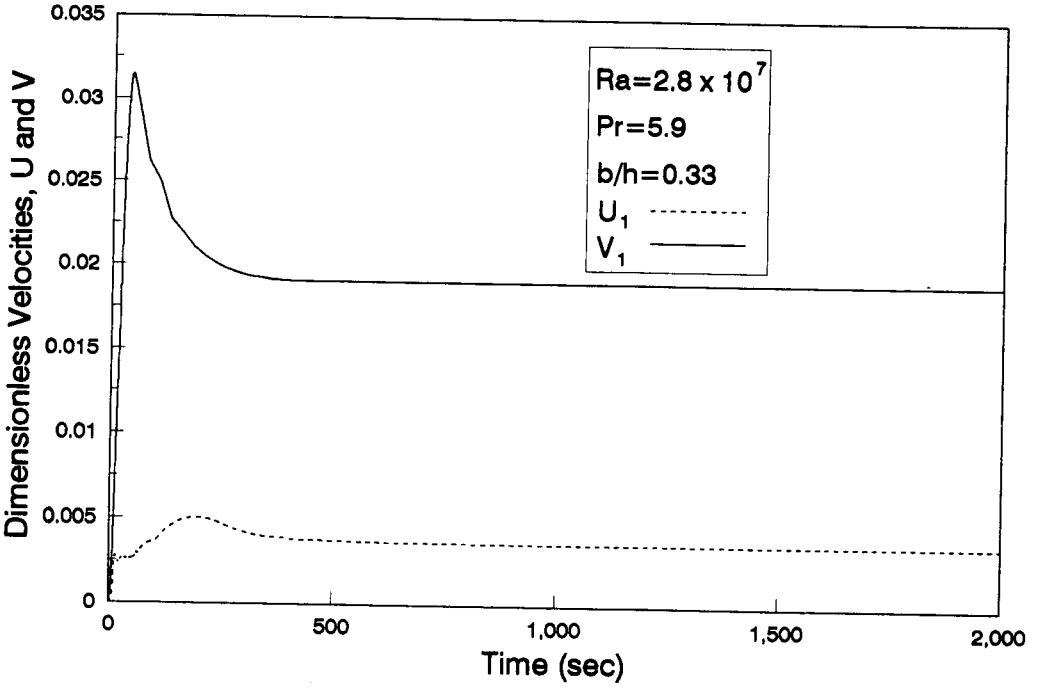

Figure 4.10 Dimensionless velocity evolution at selected locations to determine steady-state.

CHAPTER 5

NUMERICAL EXPERIMENTAL APPARATUS AND PROCEDURE

5.1 Scope

As an alternative to matching the characteristics and the shapes of complex systems of electronic components on a host circuit board in real situations, the present study is directed at obtaining accurate numerical data from the analysis of a two-dimensional, coupled conduction and natural convection model with the general geometric features and cooling fluid properties of electronic systems. The purpose of this numerical study of a research model was to improve the current state of knowledge of the processes of thermal and fluid dissipation from microelectronic systems. To complete the experiment, the most important issue was the means to determine a selection of reasonable material properties for both solids and fluids. This process is discussed in the following two sections: First, the selection of a working fluid as coolant capable of supporting the heat flux levels required in contemporary electronic equipment; second, the selection of solid materials for heat generating blocks, including the IC chips and the vertical PCB plates.

5.2 Selection and Properties of Coolant Liquids

There are numerous candidates as dielectric coolants for the modern electronic cooling systems, including air, distilled water, fluorochemicals, and ethylene glycol. The principal advantages of cooling with air are its availability and ease of application. Air cooling is frequently used for applications with low power and low packaging densities. However, air cooling is generally used more often for forced convection than for natural convection systems. For example, Lin [39], by experimentation, demonstrated that heated block surfaces air-cooled by natural convection remained too hot even when relatively small heat inputs were supplied. This indicated that air cooling by means of natural convection would not support the packaging densities and heat flux levels required in at least certain modern technologies.

In point of fact, electronic cooling capabilities can be significantly improved when liquid cooling means are used. Liquid cooling applications can generally be categorized as either indirect or direct. For direct liquid cooling, the electronics or the packages within which they are housed are placed within direct and intimate contact with the cooling liquid. Direct liquid cooling provides the opportunity to remove heat directly from the IC chip or from the surface of the heat generating device, thus transferring excess heat into the liquid in the virtual absence

of any intervening thermal conduction resistance path. In recent years, there has been considerable interest in direct liquid cooling. Machines such as the CRAY-2 supercomputer now use this cooling approach.

The selection of a coolant for liquid cooling applications has been subject to frequent investigation and discussion. In this section, several of those studies which have addressed natural convection liquid cooling are considered as reasonable choices from among commercially or otherwise available dielectric fluids. Park and Bergles [34] developed an experimental investigation of liquid (water and R-113) natural convection heat transfer characteristics, using thin foil heaters to simulate microelectronic chips. Keyhani et al. [30,38] experimentally investigated the aspect ratio effect on natural convection heat transfer with discrete and protruding heat sources placed in ethylene glycol. Joshi and Paje [44] presented an experimental investigation of natural convection heat transfer from a commercially available semiconductor device packaged with FC-75. Sathe and Joshi [40] conducted a numerical examination of coupled heat transfer from a substrate-mounted heat generating protrusion in FC-75.

Based upon recommendations derived from the studies cited above, from among available dielectric fluids, the selected working fluid coolants considered in the present study were distilled water, FC-75, and ethylene glycol. Commercially available electronic equipment items are com-

monly cooled with either water, water and ethylene glycol, or fluorochemicals (e.g., FC-75). As a convenient reference, and to illustrate the effect of coolant selection on heat transfer capabilities, coolant thermal properties for each type considered in the present study are tabulated in Table 5.1.

Table 5.1 Properties of various dielectric cooling liquids.

Thermal Property	Distilled Water	FC-75	Ethylene Glycol
Density (Kg/m^3)	997.0	1758.8	1103.7
Thermal conductivity (W/m^oK)	0.608	0.064	0.255
Specific heat (J/Kg^oK)	4177.0	1038.3	2460.0
Viscosity ($Pa \circ sec$)	0.857×10^{-3}	1.4427×10^{-3}	1.07×10^{-2}
Thermal diffusivity (m^2/sec)	1.460×10^{-7}	0.3505×10^{-7}	0.939×10^{-7}
Kinematic viscosity (m^2/sec)	0.8600×10^{-6}	0.8203×10^{-6}	9.65×10^{-6}
Thermal expansion ($1/^oK$)	2.7594×10^{-4}	1.6×10^{-3}	0.65×10^{-3}

Sources: [45,46,47].

With respect to density, viscosity, thermal conductivity, and specific heat from the cooling standpoint, water is probably the best liquid available. For long-term

operations, distilled water that has been deionized is generally used. However, distilled water suffers from the limitations of low boiling temperature, the capacity to freeze at temperatures below 0°C, and poor electrical insulation capabilities.

A fluorochemical manufactured by the 3M Company, FC-75 is a liquid with approximately the same viscosity as water. This liquid has a specific heat which is approximately one-fourth that of water, and it provides excellent dielectric characteristics. FC-75 is usable over a temperature range from -65°C to 100°C. In contrast, the thermal conductivity of ethylene glycol is lower than that for water. Commercially, this liquid is used for antifreeze mixtures of 62% ethylene glycol and 38% water. The mixture of ethylene glycol and water provides degraded thermal performance, but it will not freeze until a temperature of -65°C is reached, which is the lowest limit of U.S. military requirements.

5.3 Selection and Properties of Heated Blocks and Plates

The choice of solid materials for heated blocks and plates was an important consideration for the present study. Since thermal conduction is the principal path for heat flow to heated blocks, the thermal conductivity of heated blocks to simulate electronic heated packages was a property of principal interest. Current generations of electronic components are packaged in a wide variety of

shapes and sizes, both with and without electrical lead wires, in plastic cases.

The protruding blocks which provided the heat dissipation function for the present study were considered from the viewpoint of a wide variety of microelectronic devices. These types of blocks primarily dissipate most of the heat generated into adjacent liquids. The heat may be directly injected into the coolant or it may be injected through the PCB board. In a typical semiconductor plastic package, silicon IC chips are generally covered by a plastic semiconductor molding compound. The thermal conductivity of this molding compound plays a significant role in the ability of the package to transport heat away from the heated package source.

In the present study, the Dow Corning 306 molding compound, a commercially available product, was selected to simulate the properties of heated blocks [48]. The selected material for plates (PCB) was an epoxy fiberglass in common use. Table 5.2 summarizes selected solid properties for heated blocks and plates for purposes of numerical simulation. The computational parameters required to solve the dimensionless governing equation can be obtained from the properties of the liquids and solids (i.e., the conductivity ratio between the fluids and the solids, as well as the Prandtl number). Table 5.3 displays the computational parameters for each liquid considered.

Table 5.2 Solid properties of selected heated arrays (electronic package) and plates (PCB).

	Material	Property	Value
Heated Block (Elect. Package)	Dow Corning 306 Molding Compound [48]	Density (Kg/m^3)	1880
		Thermal Conductivity (W/m^oK)	0.6276
		Specific heat (J/Kg^oK)	1256
		Thermal diffusivity (m^2/sec)	2.6579×10^{-7}
Plate (PCB)	Epoxy Fiberglass [45]	Density (Kg/m^3)	1800
		Thermal Conductivity (W/m^oK)	0.2594
		Specific heat (J/Kg^oK)	1256
		Thermal diffusivity (m^2/sec)	1.1474×10^{-7}

Table 5.3 Computational parameters for solving the dimensionless governing equations.

Liquid	Parameters		
	Ratio of conductivity, heated block to liquid (k_{s1}/k_f)	Ratio of conductivity, plate to liquid (k_{s2}/k_f)	Pr
Distilled water	1.032	0.427	5.88
FC-75	9.806	4.053	23.40
Ethylene glycol	2.461	1.017	103.00

CHAPTER 6

RESULTS AND DISCUSSION

6.1 Scope

Velocity and temperature profiles derived from numerical computations, as well as consideration of the heat transfer results and the effects of liquid cooling properties, are presented in this chapter. Flow patterns and the temperature distributions from natural convection processes, and conduction through heated devices with varied channel spacings, are represented by streamlines and isothermal lines. Optimal channel spacing to height ratios, for the purpose of reducing the high temperatures which exist on heated element surfaces in streamwise directions, according to changes in channel spacing, are investigated. Plots for the heat source input, Q, generated from each protruding element in relation to the temperature differences, ΔT, between the highest temperatures on the protruding surfaces in the streamwise direction and the constant cold enclosure temperature for various cooling liquids, are used to suggest the cooling abilities of each coolant considered. The heat transfer correlation equations are proposed from the following functional forms expressed as the dimensionless parameters

$$Nu_b = f\left(\left(\frac{b}{h}\right)Ra_b^*\right)$$

and

$$Nu_b = f\left(\left(\frac{b}{h}\right)Ra_b\right) .$$

6.1 Temperature Distributions for Protruding Discrete Heated Element Surfaces

The steady-state temperature distributions for the heated device element surfaces in the streamwise direction are considered. The locations with the highest temperatures are situated within the protruding heated element IC or modules with heat sources. However, heated block surface temperature distributions were investigated for reason of specific interest in the effects of the convective heat transfers which take place between the cooling fluids and the surfaces of the heated devices.

6.1.1 Comparison of Protruding Heated Element Surface Temperature Profiles at Various Heat Inputs for Each Liquid

The different heat inputs for identical channel spacing to height ratios are shown in Figures 6.1 to 6.8 for protruding heated surface temperature profiles for the different cooling liquids. In each figure, the dimensionless temperatures, T, and the dimensionless lengths, y'/s , or

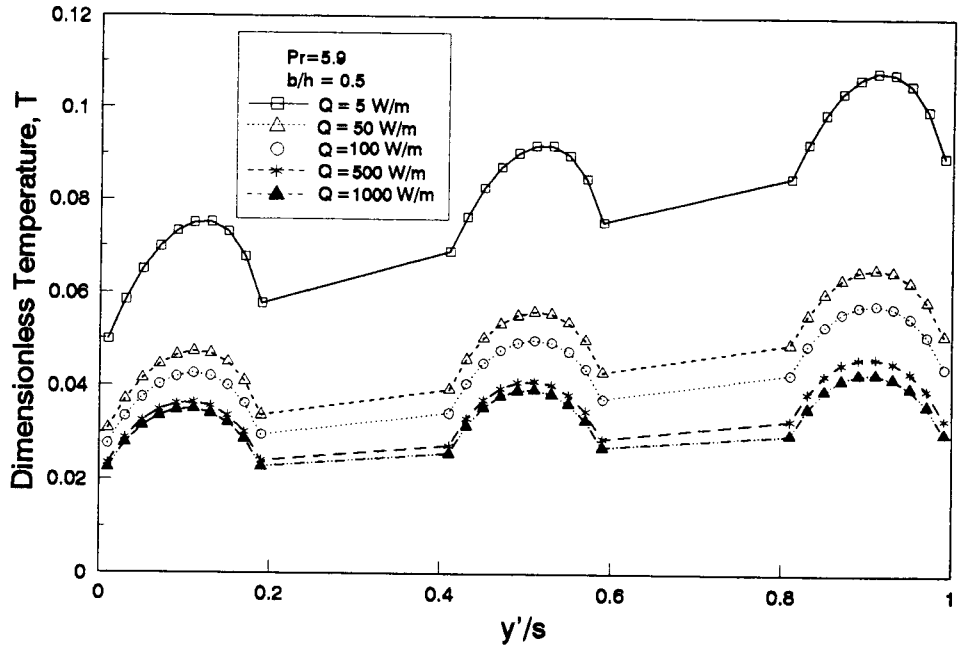

Figure 6.1 T versus y'/s for various Q, (b/h) = 0.5 for water.

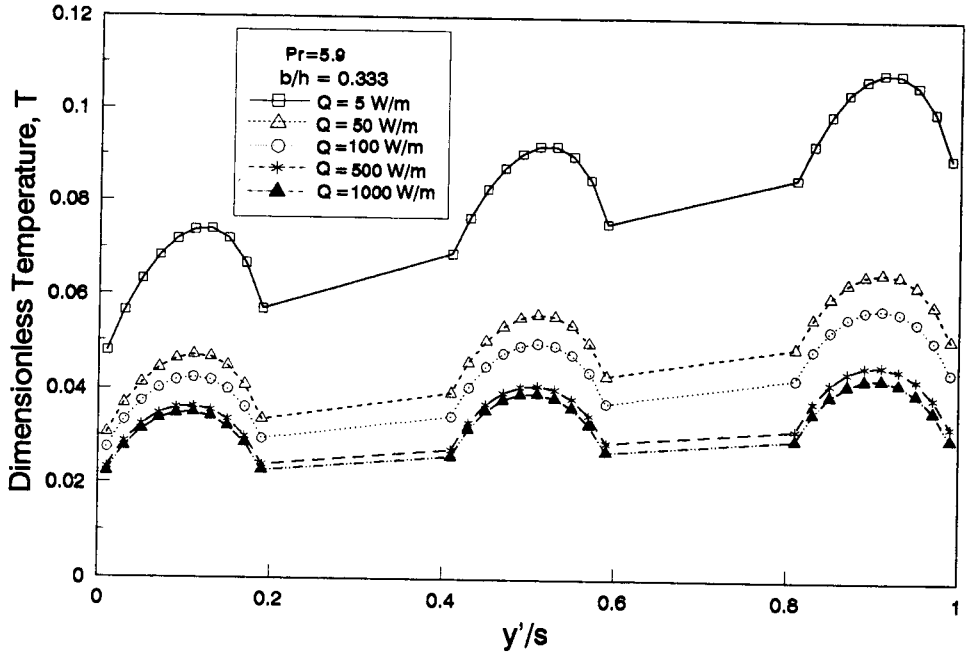

Figure 6.2 T versus y'/s for various Q, (b/h) = 0.333 for water.

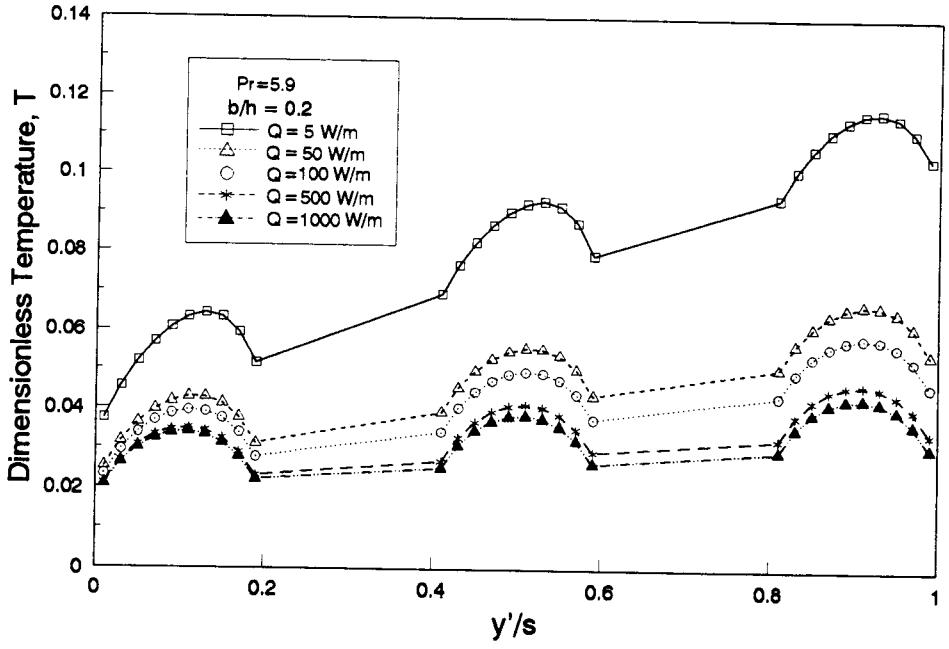

Figure 6.3 T versus y'/s for various Q, (b/h) = 0.2 for water.

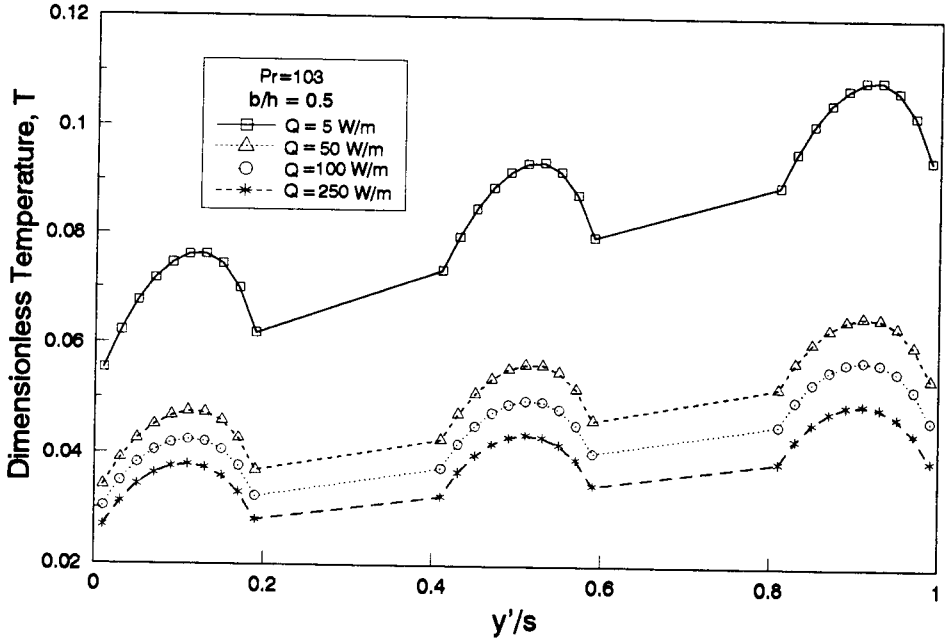

Figure 6.4 T versus y'/s for various Q, (b/h) = 0.5 for ethylene glycol.

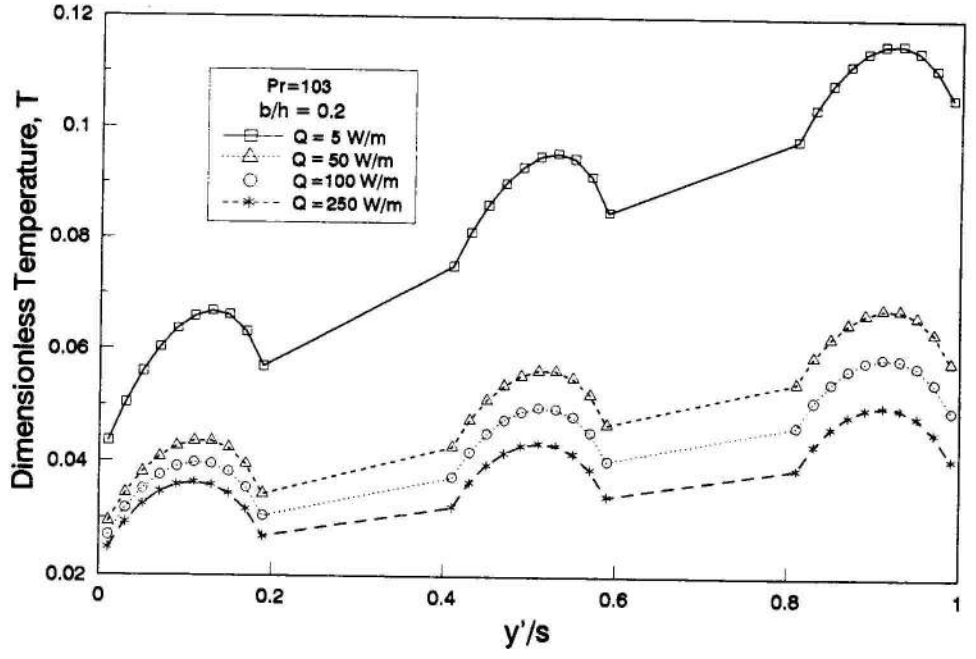

Figure 6.5 T versus y'/s for various Q, (b/h) = 0.2 for ethylene glycol.

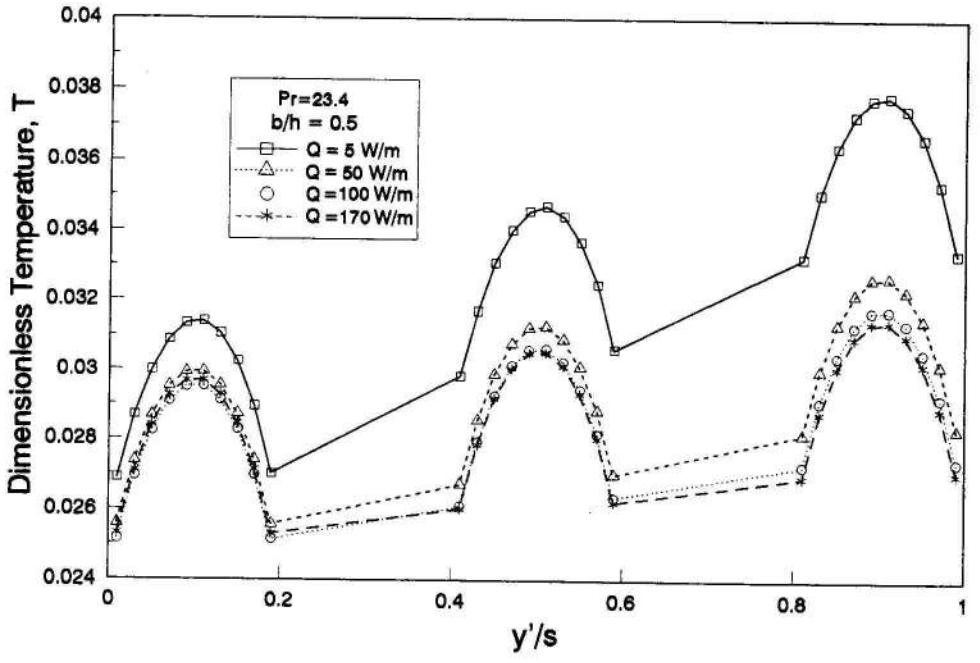

Figure 6.6 T versus y'/s for various Q, (b/h) = 0.5 for FC-75.

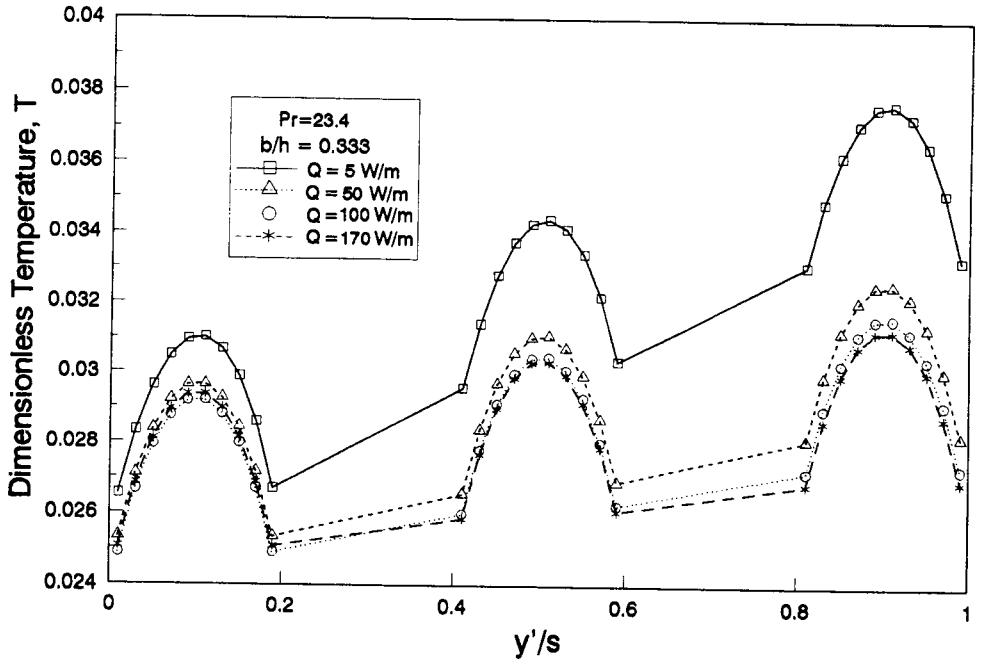

Figure 6.7 T versus y'/s for various Q, (b/h) = 0.333 for FC-75.

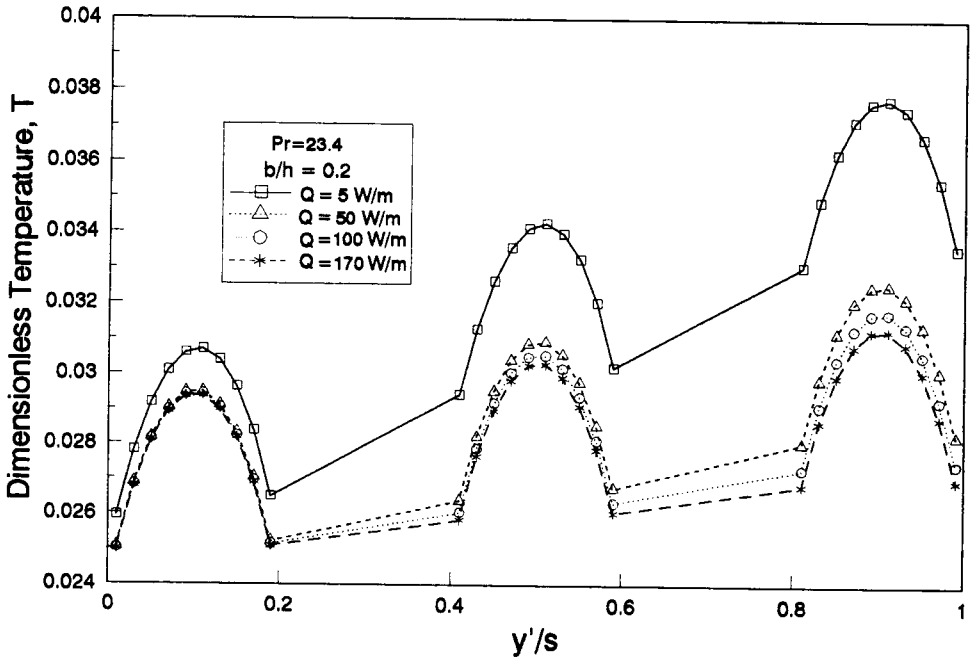

Figure 6.8 T versus y'/s for various Q, (b/h) = 0.2 for FC-75.

the ratio between the vertical direction from the starting point of the first protruding element and the distance from the first protruding element to the last protruding element, are shown. Dimensionless temperatures are as defined in equation (3-10).

For given heat inputs, upper heated surface center temperatures were usually higher than those for the lower protruding surfaces. That is, the higher upper block surface temperatures were caused by a preheating effect from rising warm buoyancy flows. For reason of its unique definition, the dimensionless temperature, T, decreased as the values of the module heat sources were increased.

For each protruding block, there were a minimum of 10 data points spaced at equal intervals. For given heat sources, Q, temperatures at each block surface generally increased from the 1st to the 7th data points and, in the cases of either water or ethylene glycol as the cooling fluid, decreased from the 8th to the 10th data points. For reason of the conduction heat transfer effect from the uniform heat source in the heated element and the convection heat transfer effect from the rising warm buoyancy flows, the locations of the highest temperatures for each protruding element surface were generally somewhat above the middle of the surface. The highest temperature at the third heated block surface was also higher than the temperatures for either the first or second surface.

6.1.2 Comparison of Protruding Heated Element Surface Temperatures for Cooling Liquids at Identical Heat Inputs

Comparisons of the temperature increments for identical channel to height ratios for the different cooling liquids, subject to equally powered devices, are given in Figures 6.9 to 6.12. Though the identical heat power, Q, for each protruding device was generated for identical boundary conditions, the temperature increments for the protruding element surfaces at steady-state were dependent upon which liquid was used as the coolant. Dimensional temperature increases from the initial temperature at each protruding surface are shown for the different coolants.

In Figures 6.9 and 6.11, temperature increases for the protruding surfaces for different coolants, at an equal power of 100 W/m for protruding electrical components with different channel spacing to height ratios are shown. When the temperature curves are compared, differences in the cooling capacities of the liquids considered become apparent. From Figure 6.9, for water at the heating power of 100 W/m, the increase in temperature was only from 4°C to 6°C. However, comparable increases for ethylene glycol and FC-75 were, respectively, from 12°C to 22°C and from 39°C to 49°C. Thus, for a given heat source,

$$(T^* - T_c)_{FC-75} > (T^* - T_c)_{e.g.} > (T^* - T_c)_{water} .$$

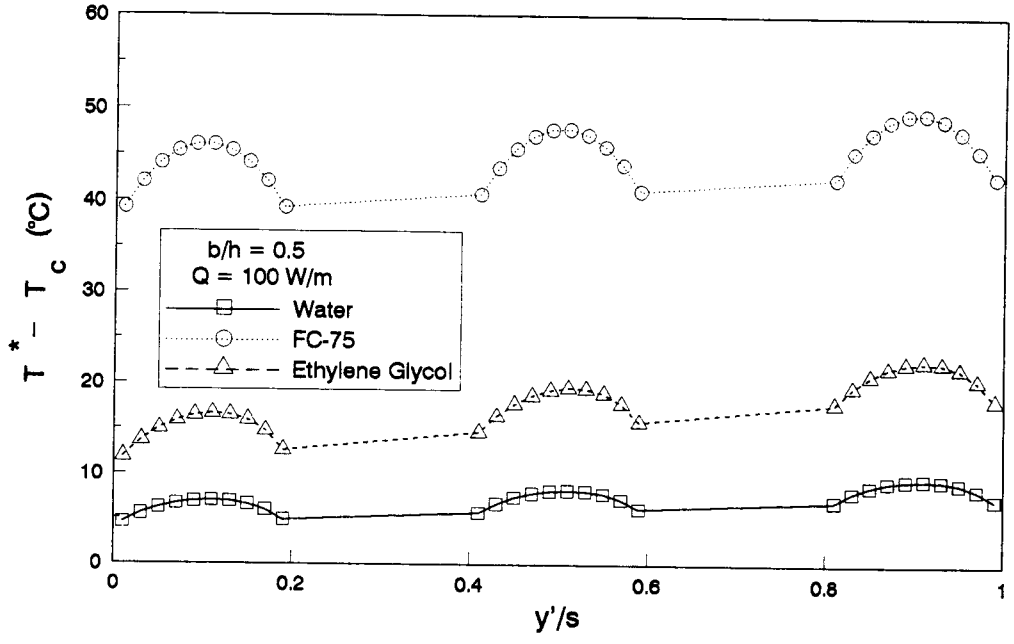

Figure 6.9 Protruding surface temperature increases for cooling liquids, Q = 100 W/m, (b/h) = 0.5.

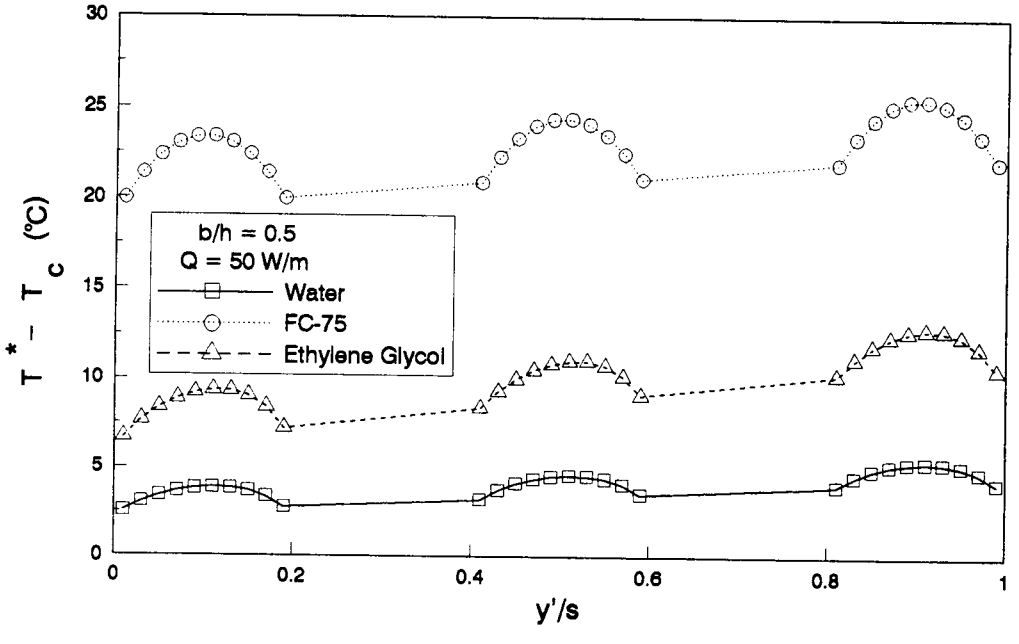

Figure 6.10 Protruding surface temperature increases for cooling liquids, Q = 50 W/m, (b/h) = 0.5.

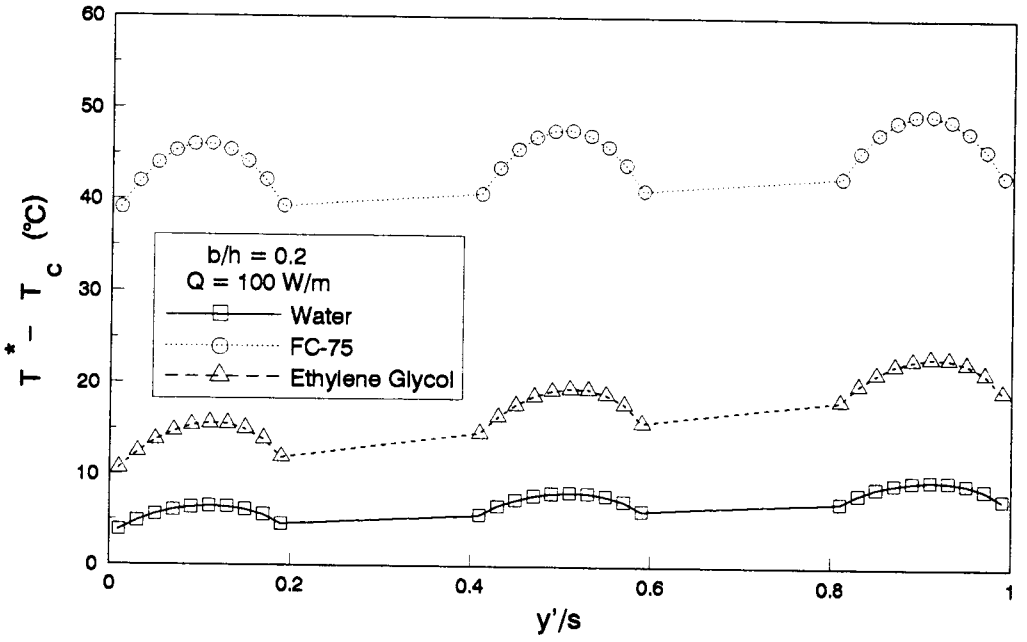

Figure 6.11 Protruding surface temperature increases for cooling liquids, Q = 100 W/m, (b/h) = 0.2.

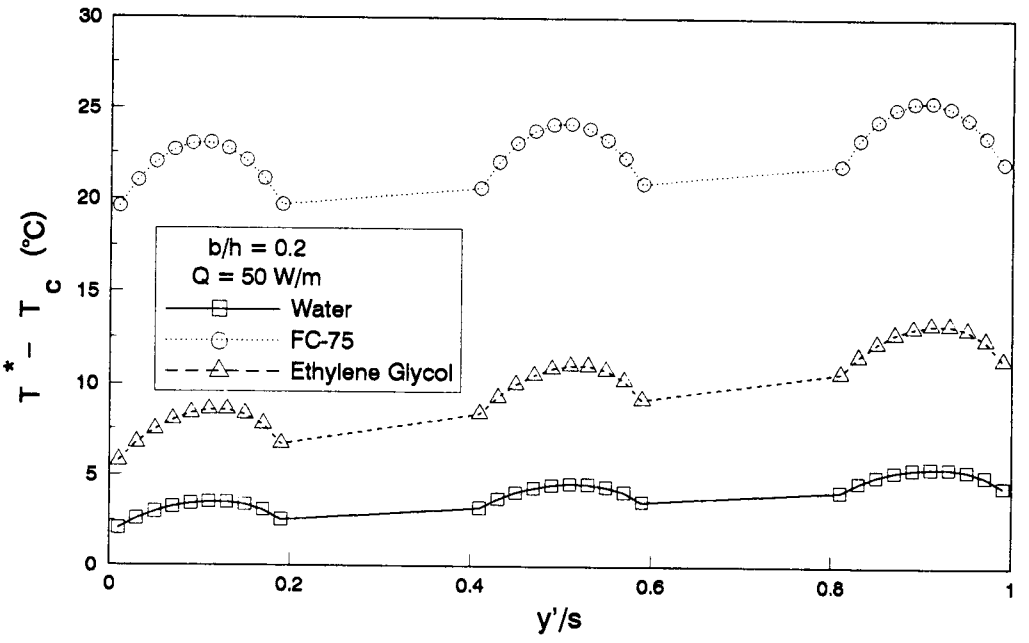

Figure 6.12 Protruding surface temperature increases for cooling liquids, Q = 50 W/m, (b/h) = 0.2.

Therefore, among the liquids considered, water is the best coolant with respect to temperature increase at the heated surface.

To determine how fluid properties affect the relationship between Q and temperature increase, the cooling fluid properties for the three liquids are analyzed to generate basic information on the significance of the cooling effect. Thus, from Table 5.1, the thermal physical properties of each of the liquids express the following relationships:

$$k_{water} > k_{e.g.} > k_{FC-75} ,$$

$$Cp_{water} > Cp_{e.g.} > Cp_{FC-75} ,$$

$$\beta_{water} < \beta_{e.g.} < \beta_{FC-75} ,$$

$$\alpha_{water} > \alpha_{e.g.} > \alpha_{FC-75} ,$$

$$Pr_{water} < Pr_{FC-75} < Pr_{e.g.} ,$$

and

$$\rho_{water} < \rho_{e.g.} < \rho_{FC-75} .$$

Examination of these cooling liquid properties indicates that liquid conductivity, specific heat, and the thermal expansion coefficients influence temperature increase. Thus, it was determined that the temperature increase for a protruding heated surface was smaller for the coolant with the highest thermal conductivity for given conditions of heat input. This finding is in good agree-

ment with the experimental results obtained by Lin [39]. For the numerical data considered for given conditions of heat input, higher protruding heated surface temperatures were observed for FC-75.

6.2 Streamlines, Channel Velocity Profiles, and Isothermal Lines

6.2.1 Streamlines

The flow patterns of different channel spacing to height ratios for the three liquids under consideration are given in Figures 6.13 to 6.27. The dimensionless stream-function (Eqn. 4-54) derived from numerical simulation was used to plot the streamlines. Previously, Lin [39] examined flow motion by experimental flow visualization to determine typical flow patterns in vertical channels subject to protruding discrete heating sources. From the present study, the channel flow patterns from the numerical simulation were well matched to Lin's results.

With respect to the distinct channel flow regions, reverse flow from the circulation effect near the top surface of the enclosure was found in the top portions of the channel when the spacing was relatively large. The penetration depth of these reversed flows were closely related to both channel spacing and liquid coolant properties. The relatively high velocity flow gathered at the front of the heated element rose along the heated plate with protruding

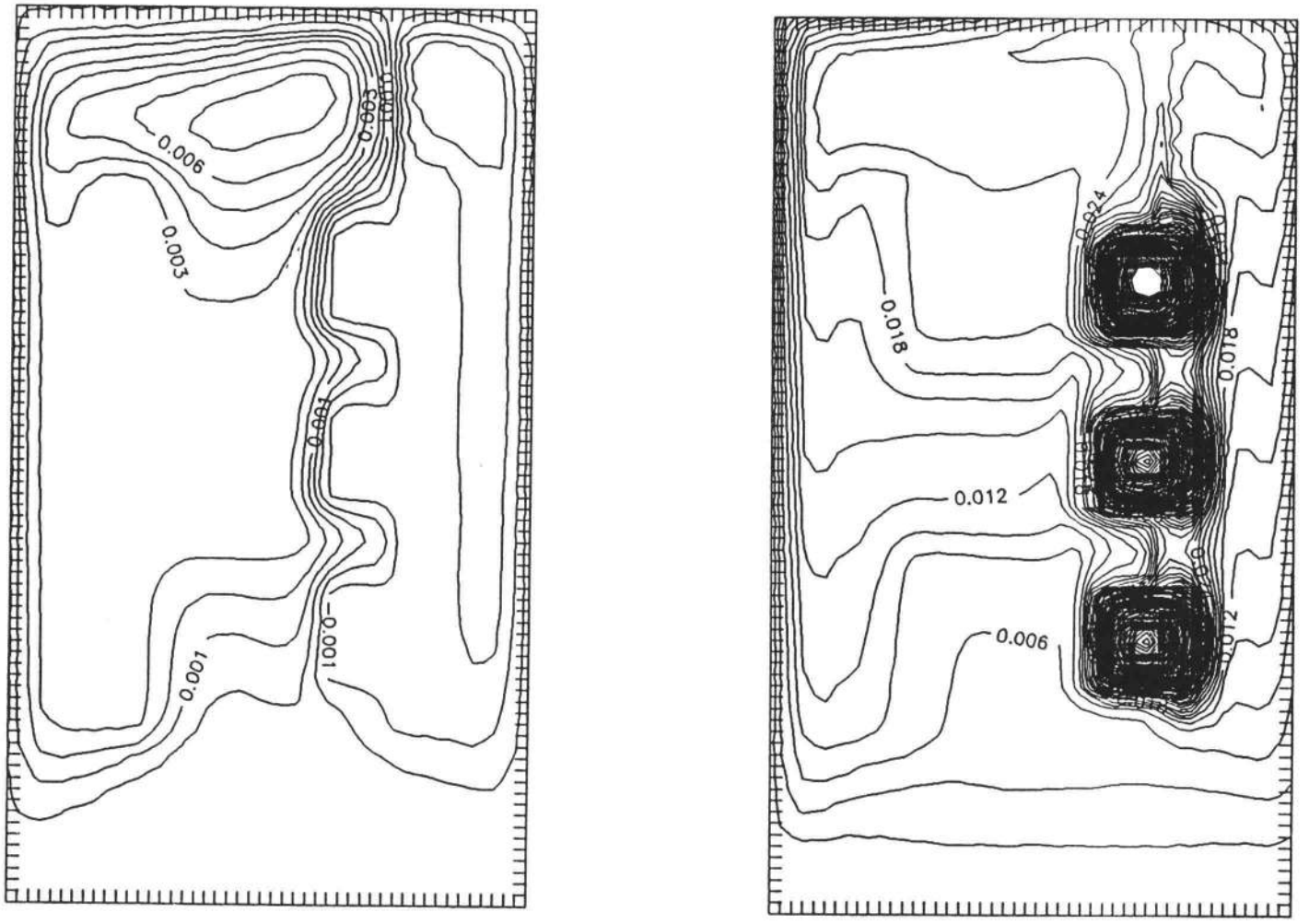

Figure 6.13 Streamline and isotherm patterns for Pr = 5.9, $Ra_b = 1.0 \times 10^8$, $(b/h) = 0.5$, and $R_1 = 1.03$.

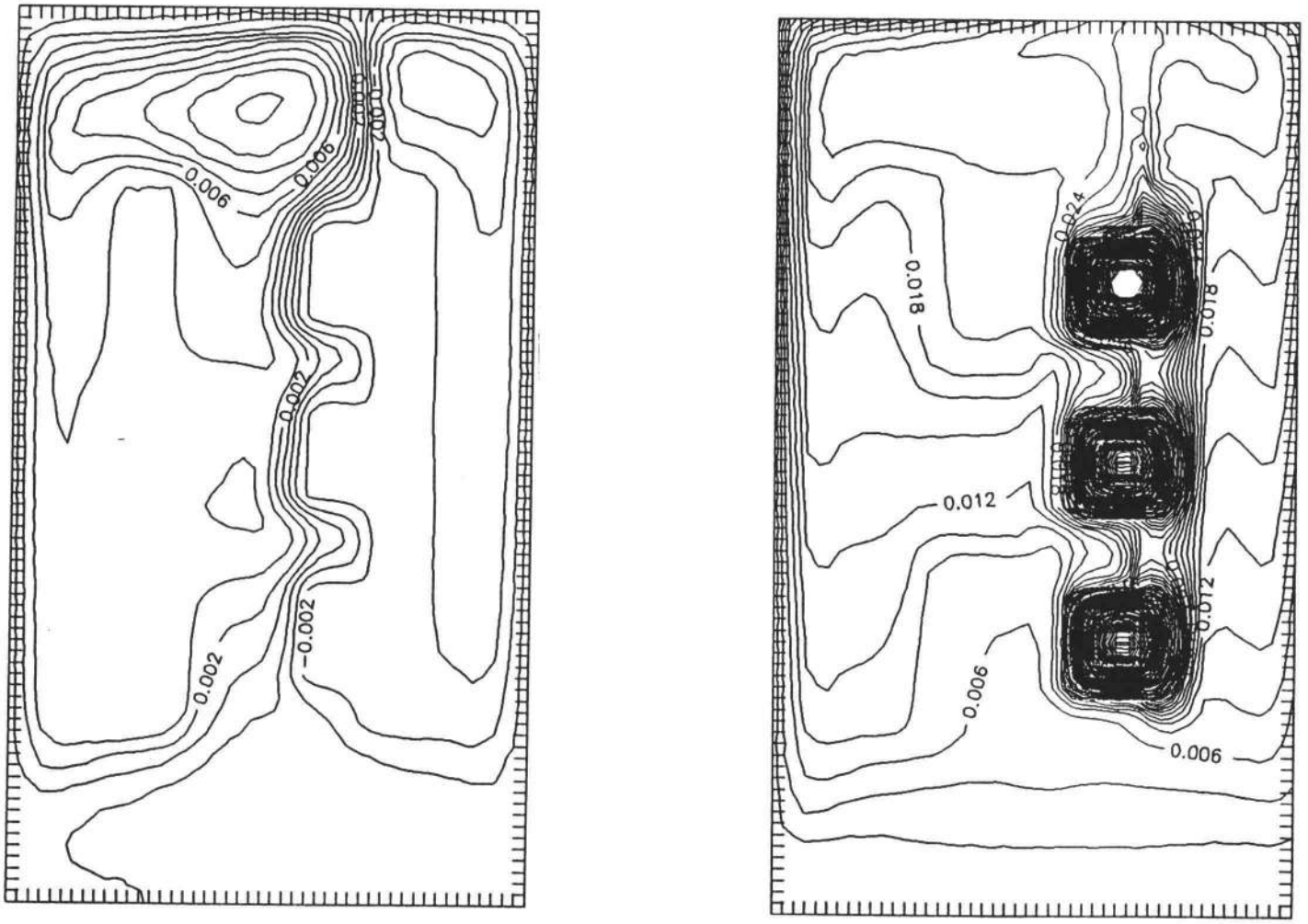

Figure 6.14 Streamline and isotherm patterns for Pr = 5.9, $Ra_b = 0.5 \times 10^8$, $(b/h) = 0.4$, and $R_1 = 1.03$.

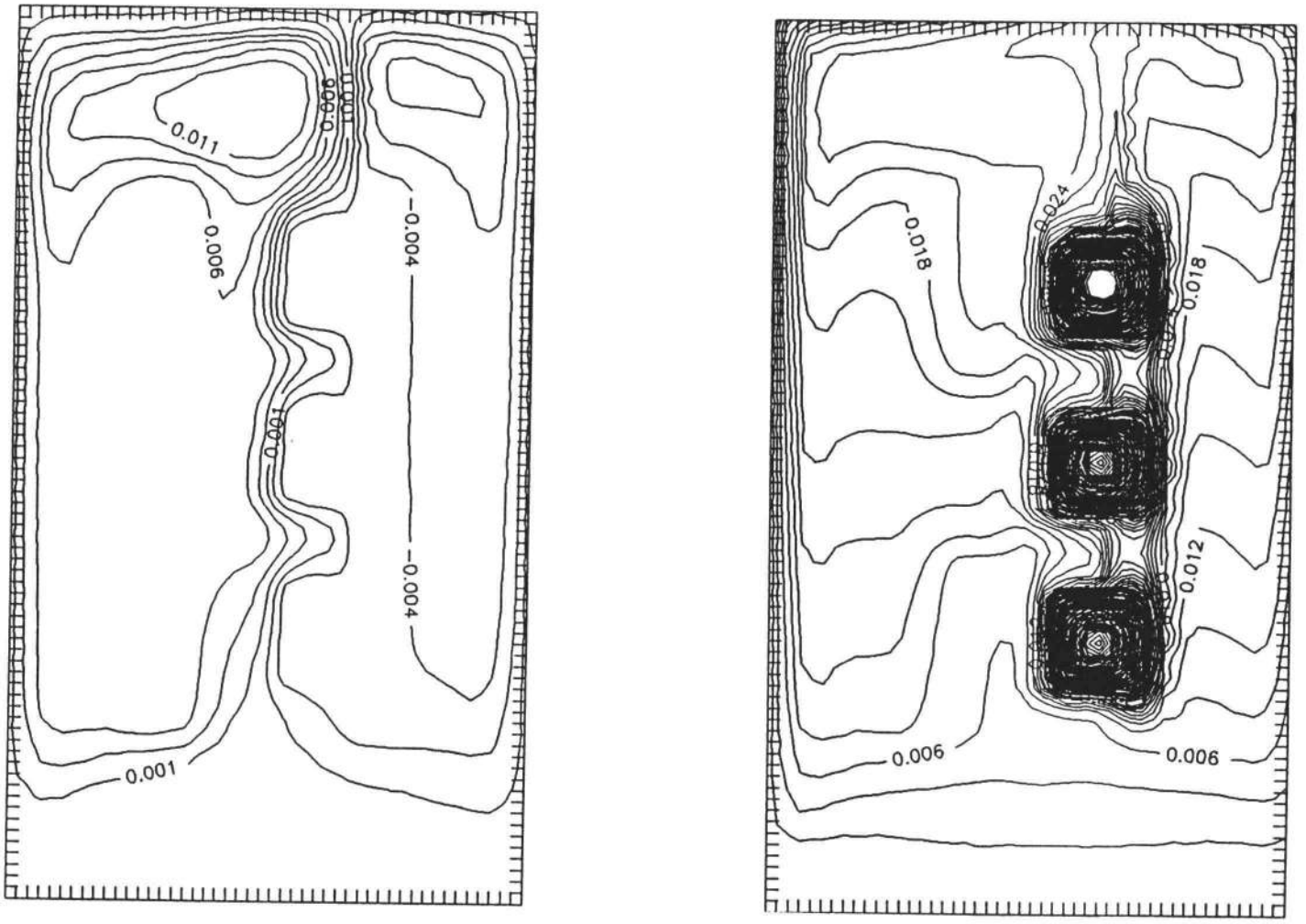

Figure 6.15 Streamline and isotherm patterns for Pr = 5.9, $Ra_b = 0.3 \times 10^8$, $(b/h) = 0.333$, and $R_1 = 1.03$.

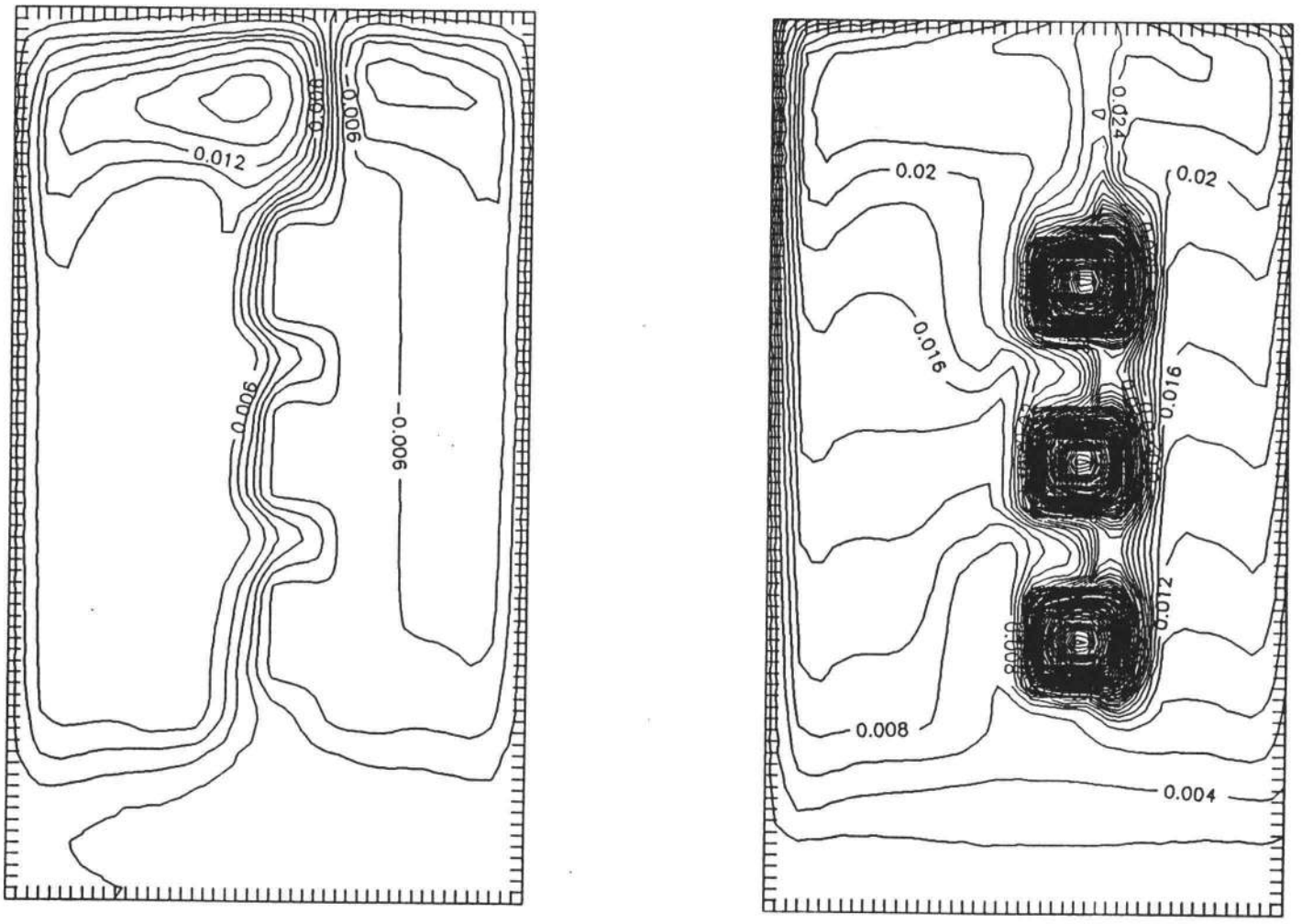

Figure 6.16 Streamline and isotherm patterns for Pr = 5.9, $Ra_b = 0.1 \times 10^8$, $(b/h) = 0.267$, and $R_1 = 1.03$.

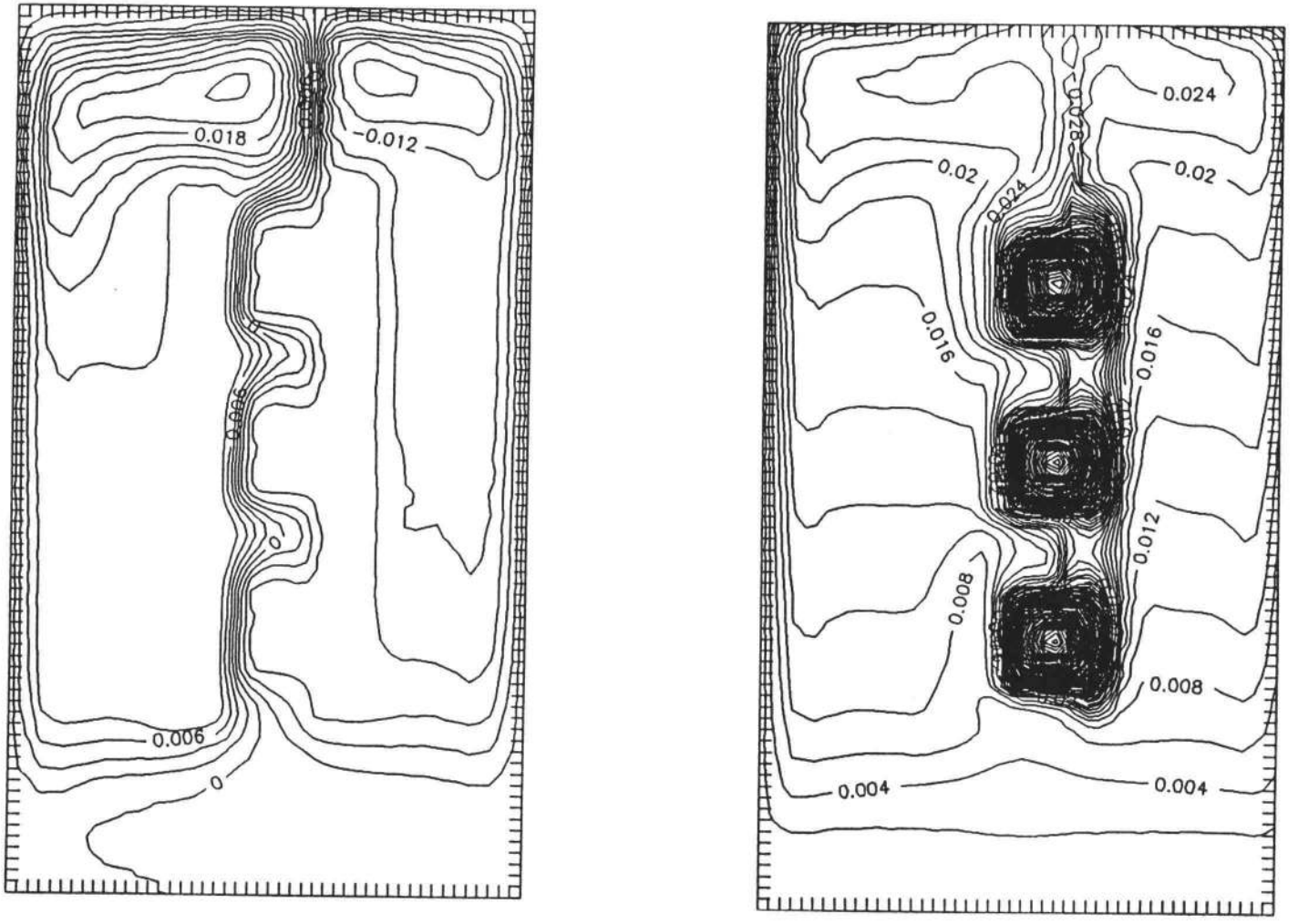

Figure 6.17 Streamline and isotherm patterns for Pr = 5.9, $Ra_b = 0.6 \times 10^7$, $(b/h) = 0.2$, and $R_1 = 1.03$.

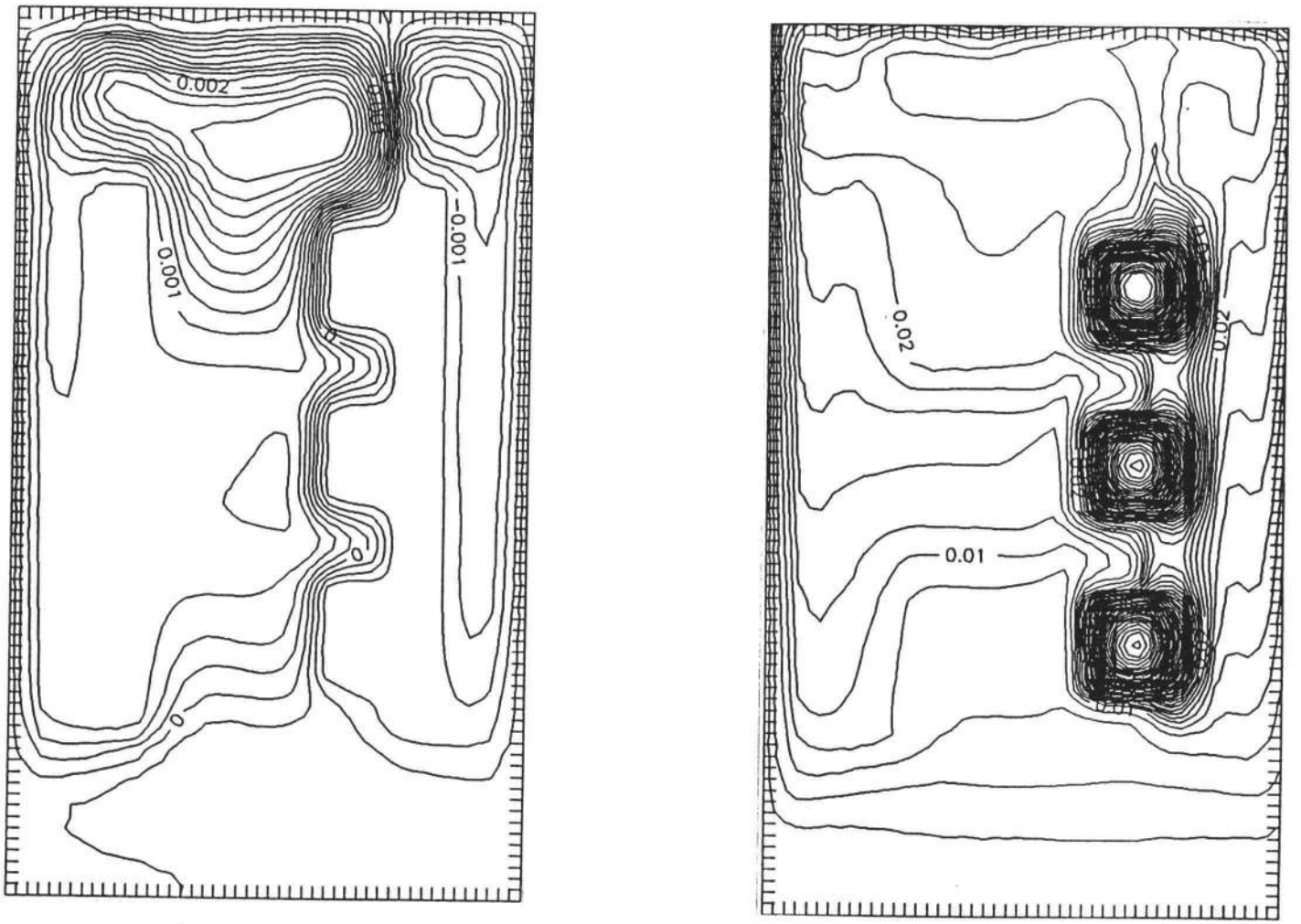

Figure 6.18 Streamline and isotherm patterns for Pr = 103, $Ra_b = 0.7 \times 10^8$, $(b/h) = 0.5$, and $R_1 = 2.46$.

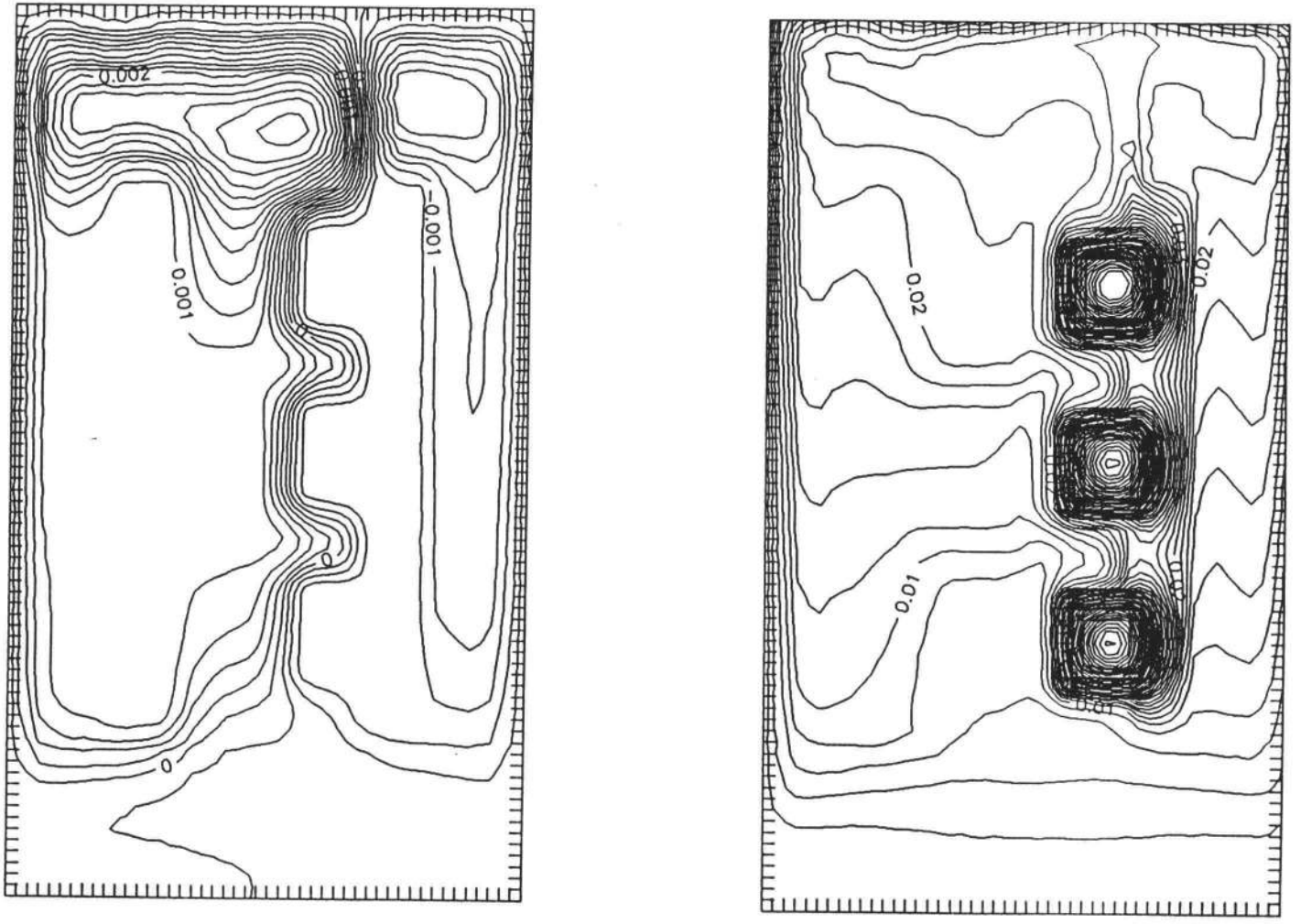

Figure 6.19 Streamline and isotherm patterns for Pr = 103, $Ra_b = 0.4 \times 10^8$, $(b/h) = 0.4$, and $R_1 = 2.46$.

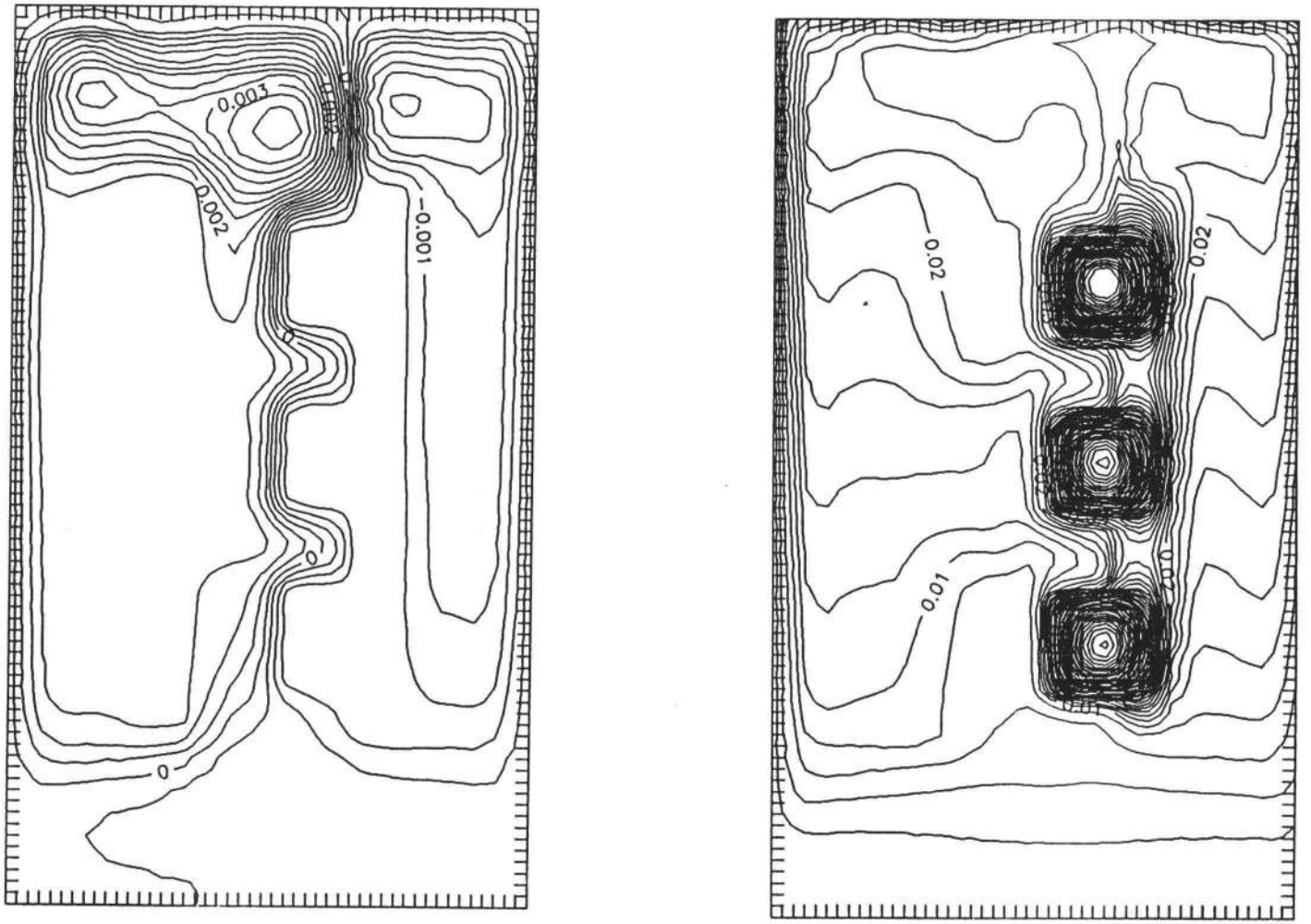

Figure 6.20 Streamline and isotherm patterns for Pr = 103, $Ra_b = 0.2 \times 10^8$, $(b/h) = 0.333$, and $R_1 = 2.46$.

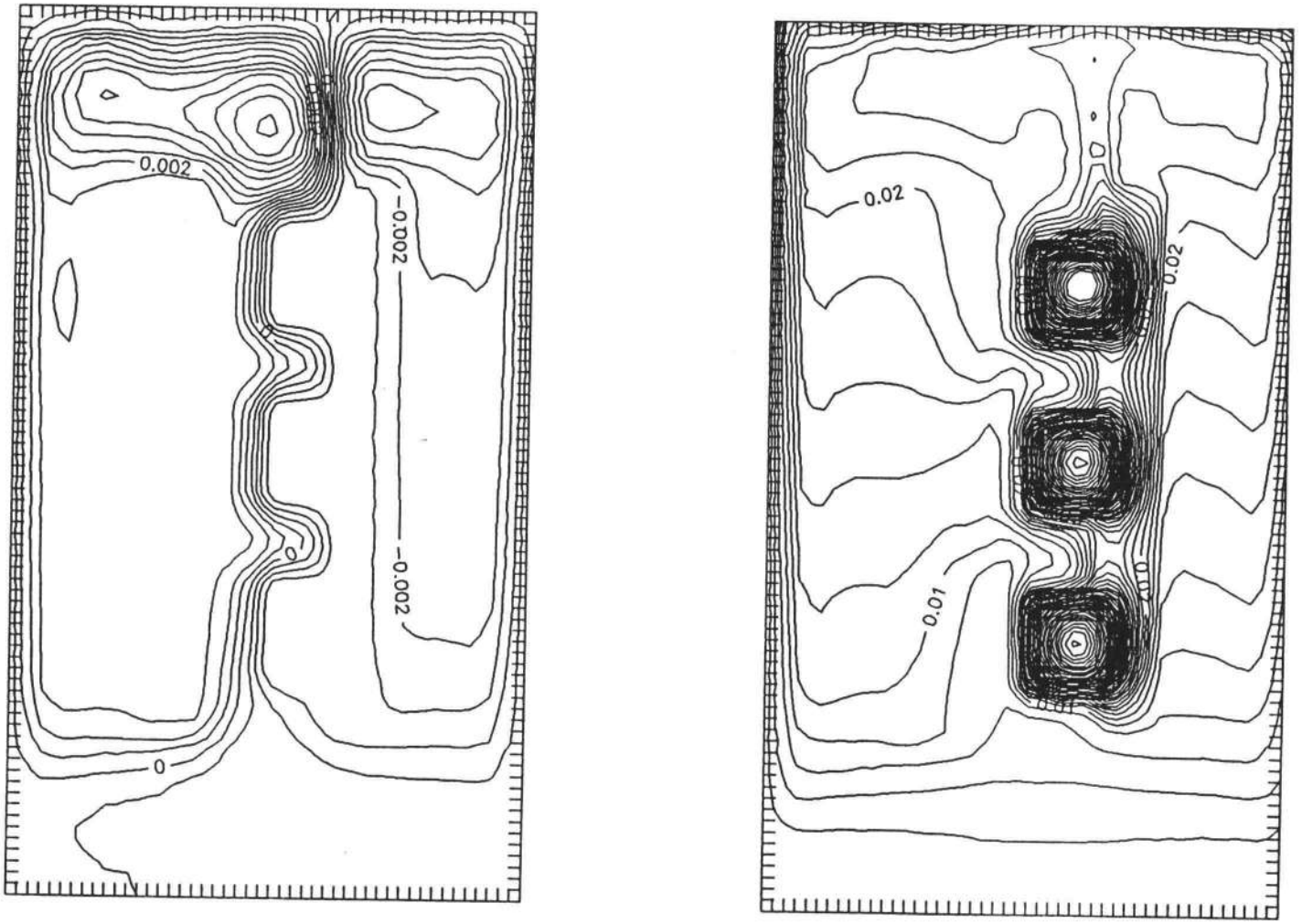

Figure 6.21 Streamline and isotherm patterns for Pr = 103, $Ra_b = 0.1 \times 10^8$, $(b/h) = 0.267$, and $R_1 = 2.46$.

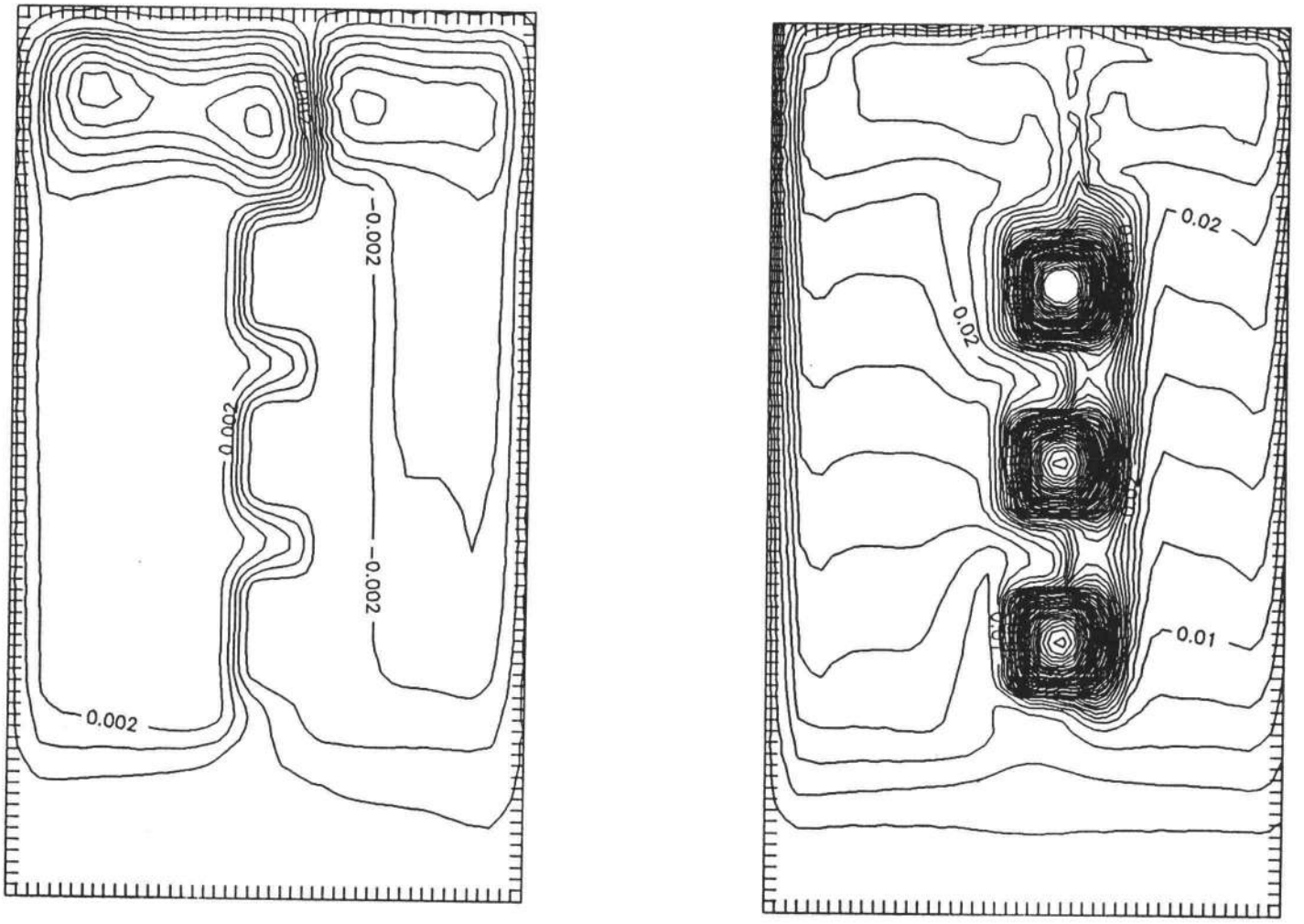

Figure 6.22 Streamline and isotherm patterns for Pr = 103, $Ra_b = 0.5 \times 10^7$, $(b/h) = 0.2$, and $R_1 = 2.46$.

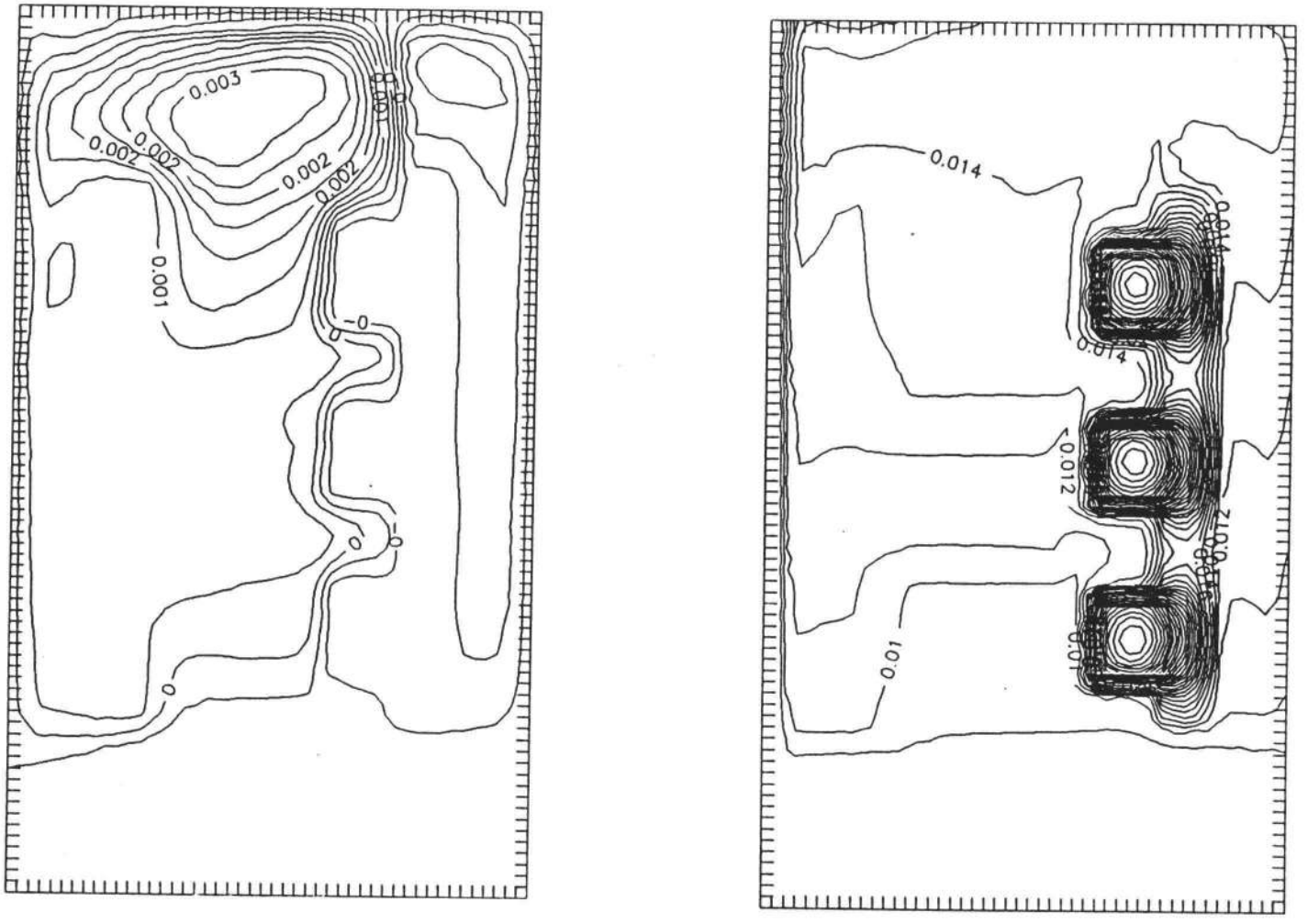

Figure 6.23 Streamline and isotherm patterns for Pr = 23.4, $Ra_b = 0.4 \times 10^{10}$, $(b/h) = 0.5$, and $R_1 = 9.81$.

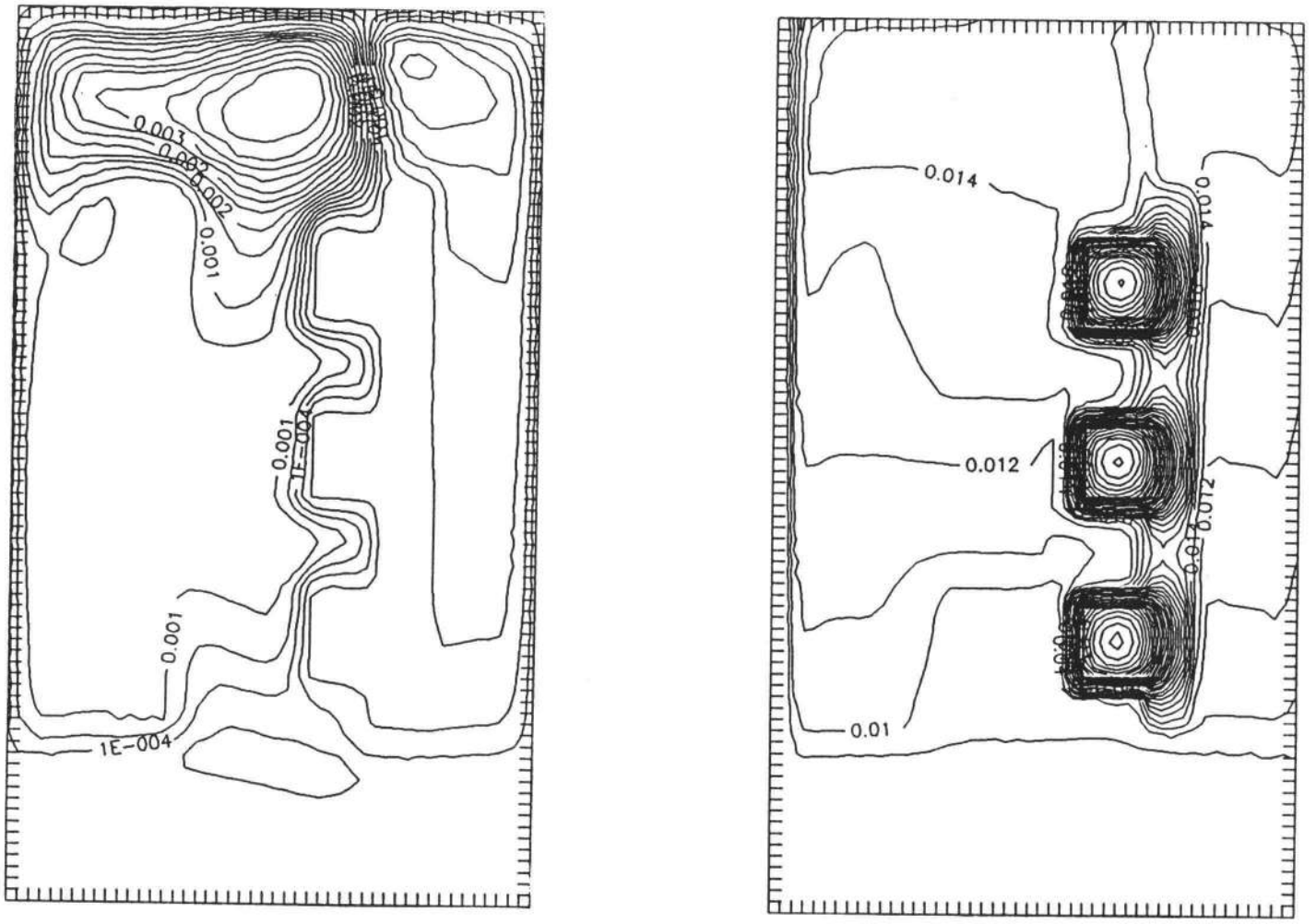

Figure 6.24 Streamline and isotherm patterns for Pr = 23.4, $Ra_b = 0.2 \times 10^{10}$, $(b/h) = 0.4$, and $R_1 = 9.81$.

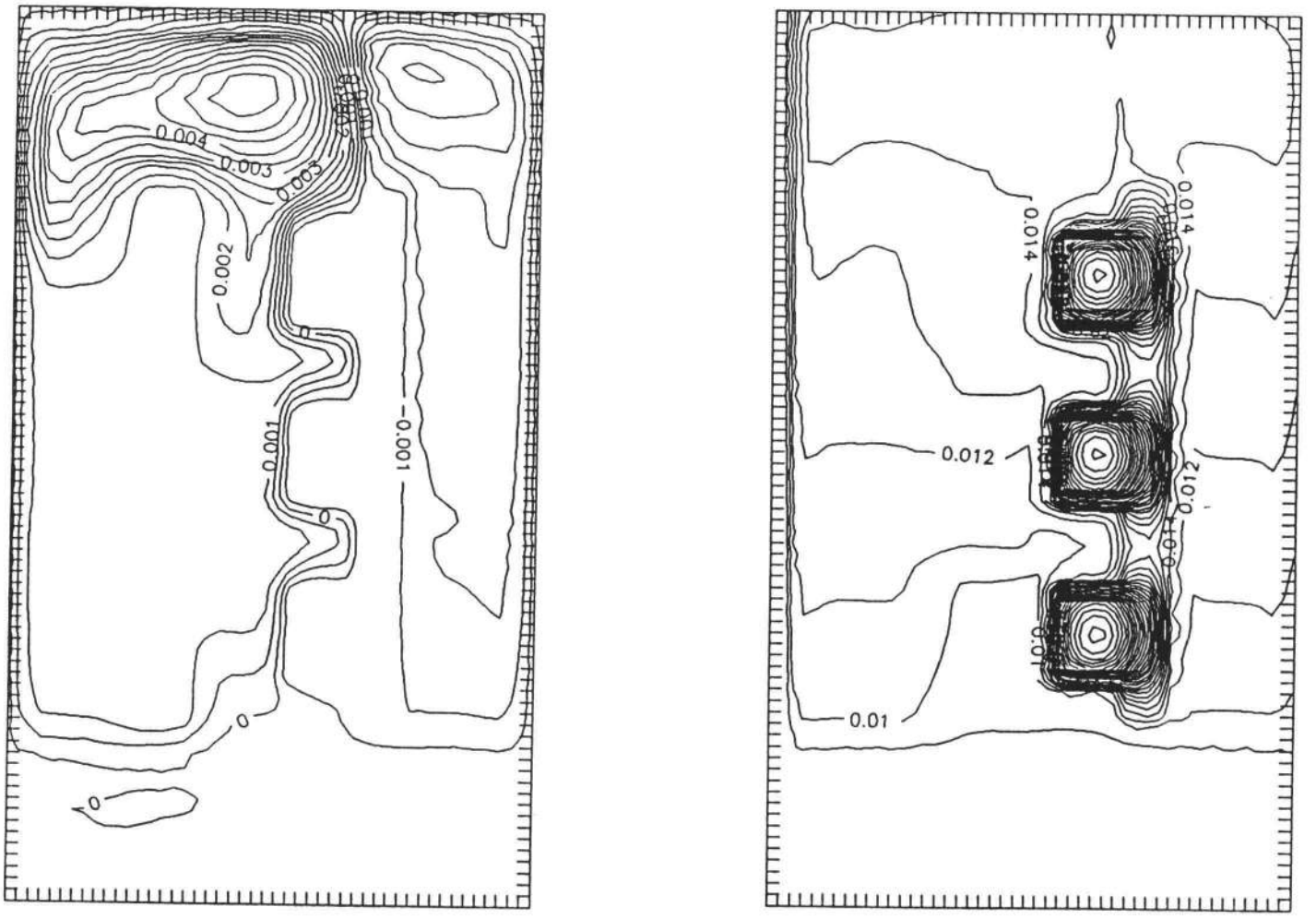

Figure 6.25 Streamline and isotherm patterns for Pr = 23.4, $Ra_b = 0.1 \times 10^{10}$, $(b/h) = 0.333$, and $R_1 = 9.81$.

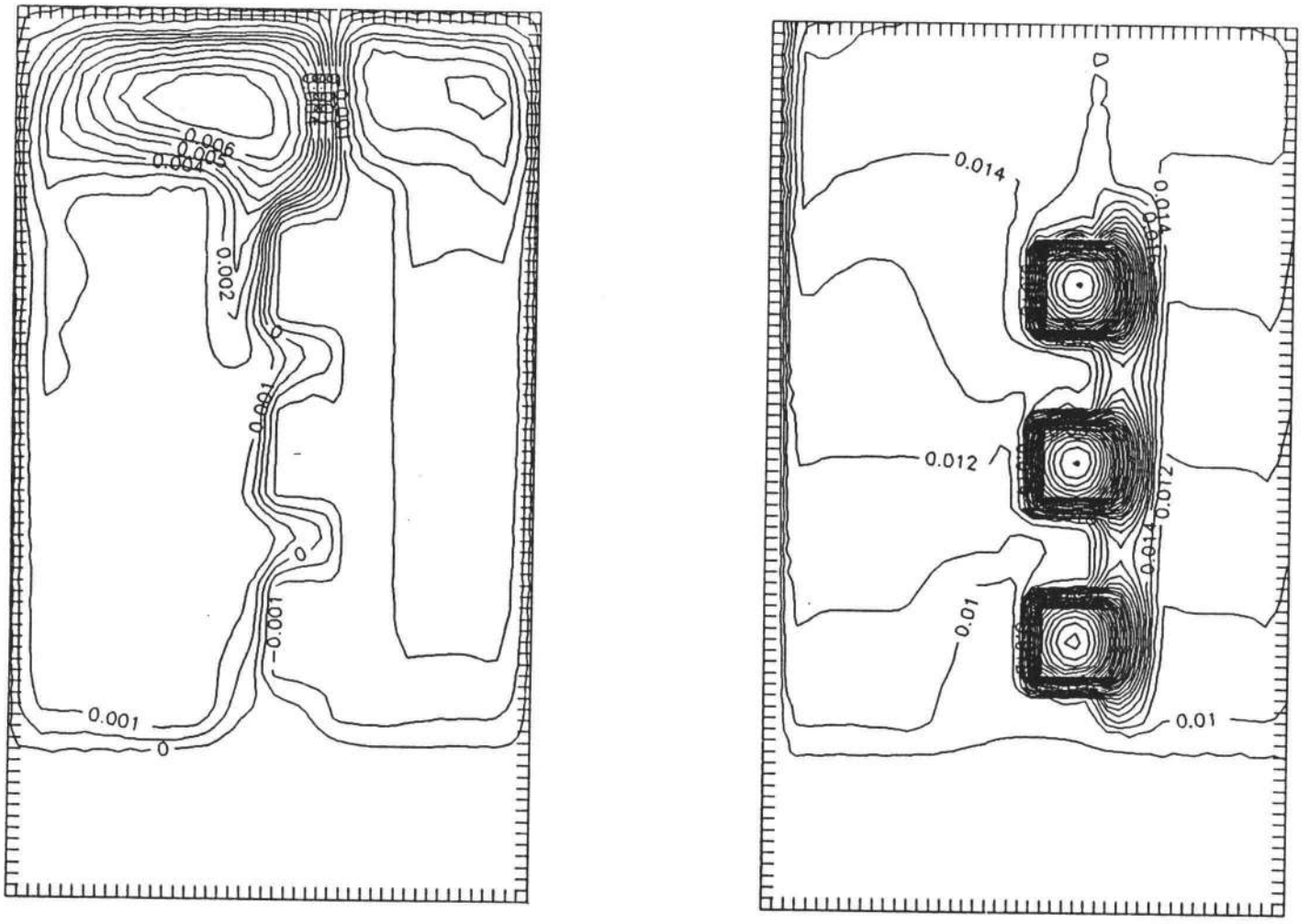

Figure 6.26 Streamline and isotherm patterns for Pr = 23.4, $Ra_b = 0.7 \times 10^9$, $(b/h) = 0.267$, and $R_1 = 9.81$.

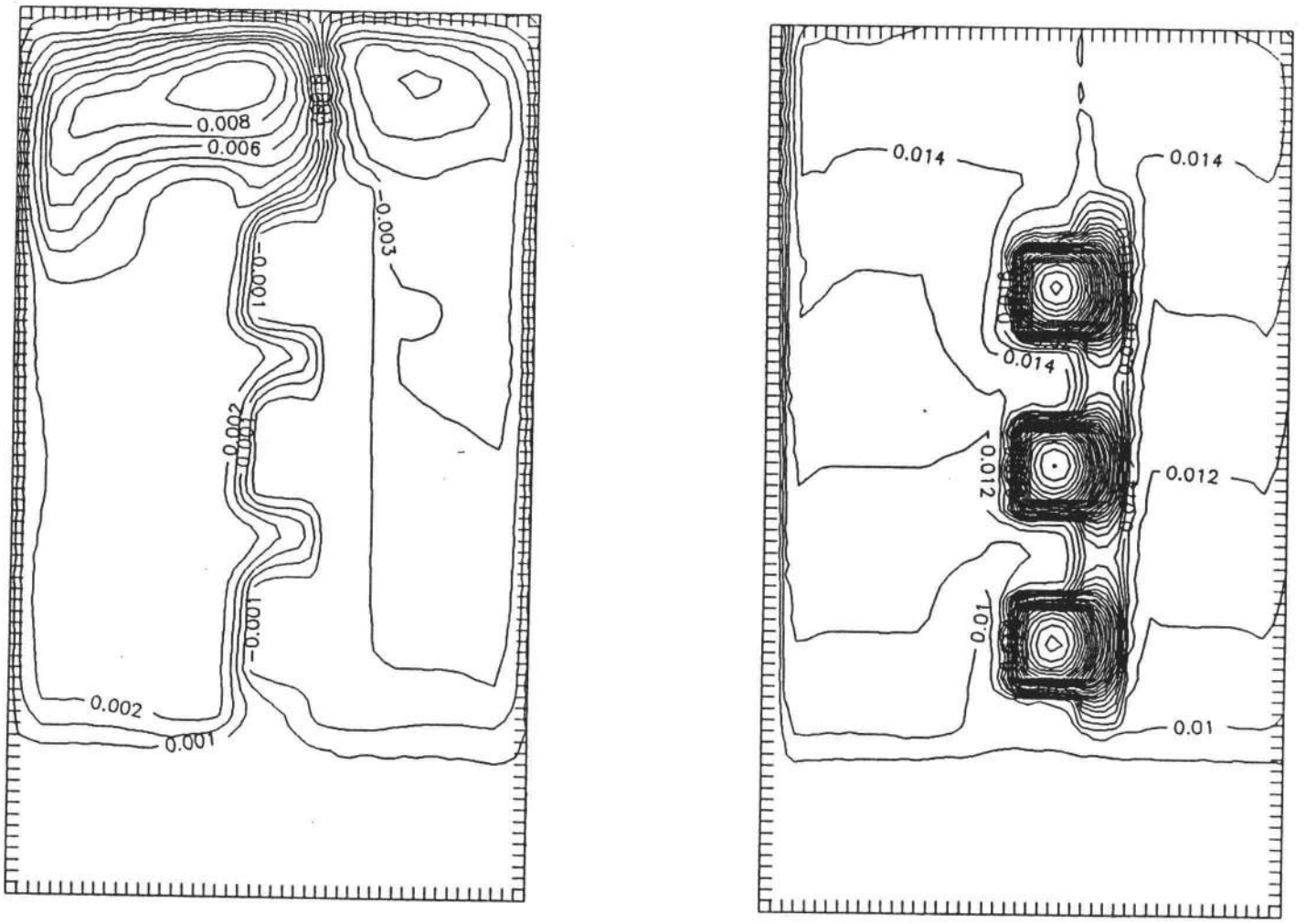

Figure 6.27 Streamline and isotherm patterns for Pr = 23.4, $Ra_b = 0.3 \times 10^9$, $(b/h) = 0.2$, and $R_1 = 9.81$.

elements. In contrast, weak flow regions were located adjacent to unheated shrouding plate in the middle portion of the widely spaced channel. These regions decreased as the channel spacing to height ratio was decreased from 0.5 to 0.2.

Flow circulation occurred at the top of the enclosure since the heated flow encountered the cooler top surface. In the lower portions of the channel, buoyancy flows were relatively slow. As the flow advanced along the heated surfaces, it was accelerated downstream. These streamlines are described in Figures 6.13 to 6.17 for the water coolant in terms of changes in channel spacing and Rayleigh number. The same parameters are indicated for ethylene glycol and for FC-75 in, respectively, Figures 6.18 to 6.22 and 6.23 to 6.27. In the case of ethylene glycol, as the channel spacing was reduced, two split circulation flow patterns were evidenced at the upper right side of the heated plates.

6.2.2 Channel Velocity Profiles

Plotting velocities within the channels provided supplementary information on flow patterns. This was particularly useful around the heated elements. Dimensionless velocity profiles for three channel locations are shown in Figures 6.28 to 6.32 for vertical velocities in the channel at the midheight level of the first through the third protruding surface, respectively, $y'/s = 0.1$, $y'/s = 0.5$,

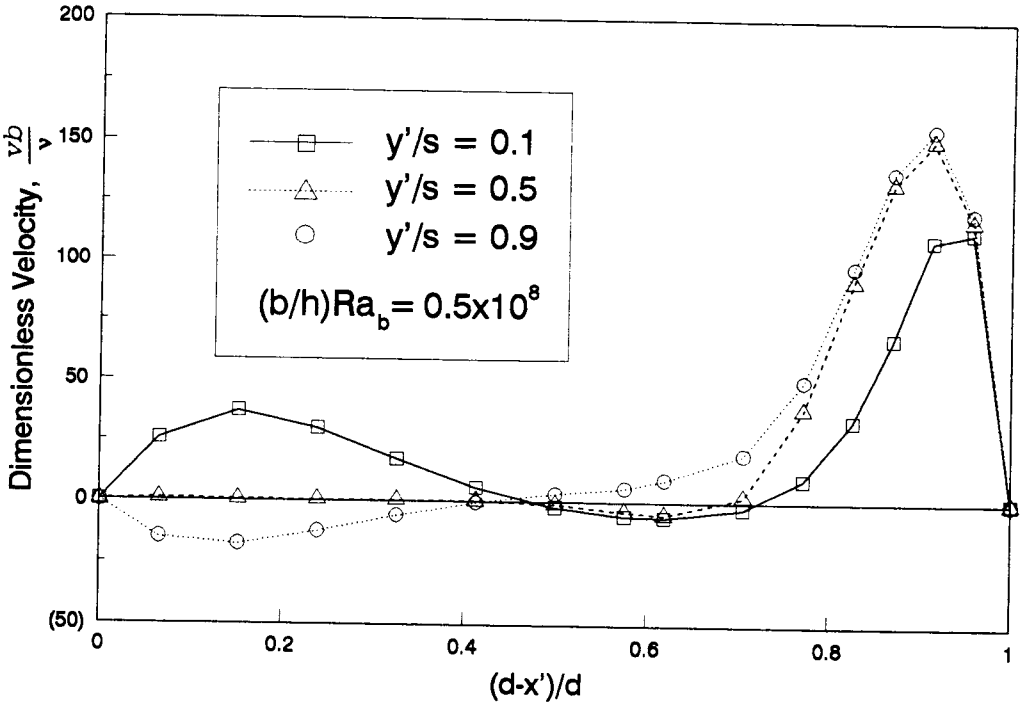

Figure 6.28 Dimensionless velocity profiles within the channel for (b/h) = 0.5 and Pr = 5.9.

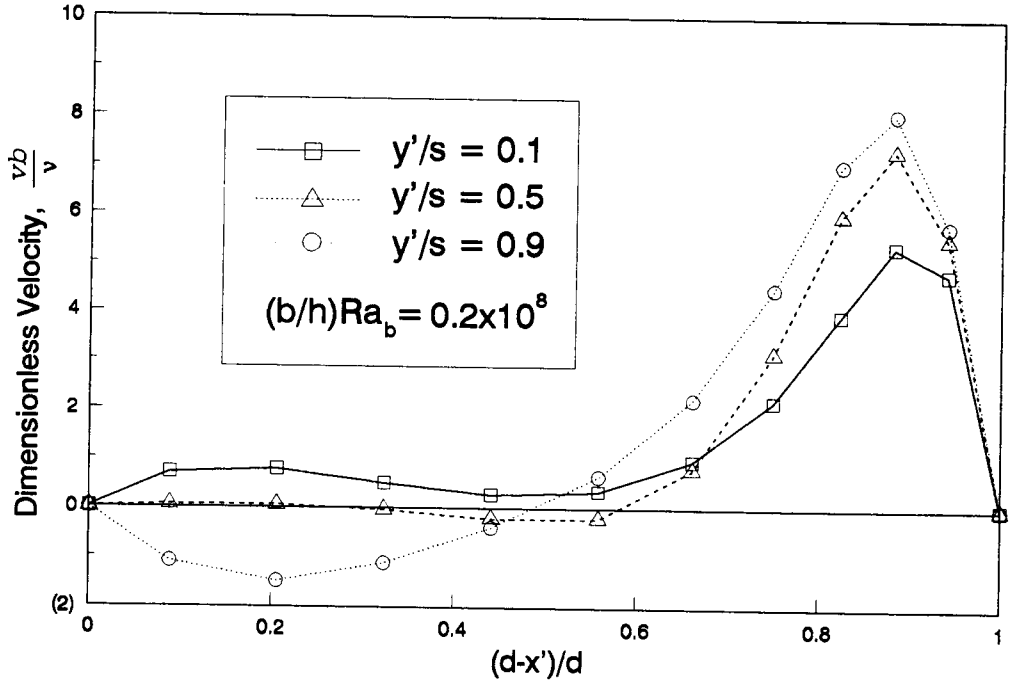

Figure 6.29 Dimensionless velocity profiles within the channel for (b/h) = 0.4 and Pr = 103.

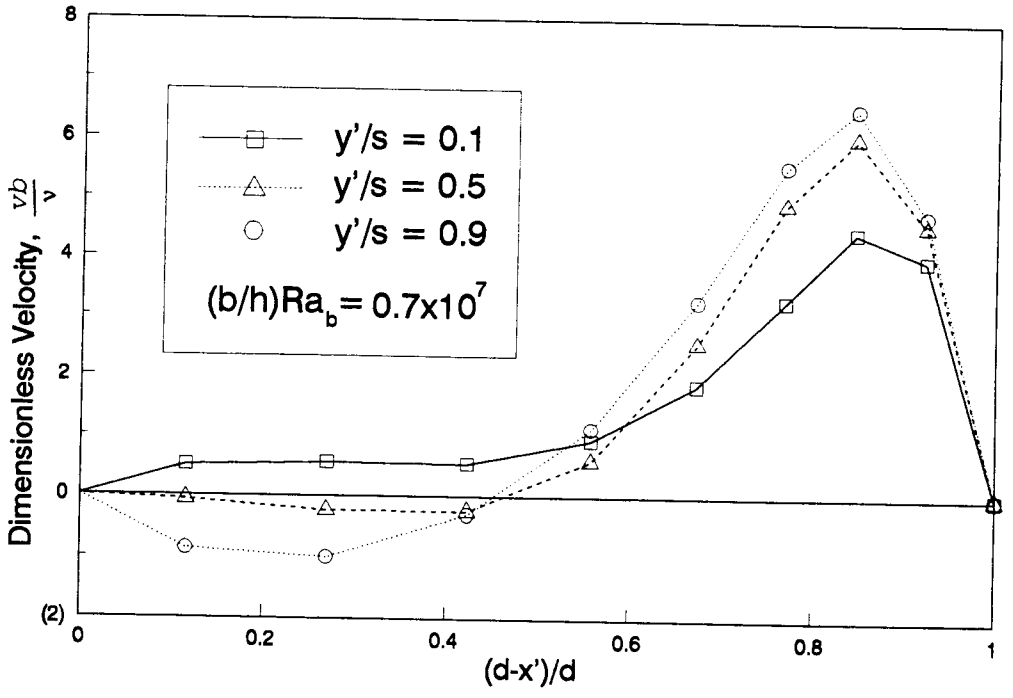

Figure 6.30 Dimensionless velocity profiles within the channel for (b/h) = 0.333 and Pr = 103.

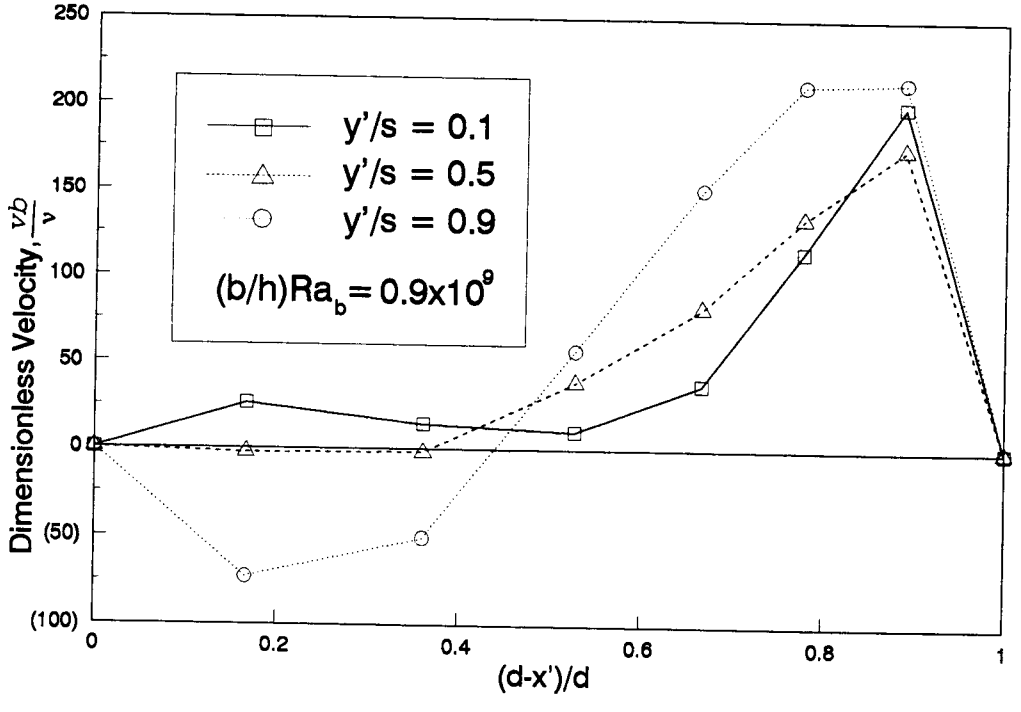

Figure 6.31 Dimensionless velocity profiles within the channel for (b/h) = 0.267 and Pr = 23.4.

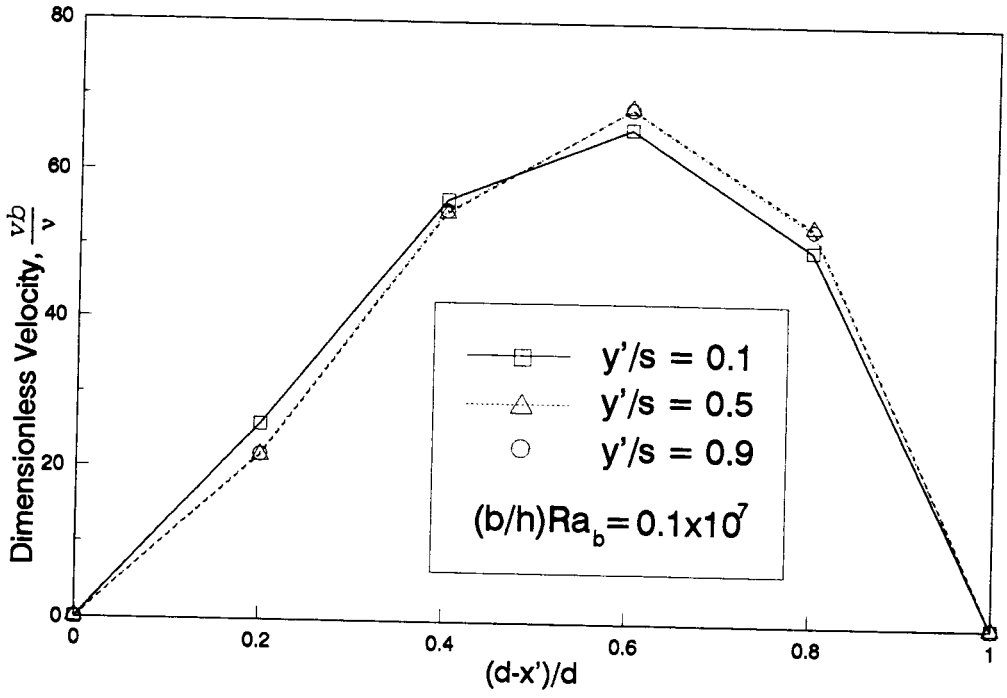

Figure 6.32 Dimensionless velocity profiles within the channel for (b/h) = 0.2 and Pr = 5.9.

and y'/s = 0.9 . In these figures, five channel aspect ratios for various cooling fluids are presented.

Figure 6.28 shows boundary-layer velocity profiles along the heated side of the protruding surfaces, profiles which were more vigorous than velocities adjacent to the unheated shrouded plate. The profiles for locations adjacent to the second and third heated protruding surfaces reflected higher velocities than the profile for the first heated protruding surface. Negative velocities near the unheated plate around the channel exits reflected a circulation effect, which existed in the top portions of the model.

The velocity profiles at channel midheight level near the unheated plate described relatively weak flows. Though different coolants were considered, this trend remained largely constant from Figures 6.28 through 6.31. From Figure 6.32, the smallest channel spacing indicated a parabolic profile. At the top portion of the model, due to narrow channel spacing, there was no circulation effect upon the channel. In addition, since the velocity profile at channel midheight and that for the third protruding surface were nearly identical, fully developed flow characteristics were found.

6.2.3 Isothermal Lines

The temperature fields for different channel spacing to height ratios for the three cooling liquids are also described in Figures 6.13 to 6.27. The dimensionless temperature, T, is used to plot the isothermal lines. Isothermal lines for various channel spacings and Rayleigh numbers for water as a coolant are shown in Figures 6.13 to 6.17, whereas the isothermal lines for ethylene glycol and FC-75 are provided, respectively, in Figures 6.18 to 6.22 and 6.23 to 6.27.

Though the left plate of the test model lacked a heat source, the existence of a shrouding plate affected the temperature field. Based upon the location of this unheated plate, the isothermal lines within the channel demonstrate differences between configurations. At steady-

state, the fluid temperatures of the upper region of the model were higher than the fluid temperatures of the lower region. The cooled liquid temperature at the middle of the channel entry affected by the cold enclosure was lower than the temperature of the unheated plate at the same level. In contrast, the temperature of the flow past the second protruding heated device within the channel was higher than the temperature of the unheated plate at the same level. When the channel spacing to height ratio was set at 0.5, as shown in Figures 6.13, 6.18, and 6.23, constant temperature lines for the same altitudes at channel midlevel were observed. As the ratio was decreased, the width of the flat lines was decreased.

6.3 Cooling Capacities of Different Cooling Liquids

The heat source, Q, for each protruding heated device, plotted as a function of the temperature difference, $\Delta T\,(^{\circ}C)$,between the highest temperature of each protruding heated surface and the cold enclosure temperature for the various liquids, is shown in Figures 6.33 to 6.35. Figure 6.33 represents the third protruding heated device from the bottom, whereas Figure 6.34 represents the first protruding heated device. For water and FC-75 as coolants, ΔT increased proportionate to the temperature increase of the heat source. For given heat inputs, the ΔT for FC-75 was much higher than the equivalent measure for water. For

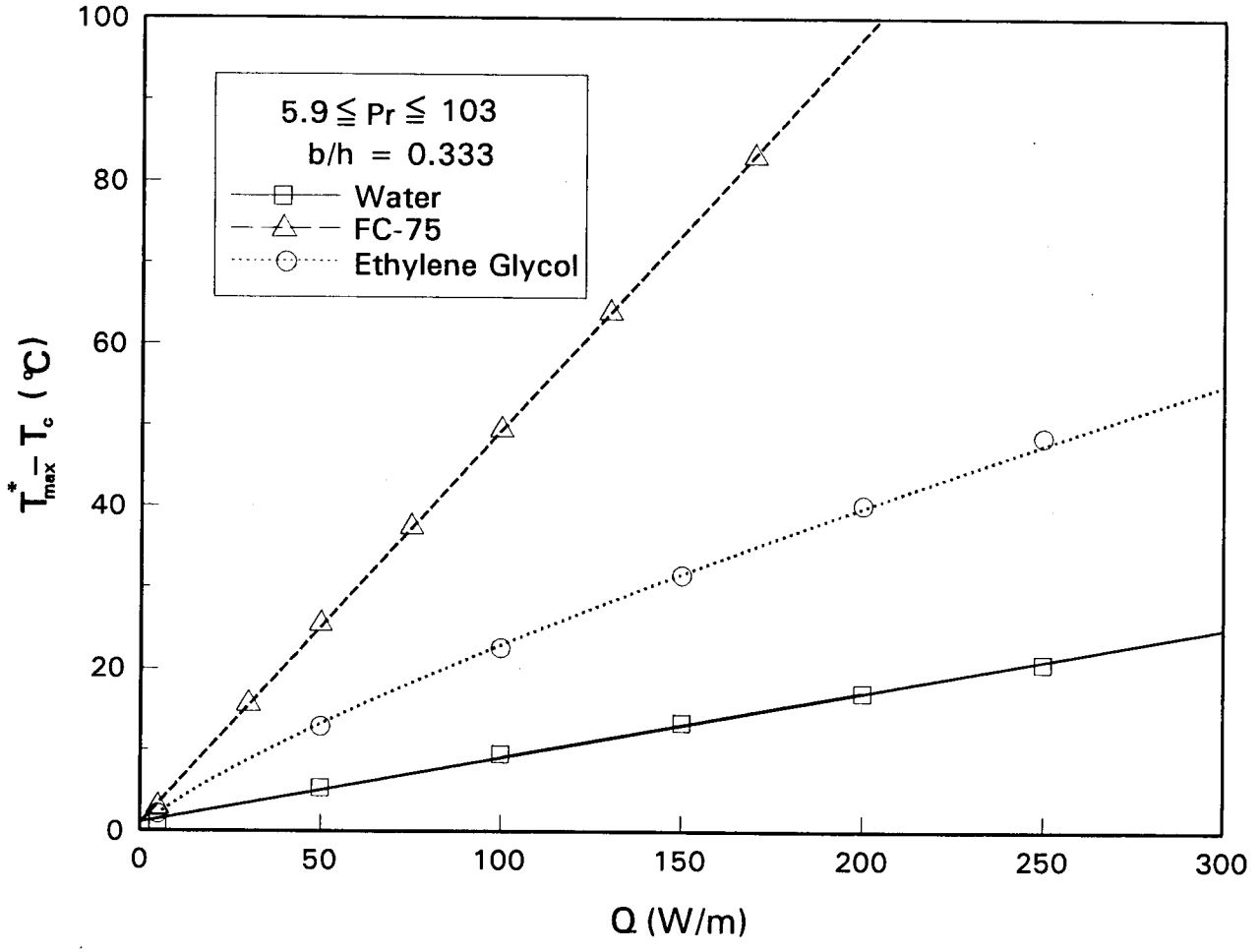

Figure 6.33 Maximum temperature for third protruding heated surface for cooling liquids in relation to heat inputs.

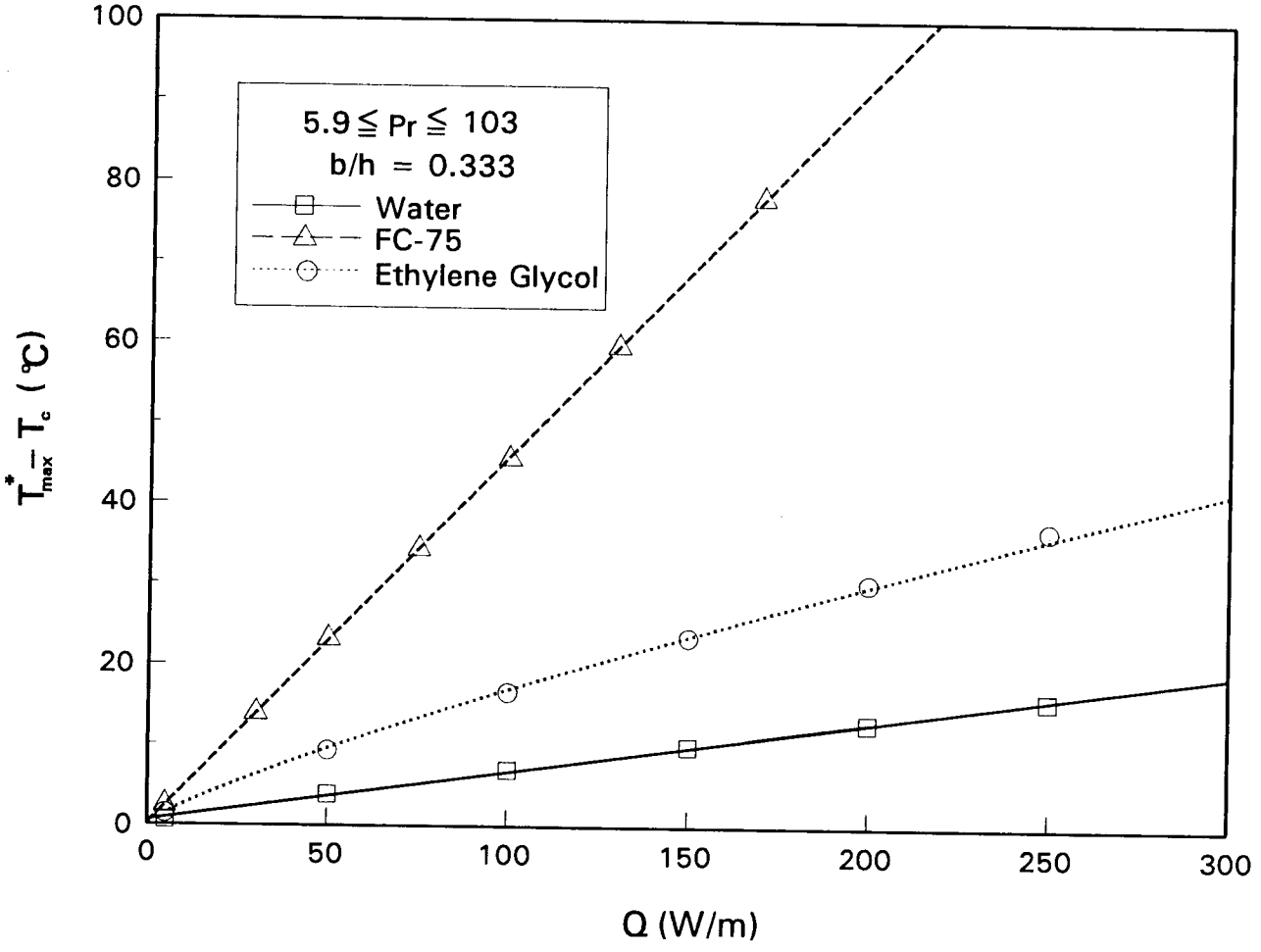

Figure 6.34 Maximum temperature for first protruding heated surface for cooling liquids in relation to heat inputs.

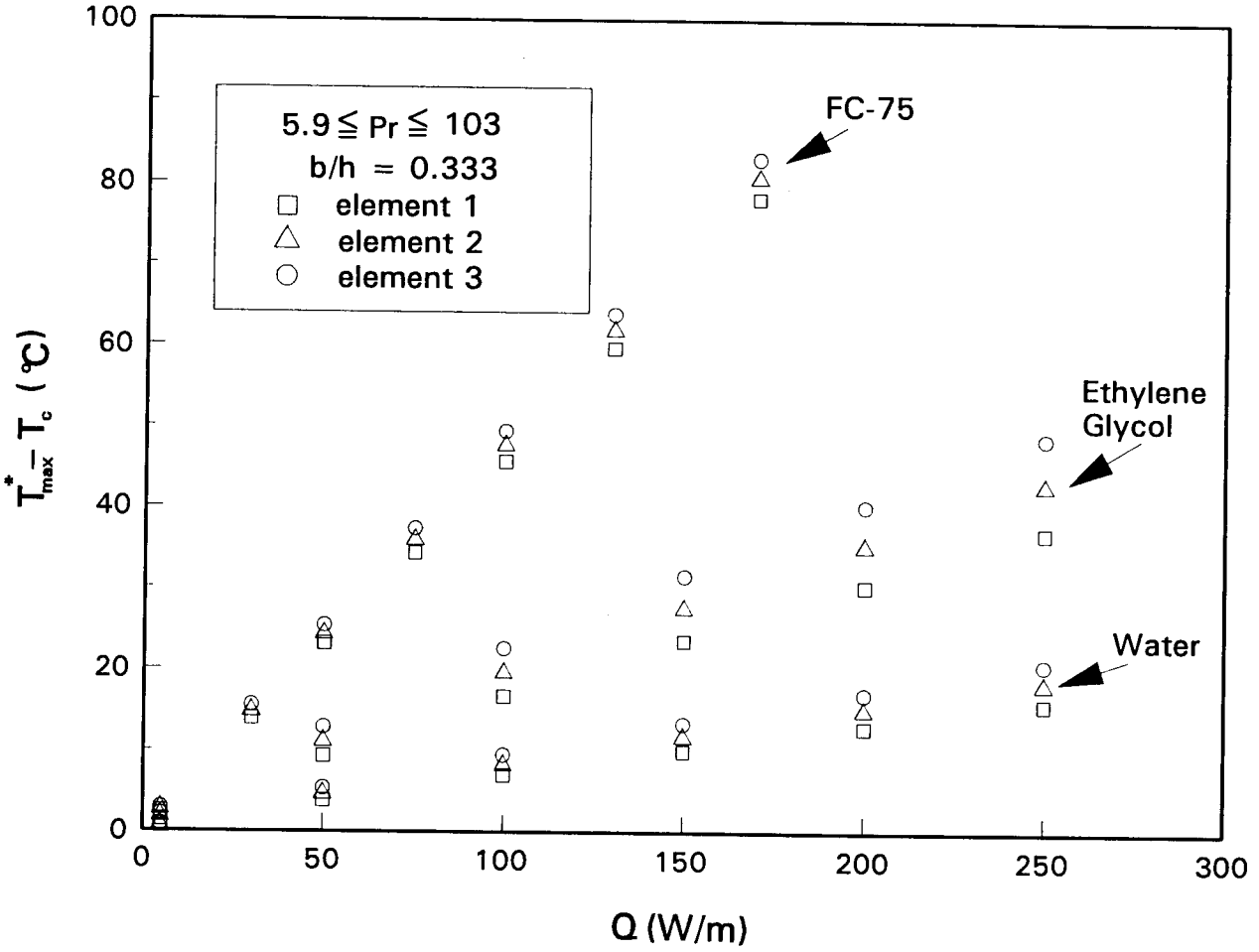

Figure 6.35 Maximum temperature for each protruding heated surface for cooling liquids in relation to heat inputs.

ethylene glycol, ΔT increased at a nonlinear trend with small heat inputs, then increased proportionately with an increase in ΔT . Therefore, for protruding surfaces in devices subject to identical heat inputs,

$$\Delta T_{\text{FC-75}} > \Delta T_{\text{e.g.}} > \Delta T_{\text{water}} .$$

The plots for Q in relation to ΔT for the various cooling liquids clearly indicated that the temperature distributions were closely related to the heat transfer properties of the coolants.

Figure 6.35 indicates that the highest temperatures for the surface of the upper protruding device surface were greater than the highest temperatures for the lower protruding device surface. This trend contributed to increased buoyancy flow subject to convection adjacent to the upper device as well as thermal spread as the flow advanced downstream. That is, the higher temperatures of the upper device resulted from rising warm fluids. Though FC-75 reflected a trend of large temperature increments for given identical heat inputs, the temperature spread between the upper and lower device surface temperatures was larger for ethylene glycol than for FC-75.

6.4 Optimization of Channel Spacing to Height Ratios in Relation to Maximum Temperatures of Protruding Heated Surfaces

The channel intervals which result in the most effective reductions of protruding heated surface temperatures within heated channel systems are discussed in this section. The determination of optimum ratios, $\left(\frac{b}{h}\right)_{opt}$, for the various cooling liquids was based upon consideration of maximum protruding surface temperatures as a standard, as indicated in Figures 6.36 to 6.38. Maximum temperatures at the protruding surfaces for each channel were generally found in the area of the third protruding surface.

Information derived from Figures 6.36 to 6.38 may be used to determine which channel spacings provide minimum value among the maximum surface temperatures for each channel spacing at given identical heat inputs. The dimensionless value, Θ, was defined as $\Delta T_i/\Delta T_{min}$, where ΔT_i was the temperature difference between the protruding heated maximum surface temperature and the constant cold enclosure temperature for each channel spacing and ΔT_{min} was the minimum value within the ΔT_i range. Several heat inputs, Q, for different cooling fluids were considered to indicate temperature change trends according to changes in channel spacing. Though these various heat inputs, Q, were considered for protruding devices in each coolant, it was

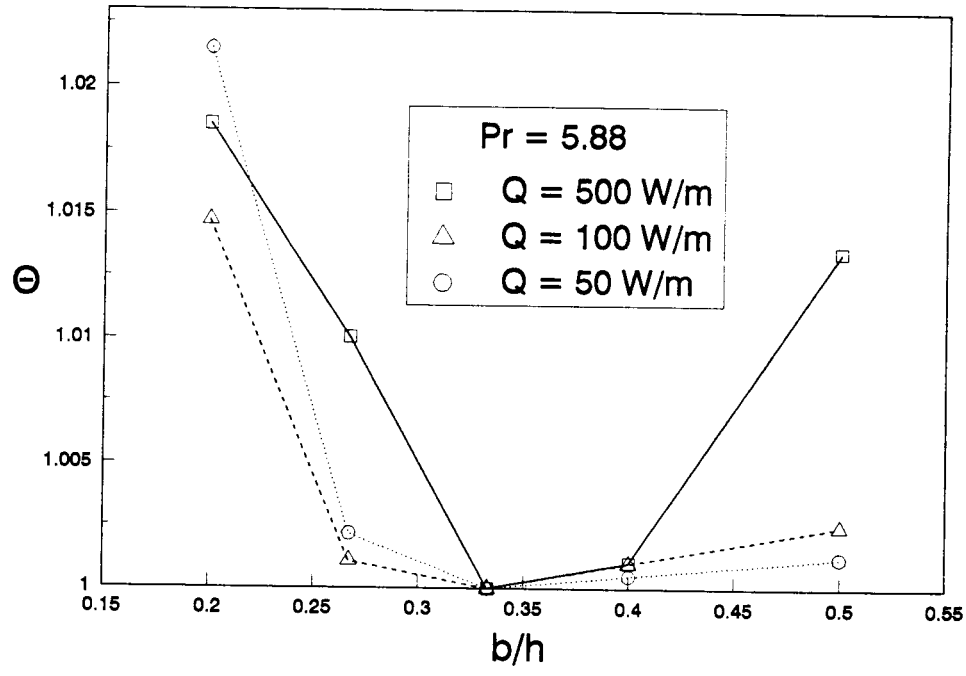

Figure 6.36 Temperature change ratios in relation to channel spacing ratios at various heat inputs for Pr = 5.9.

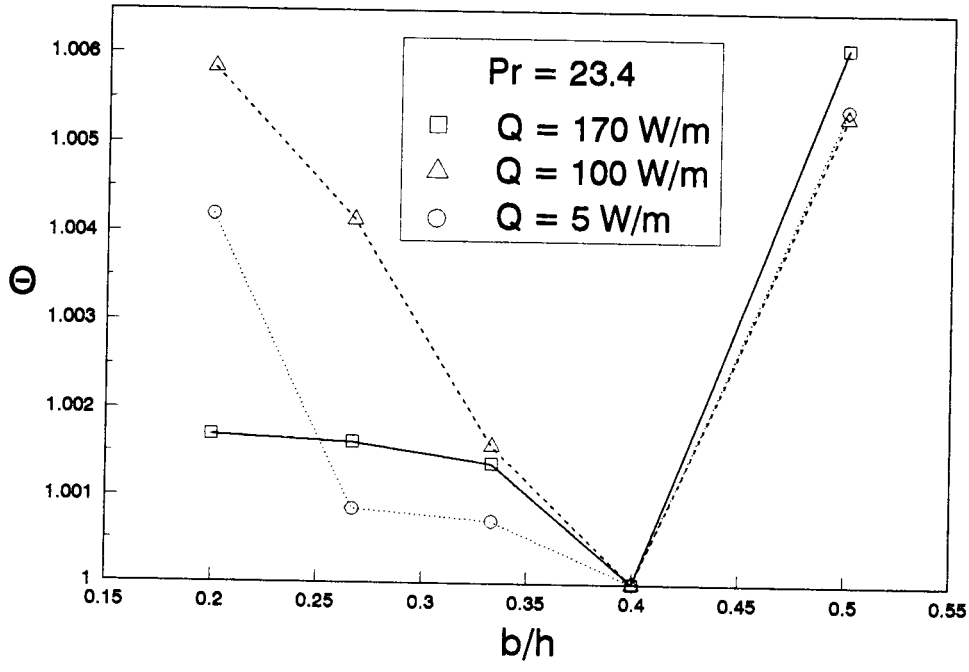

Figure 6.37 Temperature change ratios in relation to channel spacing ratios at various heat inputs for Pr = 23.4.

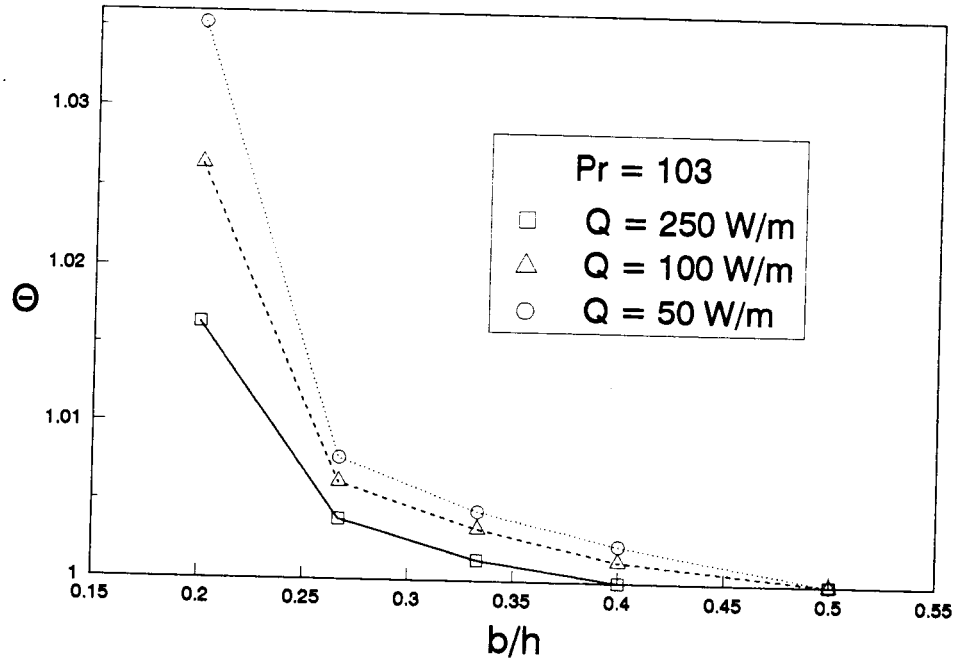

Figure 6.38 Temperature change ratios in relation to channel spacing ratios at various heat inputs for Pr = 103.

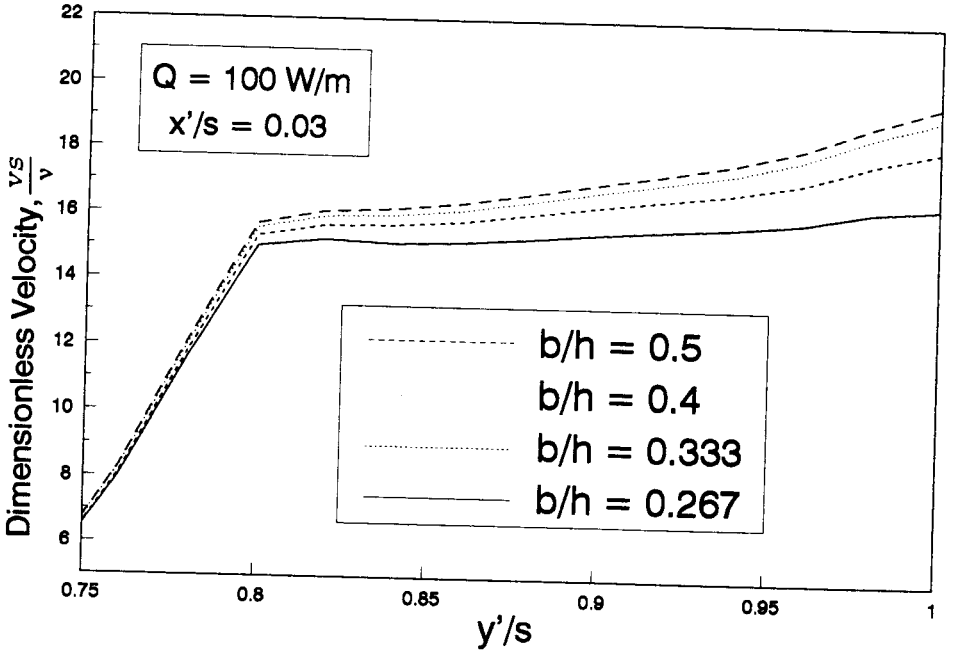

Figure 6.39 Dimensionless velocities for ethylene glycol adjacent to the third protruding surface for channel spacing ratio, Pr = 103.

determined that certain channel spacings resulted in the optimization of maximum surface temperature reductions.

For water, the optimum channel spacing to height ratio for five channel spacing options was 0.333. The largest variation of θ in relation to channel spacing was approximately 1.02. In turn, for FC-75 and for ethylene glycol, the optimum ratios were, respectively, 0.4 and larger than 0.4 with values of θ , respectively, less than 1.01 or larger than 1.03. The values of θ for ethylene glycol was larger than equivalent values for the other coolants. This finding indicated that ethylene glycol, among the liquids considered, was the cooling liquid most sensitive to temperature changes in relation to changes in channel spacing.

It is of interest to determine why and in which situations variations in channel spacing affect the surface temperatures of heated protruding surface devices subject to identical heat inputs. The fluid velocities of ethylene glycol, near the protruding surfaces for various channel spacings, were observed to measure this channel spacing effect. Figure 6.39 indicates that velocities increased at greater rates around the third protruding surface, or the area of maximum temperature as channel spacing was increased. Thus, from comparison of the results given in Figures 6.38 and 6.39, it was found that the velocities at heated surfaces in relation to channel spacing were significantly related to reductions in temperature.

6.5 Heat Transfer Correlations for Vertical Channels

The plot between the Nusselt number at each protruding element surface and the modified channel Rayleigh number, $\left(\frac{b}{h}\right)Ra_b^*$, based upon heat flux and characteristic length, b, is shown in Figure 6.40 for water. This approach was based upon the method developed by Elenbaas [9] for vertical channels. In Figure 6.40, the solid line describes the correlation equation between the average Nusselt number for all three protruding surfaces and the modified channel Rayleigh number for various average heat fluxes at the protruding surfaces and for different channel distances. In turn, Figure 6.41 shows the plot between the Nusselt number and the channel Rayleigh number, $\left(\frac{b}{h}\right)Ra_b$, based on heat input, Q. The dashed line in Figure 6.41 describes the correlation equation between the average Nusselt number for all protruding surfaces and the channel Rayleigh number for various heat inputs at the protruding surfaces and for various channel distances. From the results indicated in Figures 6.40 and 6.41, it was found that the Nusselt number, or the heat transfer coefficient for the first protruding element surface among all three protruding surfaces, was higher than for the third protruding element surface. Since they are directly related to knowledge of channel cooling configurations, and if the channel spacing as well as the heat flux/inputs from a heated device mounted upon a vertical plate are known, the

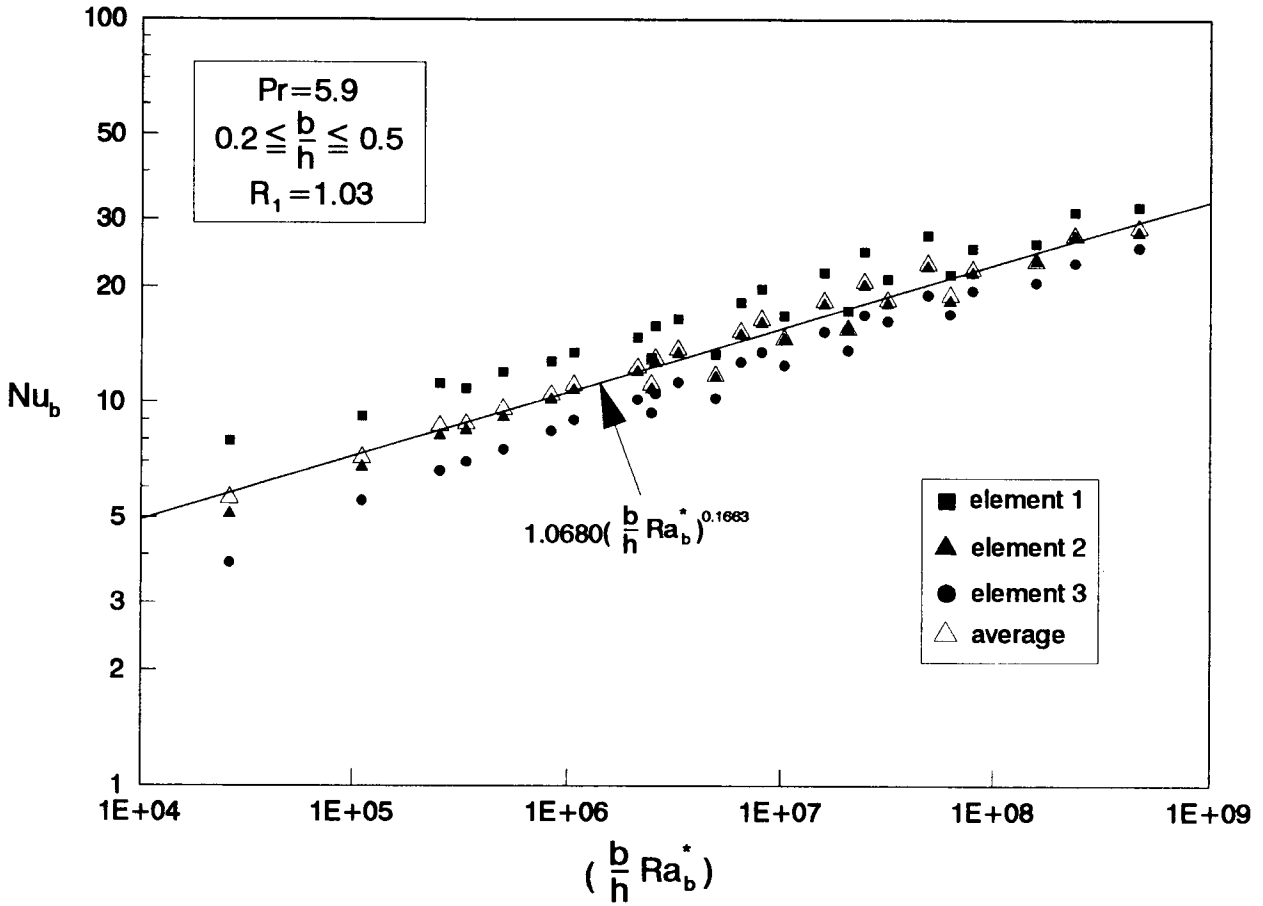

Figure 6.40 Correlation of the Nusselt number and the modified channel Rayleigh number for water.

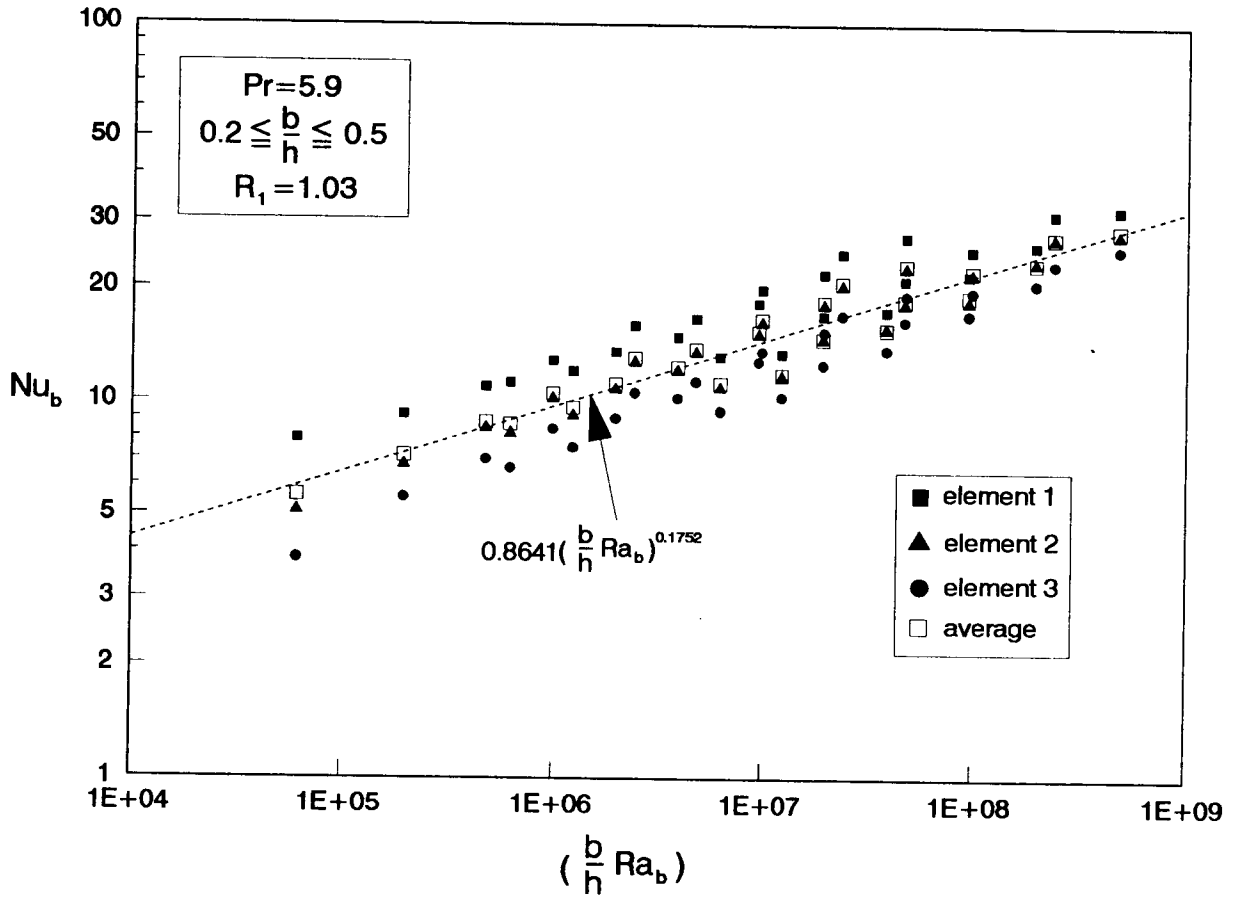

Figure 6.41 Correlation of the Nusselt number and the channel Rayleigh number for water.

correlation equations constitute a noteworthy research contribution.

Correlations of the average Nusselt number computed for all protruding element surfaces, considered as functions of the channel modified Rayleigh number, $\left(\frac{b}{h}\right)Ra_b^*$, or channel Rayleigh number, $\left(\frac{b}{h}\right)Ra_b$, are shown in Figures 6.42 to 6.44 for, respectively, water, ethylene glycol, and FC-75. The modified channel Rayleigh number is a function of heat flux and channel width. Thus, changes in channel width or in heat flux produce changes in the Rayleigh number, which in turn results in the variation of the Nusselt number.

For the vertical channel data, the results were compared to equations provided by Fujii and Fujii [6]. The Fujii correlation for vertical surfaces at uniform heat flux was modified for the case of vertical channels. The Fujii correlation equation was evaluated at midheight $(h/2)$ of a vertical surface for average values, and then was multiplied by $2\left(\frac{b}{h}\right)$ to obtain an equation suitable for the case of vertical channels. From the application of the Prandtl number for each coolant, the Fujii equation for vertical channels becomes:

$$Nu_b = 0.673\left(\left(\frac{b}{h}\right)Ra_b^*\right)^{0.2}, \qquad Pr = 5.9 \qquad (6\text{-}1)$$

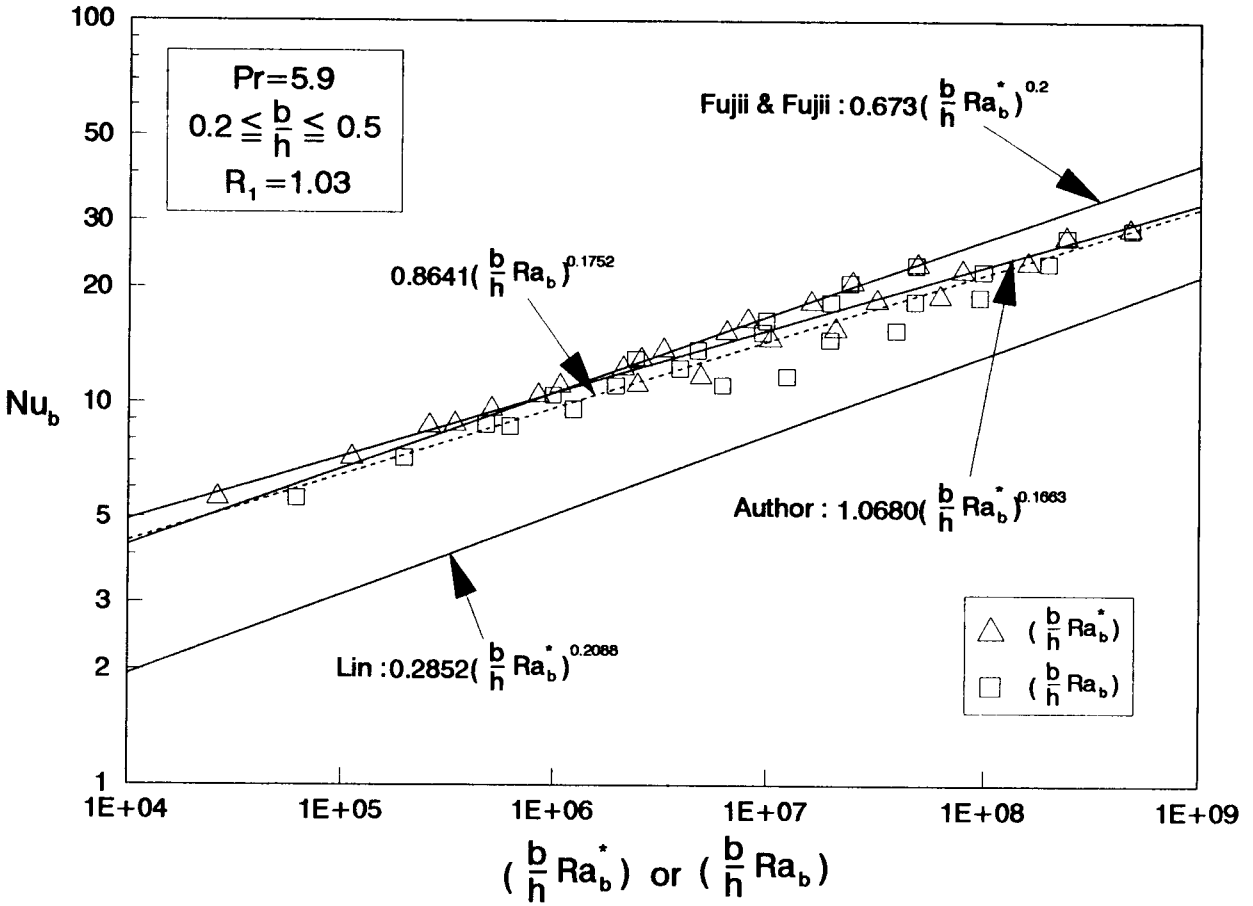

Figure 6.42 Comparison of water data to the Fujii [6] correlation and the Lin [39] experimental output for average Nusselt numbers.

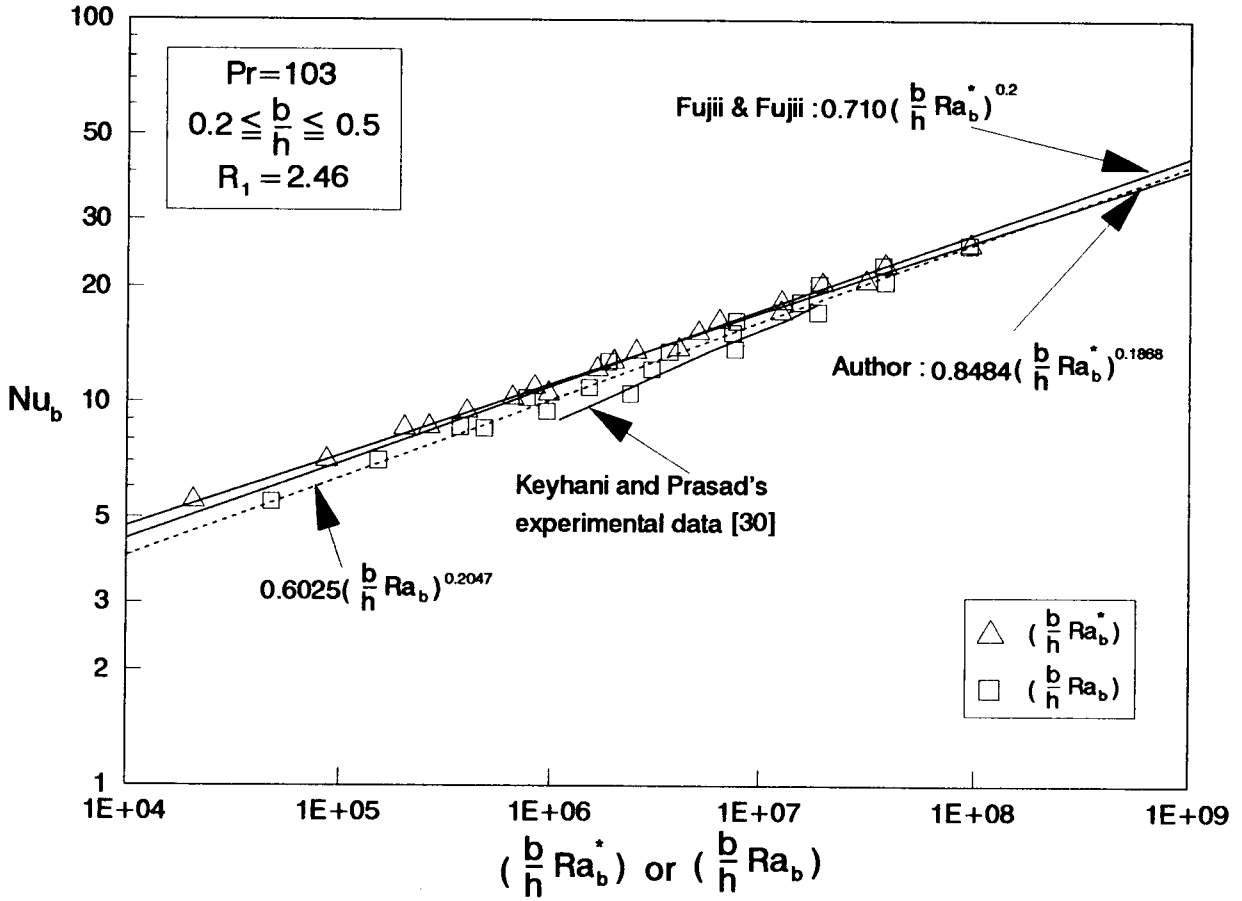

Figure 6.43 Comparison of ethylene glycol data to the Fujii [6] correlation and the Keyhani [30] experimental output for average Nusselt numbers.

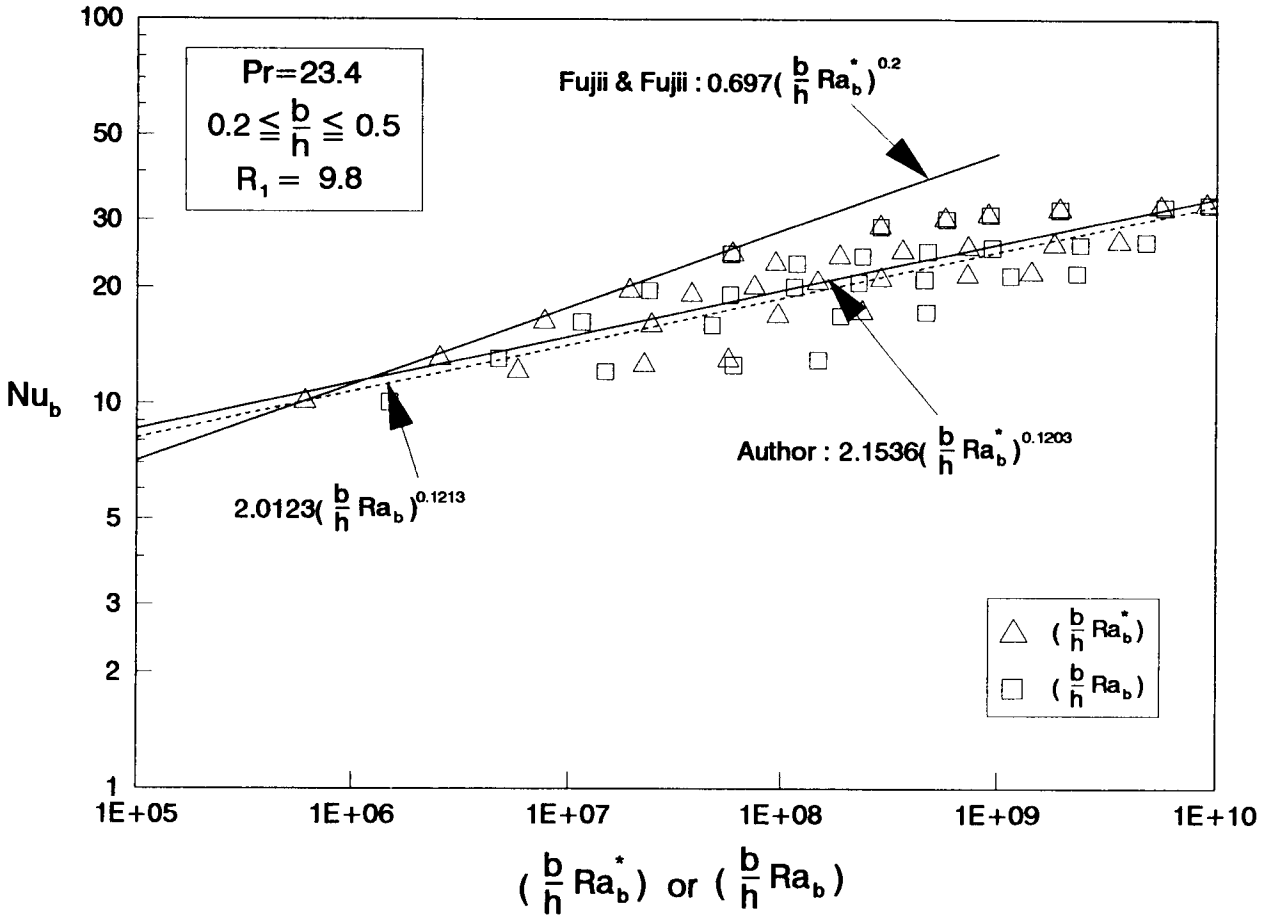

Figure 6.44 Comparison of FC-75 data to the Fujii [6] correlation for average Nusselt numbers.

$$Nu_b = 0.697\left(\left(\frac{b}{h}\right)Ra_b^*\right)^{0.2}, \qquad Pr = 23.4 \qquad (6\text{-}2)$$

$$Nu_b = 0.710\left(\left(\frac{b}{h}\right)Ra_b^*\right)^{0.2}. \qquad Pr = 103 \qquad (6\text{-}3)$$

Since appropriate or available correlation ranges for modified Rayleigh numbers were not considered in the Fujii and Fujii [6] equation, the modified channel Rayleigh number ranges were applied as wide ranges, $10^4 \le \left(\frac{b}{h}\right)Ra_b^* \le 10^9$, in Figures 6.42 to 6.44. For water (Fig. 6.42), the results were also compared to the Lin [39] equation derived from experimental results. However, Lin's equation was acquired using somewhat different geometries and boundary conditions, different conductivities for heated materials, and different means of providing heat input to the heated blocks. As may be seem from Figure 6.42, the values of the Nusselt number for the research model considered in the present study were located between the results from the Fujii and Fujii [6] equation and the results obtained by Lin [39] from experimentation.

For ethylene glycol, Figure 6.43 shows a comparison of the experimental results obtained by Keyhani [30] for a vertical cavity (aspect ratio, $\left(\frac{b}{h}\right) = 0.222$) based upon one isothermal cold wall in relation to an opposing vertical wall with three discrete, flush-heated sections of equal height. The results for ethylene glycol obtained from the present investigation were closer to the Fujii and Fujii

[6] correlation data and the Keyhani [30] experimental data than for the other liquids considered. For both water and FC-75, the Fujii equation overpredicted the value of the Nusselt number, particularly in higher ranges of $\left(\frac{b}{h}\right)\mathrm{Ra}_b^*$, as shown in Figures 6.42 and 6.44. This result was anticipated since the present investigation was concerned with protruding discrete heating device elements rather than continuously heated surfaces on a single channel plate.

A comparison between the Lin [39] correlation equation, for $0.72 \leq \mathrm{Pr} \leq 1009$ where $0.1 \leq \left(\frac{b}{h}\right) \leq 0.5$, and the correlation equation obtained from numerical results in the present study, $5.9 \leq \mathrm{Pr} \leq 103$ where $0.2 \leq \left(\frac{b}{h}\right) \leq 0.5$, is shown in Figure 6.45. It is of interest to note that though the two approaches reflect somewhat different conditions, the results of this comparison are well-matched with respect to the correlation of the Nusselt number and the modified channel Rayleigh number.

To set the correlation equation for the present study, the independent dimensionless parameters were the modified channel Rayleigh number and the channel Rayleigh number. The dependent dimensionless parameter, the average Nusselt number for all three protruding surfaces, was calculated in accordance with the following relations to fit the heat transfer data by the least-squares method of curve fitting. These correlations, based upon the independent parameter for the three liquid coolants considered and varying channel spacings, are:

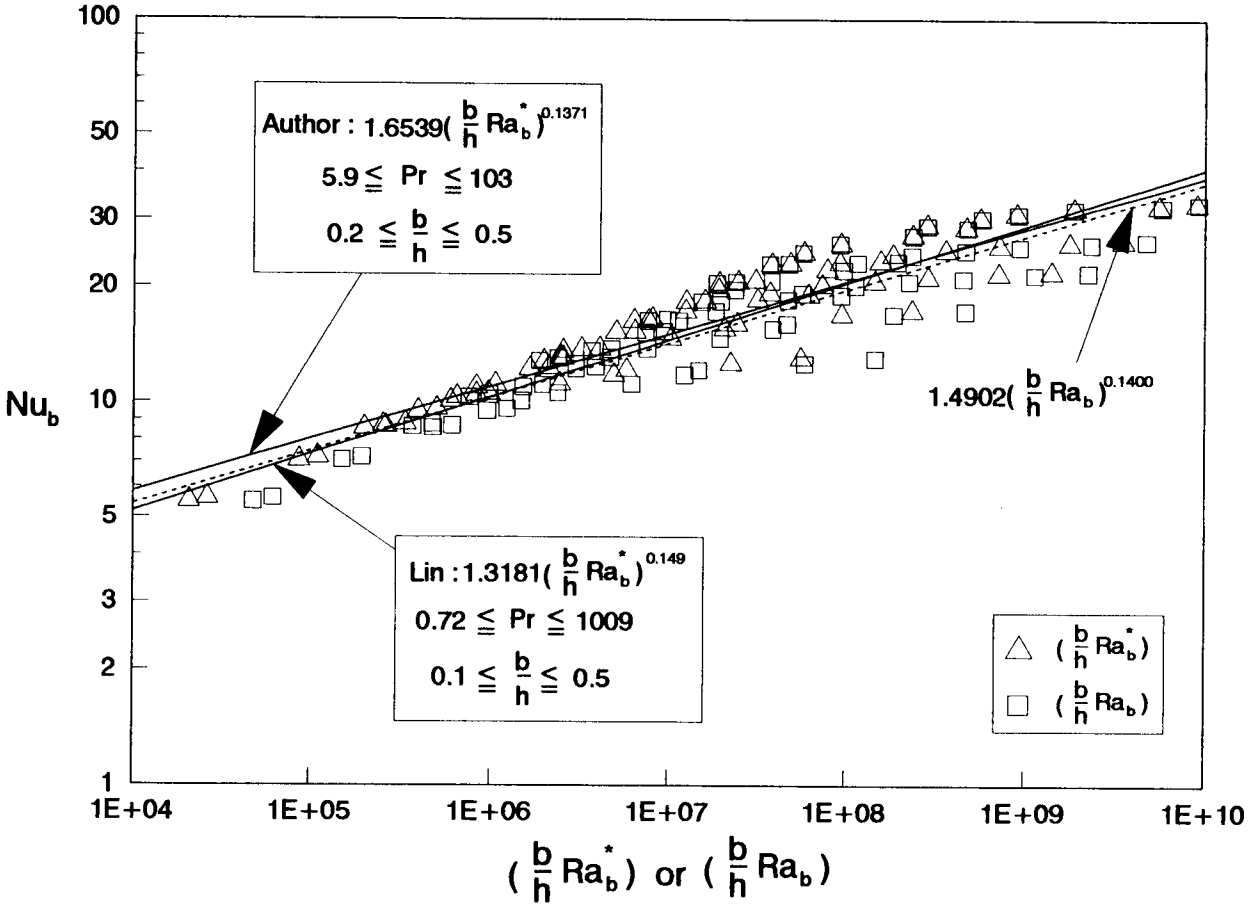

Figure 6.45 Comparison of data for all liquids with the Lin [39] experimental correlation for average Nusselt number.

$$Nu_b = 1.0680\left(\frac{b}{h}\,Ra_b^*\right)^{0.1663} \qquad (6\text{-}4)$$

and

$$Nu_b = 0.8641\left(\frac{b}{h}\,Ra_b\right)^{0.1752} \qquad (6\text{-}5)$$

for Pr = 5.9, $0.2 \le \frac{b}{h} \le 0.5$, and $R_1 = 1.03$;

$$Nu_b = 0.8484\left(\frac{b}{h}\,Ra_b^*\right)^{0.1868} \qquad (6\text{-}6)$$

and

$$Nu_b = 0.6025\left(\frac{b}{h}\,Ra_b\right)^{0.2047} \qquad (6\text{-}7)$$

for Pr = 103, $0.2 \le \frac{b}{h} \le 0.5$, and $R_1 = 2.46$; and

$$Nu_b = 2.1536\left(\frac{b}{h}\,Ra_b^*\right)^{0.1203} \qquad (6\text{-}8)$$

and

$$Nu_b = 2.0123\left(\frac{b}{h}\,Ra_b\right)^{0.1213} \qquad (6\text{-}9)$$

for Pr = 23.4, $0.2 \le \frac{b}{h} \le 0.5$, and $R_1 = 9.8$.

For all coolants combined, the correlation equation, based upon an independent parameter, either $\left(\frac{b}{h}\right)Ra_b^*$ or $\left(\frac{b}{h}\right)Ra_b$, for the protruded vertical channel was

$$Nu_b = 1.6539\left(\frac{b}{h}\,Ra_b^*\right)^{0.1371} \qquad (6\text{-}10)$$

and

$$Nu_b = 1.4902\left(\frac{b}{h}\,Ra_b\right)^{0.1400} \qquad (6\text{-}11)$$

for $5.9 \le Pr \le 103$, $0.2 \le \frac{b}{h} \le 0.5$, and $1.03 \le R_1 \le 9.8$.

Average errors, maximum errors, standard deviations, and R^2 for the various correlation equations are given in Table 6.1.

Table 6.1 Channel correlations for protruded heated elements.

Correlation equation	Average error	Maximum error	Standard deviation	R^2
6-4	9.61	27.43	8.45	96.61
6-5	9.61	27.42	8.46	92.71
6-6	8.67	24.83	7.61	99.53
6-7	8.66	24.81	7.60	97.47
6-8	13.87	31.84	11.22	74.73
6-9	13.89	31.82	11.23	64.38
6-10	11.00	31.86	9.75	89.19
6-11	11.02	31.85	9.76	84.16

CHAPTER 7

CONCLUSIONS AND RECOMMENDATIONS

7.1 Conclusion

This study has developed and considered a numerical investigation of natural convection heat transfer from three uniformly heated protruding elements mounted on a vertical plate placed in opposition to a second plate. Three available cooling liquids, including distilled water, FC-75, and ethylene glycol, were employed to compare heat transfer cooling effects from the protruding heat sources. Dimensionless parameters were computed for the following ranges:

1) $5.9 \leq Pr \leq 103$,

2) $10^4 < \left(\frac{b}{h}\right)(Ra_b^*) < 10^{10}$,

3) $10^4 < \left(\frac{b}{h}\right)(Ra_b) < 10^{10}$,

4) $1.03 \leq R_1 \leq 9.8$,

5) $0.43 \leq R_2 \leq 4.05$, and

6) $0.2 \leq \frac{b}{h} \leq 0.5$.

From this research investigation, the following conclusions are provided:

1) For a given identical heat source (Q) subject to heated elements for different cooling fluids in a

steady-state, the temperature difference (ΔT) between the maximum protruding element heated surface temperature and the cold enclosure temperature decreased as fluid thermal conductivity (k_f) or thermal diffusivity (α_f) increased, and as fluid thermal expansion (β_f) decreased. The relationship exhibited was $\Delta T_{FC-75} > \Delta T_{e.g.} > \Delta T_{water}$. That is, since

$$k_{water} > k_{e.g.} > k_{FC-75}$$

$$\alpha_{water} > \alpha_{e.g.} > \alpha_{FC-75}$$

$$\beta_{water} < \beta_{e.g.} < \beta_{FC-75} ,$$

the protruding surface temperature was the lowest in water, second lowest in ethylene glycol, and highest in FC-75 for given discrete uniform heating among the protruding elements. Since ΔT increased as R_1 increased, the temperature difference (ΔT) was also in close relationship to the conductivity ratio (R_1) between the heat generating solid and the cooling liquid.

2) The temperature difference (ΔT) increased linearly as the heat source (Q) was increased for each protruding element in water, FC-75, and ethylene glycol. The single exception was that with small heat inputs, ΔT increased nonlinearly for ethylene glycol, increasing proportionately as heat inputs were increased.

3) The first protruding element exhibited the lowest surface temperatures and the most favorable cooling effect since its location was near the plate leading edge. The maximum temperature at the third protruding element surface was generally higher than the maximum temperature at either the first or second protruding element surface. These trends contributed to the rise of warm fluids as they were convected about the upper element as well as thermal spread as the flows advanced downstream.

4) Flow patterns with different channel spacing to height ratios typically presented three distinct flow regions within the protruding heated channel. Reversed flows from the circulation effect near the top surface of the enclosure occurred in the channel top portion when channel spacings were relatively large. The penetration depth of the reversed flows were closely related to both channel spacing and liquid cooling properties; relatively high velocity flows gathered at the front of the heated element rose along the plate with protruding elements, whereas, for large channel spacings, weak flow regions were located adjacent to the unheated shrouding plate in the middle portion of the channel.

5) The temperature fields for different channel spacing to height ratios for different cooling liquids were identified by isothermal lines. From the computational results of the present study, the configuration of the temperature fields changed in accordance with the location of the unheated shrouding plate.

6) To determine which channel intervals provided the most effective reductions in protruding heated surface temperatures, optimum channel spacing to height ratios were investigated. Determination of optimum ratios, $\left(\frac{b}{h}\right)_{opt}$, was derived from observations of temperature change trends in relation to changes in channel spacing. Several heat inputs, Q, were applied to the protruding devices for each coolant, resulting in the determination that certain channel spacings served to maximize surface temperature reductions. For water, FC-75, and for ethylene glycol, the optimum channel spacing to height ratios among five channel spacing ratio options were, respectively, 0.333, 0.4, and greater than 0.4.

7) The most favorable correlations for protruding vertical channels for combinations of all the cooling liquids were

$$Nu_b = 1.6539\left(\left(\frac{b}{h}\right)Ra_b^*\right)^{0.1371}$$

and

$$Nu_b = 1.4902\left(\left(\frac{b}{h}\right)Ra_b\right)^{0.1400},$$

with standard deviations of 9.75% and 9.76%, respectively, for $5.9 \leq Pr \leq 103$, $0.2 \leq b/h \leq 0.5$, and $1.03 \leq R_1 \leq 9.8$.

7.2 Recommendations

Recommendations for further investigation to extend the findings of the present study are as follows:

1) Conduct numerical simulations of enclosures with two to three repeated vertical channels subject to PCB-mounted protruding heated devices, based upon patterns used within modern electronic systems. The present structure of PCB arrangements is such that heat dissipation from heated sources takes place partially by convection into cooling fluids and partially by conduction to the PCB itself. The heat conducted to the PCB is eventually removed by convection to the adjacent vertical channel and is thus repeated in every vertical channel.

2) Other than for 0.8, analyze heat transfer effects by varying the ratio of protruding heated element height to width, $\frac{l_c}{B}$.

3) Determine the channel heat transfer effect from increasing the number of protruding heated elements and decreasing the height of the heated element.

4) Analyze the effect of non-uniform heat source inputs for heated elements.

5) Other than for $1.0 \leq R_1 \leq 10.0$, analyze varied conductivity ratios (R_1) between solid and liquid coolants.

6) Simulate various enclosure height to channel plate ratios (H/h) to determine the effect of velocity changes about the channel exits, and simulate various enclosure aspect ratios (H/L) to evaluate the influence of enclosure geometry upon flows.

7) To seek the most accurately optimal channel spacing to height ratios, analyze channel spacing widths for more than five optional widths.

REFERENCES

1 Chu, R.C., "Heat Transfer in Electronic Systems," in Proceedings of the Eighth International Heat Transfer Conference, Vol.1, Hemisphere, 1986.

2 Aung, W., Cooling Techniques for Computers, Hemisphere Publishing Corporation, New York, 1990.

3 Patankar, S.V., Numerical Heat Transfer and Fluid Flow, Hemisphere Publishing Corporation, Washington D. C., 1980.

4 Amsden, A.A. and F.H. Harlow, The SMAC Method: A Numerical Technique for Calculating Incompressible Fluid Flows, Los Alamos Scientic laboratory, TID-4500, 1970.

5 Sparrow, E.M. and J.L. Gregg, "Laminar Free Convection from a Vertical Plate with Uniform Surface Heat Flux," Transactions of the ASME, Vol. 78, pp. 435-440, 1956.

6 Fujii, T. and M. Fujii, "The Dependence of Local Nusselt Number on Prandtl Number in the Case of Free Convection Along a Vertical Surface with Uniform Heat Flux," International Journal of Heat and Mass Transfer, Vol.19, pp. 121-122, 1976.

7 Roy, S., "The Dependence of Local Nusselt Number on Prandtl Number in Free Convection," Letters in Heat and Mass Transfer, Vol. 3, pp. 227-230, 1976.

8 Churchill, S.W. and H.H.S. Chu, "Correlating Equations for Laminar and Turbulent Free Convection from a Vertical Plate," International Journal of Heat and Mass Transfer, Vol.18, pp. 1323-1329, 1975.

9 Elenbaas, W., "Heat Dissipation of Parallel Plates by Free Convection," Physica, Vol. 9, pp. 1-28, 1942.

10 Tao, L.N., "On Conbined Free and Forced Convection in Channels," Transactions of the ASME, Journal of Heat Transfer, Vol. 82, pp. 233-238, 1960.

11 Bodoia, J.R. and J.F. Osterle, "The Development of Free Convection between Heated Vertical Plates, "Transactions of the ASME, Journal of Heat Transfer, Vol. 84, pp. 40-44,1962.

12 Aung, W., "Fully Developed Laminar Free Convection between Vertical Plates Heated Asymmetrically," International Journal of Heat and Mass Transfer, Vol. 15, pp. 1577-1580, 1972.

13 Miyatake, O., T. Fujii, and H. Tanka, "Natural Convective Heat Transfer between Vertical Parallel Plates—One Plate with a Uniform Heat Flux and the Other Thermally Insulated," Heat Transfer-Japanese Reaserch, Vol. 2, No. 1, pp. 25-32, January 1973.

14 Miyatake, O. and T. Fujii, "Free Convective Heat Transfer Between Vertical Parallel Plates—One Plate Isothermally Heated and the Other Thermally Insulated," Heat Transfer-Japanese Research, Vol. 1, No. 3, pp 30-38, July 1972.

15 Miyatake, O. and T. Fujii, "Natural Convective Heat Transfer between Vertical Parallel Plates at Unequal Uniform Temperatures," Heat Transfer-Japanese Research, Vol. 2, No. 4, pp. 79-88, October 1973.

16 Miyatake, O. and T. Fujii, "Natural Convective Heat Transfer between Vertical Parallel Plates with Unequal Heat Fluxes," Heat Transfer-Japanese Research, Vol. 3, No. 3, pp. 29-33, July 1974.

17 Siegel, R. and R.H. Norris, "Tests of Free Convection in a Partially Enclosed Space between Two Heated Vertical Plates," Transactions of the ASME, Vol. 79, pp. 663-673, April 1957.

18 Sparrow, E.M., G.M. Chrysler, and L.F. Azevedo, "Observed Flow Reversals and Measured-Predicted Nusselt Numbers for Natural Convection in a One-Sided Heated Vertical Channel, "Transactions of the ASME, Journal of Heat Transfer, Vol. 106, pp. 325-332, May 1984.

19 Levy, E.K., "Optimum Plate Spacings for Laminar Natural Convection Heat Transfer from Parallel Vertical Isothermal Flat Plates," Transactions of the ASME, Journal of Heat Transfer, Vol. 93, pp. 463-465, November 1971.

20 Burch, T., T. Rhodes and S. Acharya, "Laminar Natural Convection between Finitely Conducting Vertical Plates," International Journal of Heat and Mass Transfer, Vol. 28, No. 6, pp. 1173-1186, 1985.

21 Kim, S.H., N.K. Anand, and L.S. Fletcher, "Free Convection Between Series of Vertical Parallel Plates with Embedded Line Heat Sources," Transactions of the ASME, Journal of Heat Transfer, Vol. 113, pp. 108-115, 1991.

22 Hanzawa, T., H. Ishihara, K. Sekiguchi, T. Fujii, Y. Suzuki, and K. Kato, "Natural Convection Heat Transfer Between Vertical Parallel Plates with Symmetric and Asymmetric Heating," Heat Transfer-Japenese Research, Vol. 17, No. 5, pp. 61-70, 1988.

23 Chang, T.S. and T.F. Lin, "Transient Buoyancy-Induced Flow through a Heated, Vertical Channel of Finite Height," Numerical Heat Transfer, Part A, Vol. 16, pp. 15-35, 1989.

24 Wirtz, R.A. and R.J. Stutzman, "Experiments on Free Convection Between Vertical Plates with Symmetric Heating," Transactions of the ASME, Journal of Heat Transfer, Vol. 104, pp. 501-507, August 1982.

25 Ramanathan, S. and R. Kumar, "Correlations for Natural Convection between Heated Vertical Plates," ASME, HTD-Vol. 100, pp. 1-12, 1988.

26 Jaluria, Y., "Interaction of Natural Convection Wakes Arising from Thermal Sources on a Vertical Surface," Transactions of the ASME, Journal of Heat Transfer, Vol. 107, pp. 883-892, 1985.

27 Chu, H.H., S.W. Churchill, and C.V.S. Patterson, "The Effect of Heat Size, Location, Aspect Ratio, and Boundary Conditions on Two-Dimensional, Laminar, Natural Convection in Rectangular Channels," Transactions of the ASME, Journal of Heat Transfer, Vol. 98, No. 2, pp. 194-201, May 1976.

28 Turner, B.L. and R.D. Flack, "The Experimental Measurement of Natural Convective Heat Transfer in Rectangular Enclosures with Concentrated Energy Sources," Transactions of the ASME, Journal of Heat Transfer, Vol. 102, pp. 236-241, May 1980.

29 Yan, W.M. and T.F. Lin, "Natural Convection Heat Transfer in Vertical Open Channel Flows with Discrete Heating," International Communications in Heat and Mass Transfer, Vol. 14, pp. 187-200, 1987.

30 Keyhani, M., V. Prasad, R. Chen, and T.T. Wong, "Free Convection Heat Transfer from Discrete Heat Sources in a Vertical Cavity," ASME HTD-Vol.100, pp. 13-24, 1988.

31 Hwang, U.P., "Effect of Folw Direction on Mixed Convection Heat Transfer from a Vertical Flat Plate and a Plate with Square Protuberances," Letters in Heat and Mass Transfer, Vol. 6, pp. 459-468, 1979.

32 Braaten, M.E. and S.V. Patankar, "Analysis of Laminar Mixed Convection in Shrouded Arrays of Heated Rectangular Blocks," ASME HTD-Vol.32, pp. 77-84, 1984.

33 Ortega, A. and R.J. Moffat, "Heat Transfer from an Array of Simulated Electronic Components: Experimental Results for Free Convection With and Without a Shrouding Wall," ASME, HTD-Vol.48, pp. 5-15, 1985.

34 Park, K.A. and A.E. Berglers, "Natural Convection Heat Transfer Characteristics of Simulated Microelectronic Chips," Transactions of the ASME, Journal of Heat Transfer, Vol. 109, pp. 90-96, February 1987.

35 Shakerin, S., M. Bohn, and R.I. Loehrke, "Natural Convection in an Enclosure with Discrete Roughness Elements on a Vertical Heat Wall," International Journal of Heat and Mass Transfer, Vol. 31, No.7, pp. 1423-1430, 1988.

36 Afrid, M. and A. Zebib, "Natural Convection Air Cooling of Heated Components Mounted on a Vertical Wall," Numerical Heat Transfer, Part A, Vol. 15, pp. 243-259, 1989.

37 Hung, Y.H. and W.M. Shiau, "An Effective Model for Measuring Transient Natural Convective Heat Flux in Vertical Parallel Plates with a Rectangular Rib," International Journal of Heat and Mass Transfer, Vol. 32, No. 5, pp. 863-871, 1989.

38 Keyhani, M., L. Chen, and D.R. Pitts, "Aspect Ratio Effect on Natural Convection in an Enclosure with Protruding Heat Sources," ASME, HTD-Vol. 131, pp. 1-11, 1990.

39 Lin, P.C., An Experimental Study of Natural Convection from Protruding Arrays on a Vertical Plate With and Without an Opposing Wall for Various Fluids, Ph.D. thesis, Oregon State University, 1989.

40 Sathe, S.B. and Y. Joshi, "Natural Convection Liquid Cooling of a Substrate-Mounted Protrusion in a Square Enclosure: Effects of Thermophysical Properties, Geometric Dimensions, and Boundary Conditions," ASME, HTD-Vol. 153, pp. 73-80, 1990.

41 Bejan, A., Convection Heat Transfer, John Wiley & Sons, Inc., New York, 1984.

42 Arpaci, V.S. and P.S. Larsen, Convective Heat Tranfer, Prentice-Hall, Inc., New Jersey, 1984.

43 Trent, D.S., and L.L. Eyler, Tempest: A Computer Program for Three-Dimensional Time-Dependent Hydrothermal Analysis, Battelle Pacific Northwest Laboratories, 1991.

44 Joshi, Y. and R.A. Paje, "Natural Convection Cooling of a Ceramic Substrate Mounted Leadless Chip Carrier in Dielectric Liquids," International Communication Heat and Mass Transfer, Vol. 18, pp. 39-47, 1991.

45 Steinberg, D.S., Cooling Techniques for Electronic Equipment, John Wiley & Sons, New York,1991.

46 Scott, A.W., Cooling of Electronic Equipment, John Wiley & Sons, New York, 1974.

47 Incropera, F.P. and D.P. DeWitt, Fundamentals of Heat and Mass Transfer, John Wiley & Sons, New York, 1985.

48 Dow Corning, Materials for High Technology Applications, Dow Corning Corporation, 1989.

APPENDIX

Appendix A

Verification of the Computer Code

The natural convection liquid cooling model for a plate-mounted heat generating block in FC-75, presented by Sathe and Joshi [40], was selected to verify the dimensionless computer code developed for the present study. The reasons for the selection of this specific model were that (1) the model liquid coolant, FC-75, was considered and (2) the numerical configuration of the model simulated a PCB-mounted, uniformly heated device enclosed within a liquid square cavity. Both of these considerations paralleled the research design developed for the present study.

Figure A.1 demonstrates a schematic design for a liquid cooled protruding heat source assembly. At steady-state, the isothermal lines and streamlines from the computational results obtained by Sathe and Joshi [40] were compared to those obtained from the implementation of computer codes developed for the present study. As given in Figures A.2 and A.3 for, respectively, isothermal lines and streamlines, the following conditions were considered: Pr = 25, Ra = 10^6, R_1 = 1.0, and R_2 = 10.

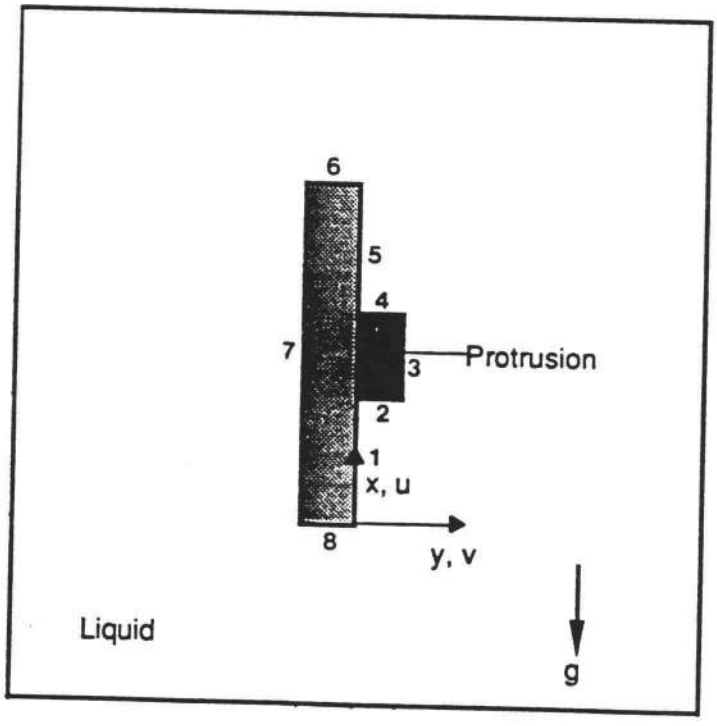

Figure A.1 Schematic diagram of liquid cooling protruding heat source assembly, from Sathe and Joshi [40].

(a)

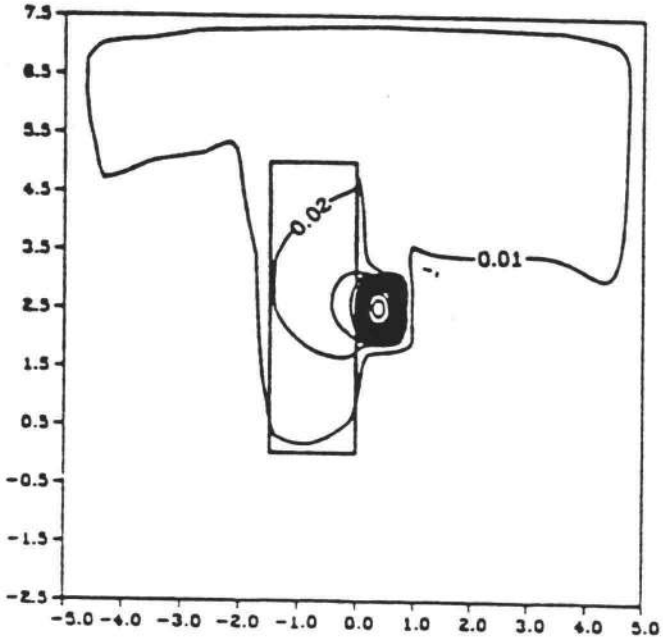

(b)

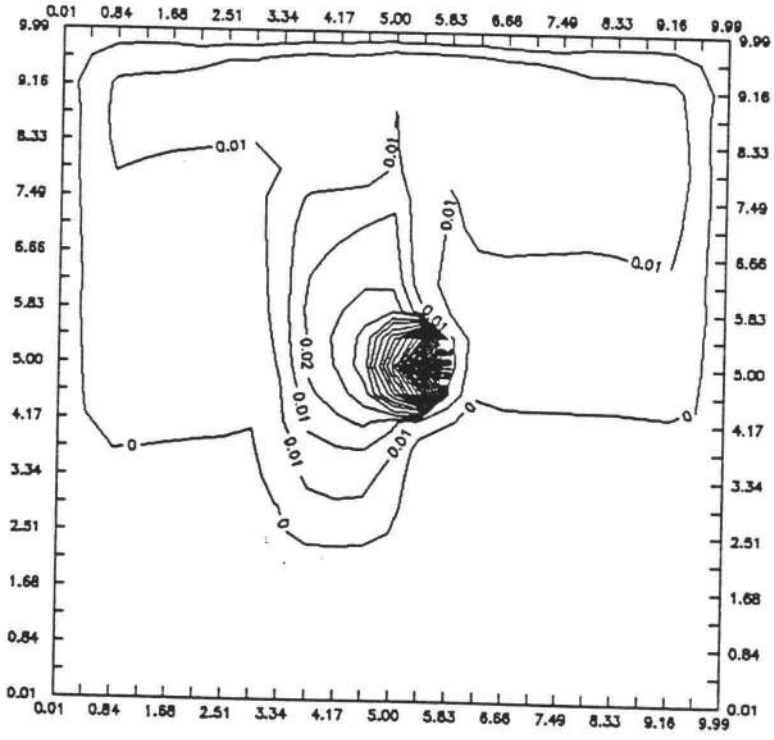

Figure A.2 Comparison of isothermal line patterns, from (a) Sathe and Joshi [40] to (b) isothermal line patterns from present study.

(a)

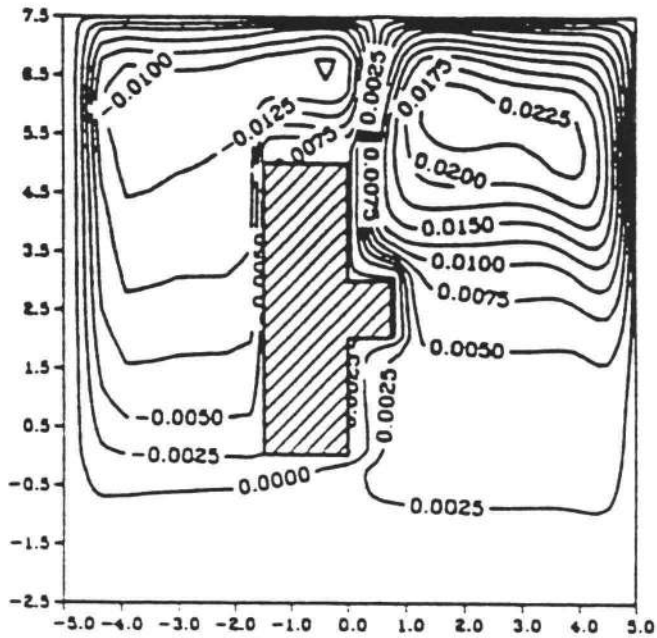

(b)

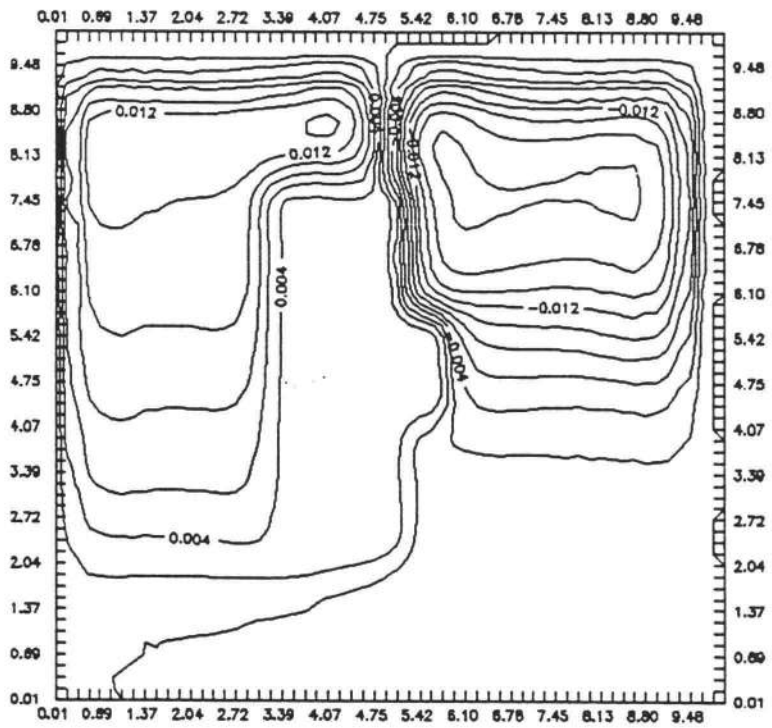

Figure A.3 Comparison of streamline patterns from (a) Sathe and Joshi [40] to (b) streamline patterns from the present study.